Multicomponent Metal-Organic Frameworks

A thesis presented in partial fulfilment of the requirements of the degree of

Doctor of Philosophy
in
Chemistry

at Massey University, Manawatū, New Zealand

Lujia Liu
2015

For Minxuan Du

Abstract

Introducing multiple functional groups into the pores of metal-organic frameworks (MOFs) promise sophisticated properties. Precise control over the position of these functional groups would enable the 3D chemical environment of discrete void spaces to be tailored. This was an outstanding challenge prior to this work. In this thesis we present a study of the synthesis, characterization and properties of MOFs that can meet this goal. These MOFs are multicomponent in nature, being built up from three geometrically distinct organic ligands. Functional groups can be appended to these ligands and are incorporated in precise locations and with perfect order in the frameworks. The chemical environment of the pores of these MOFs is “programmed” by these functional groups. MOFs constructed in this way give rise to exceptional gas adsorption characteristics, unexpected stability towards water vapour, and tunable catalytic properties.

Contributions

All the work in this thesis was completed by Lujia Liu

<u>except</u>

- All elemental analyses were performed by the Campbell Microanalytical Laboratory at the University of Otago, New Zealand.
- Some gas adsorption isotherms presented in Chapter 2 and 3 were measured by Dr. Matthew Hill and Dr. Kristina Konstas at CSIRO.
- Truxene, H_3hmtt, and a precursor of H_3hett were synthesized by David Lun. David Lun also conducted scale up recrystallization of some truxene-based ligands.
- ES-MS analyses for H_3hbtt and H_3hhtt were conducted by Dr. Marie Squire at University of Canterbury
- David Perl wrote a computer script to extract the data presented in Figure 4.21.
- H_2**L1**-Boc and H_2**L1** (Chapter 5), which were fully characterized in his previous work, were provided by David Lun.[1]

Acknowledgements

I would like to take the opportunity to thank the large number of people who have contributed to my PhD research and thesis. First, I would like to thank my supervisor Associate Professor Shane Telfer for providing me this wonderful PhD opportunity and scholarship to carry out research in MOF chemistry. Thanks for his enthusiastic, encouraging and patient guidance to my research from the big picture all the way to technical details. Thanks for providing funding for me to attend conferences and visit Professor Randy Snurr's group in Northwestern University.

I would also like to thank my co-supervisor, Professor Geoff Jameson, for his much-valued guidance in crystallography and other scientific discussions during my research and thesis writing. I still remembered the day that he helped us to solve the structure of MUF-7a which set this thesis in motion. I also thank Dr. Pat Edwards for assisting specialized NMR experiments, Associate Professor Gareth Rowlands for discussions and advice on organic synthesis, Dr. Hui Yang for his assistance with isotherm data analyses, David Perl for writing a computer script that greatly assisted to process simulation results, Amy Toms for help with fluorescence spectroscopy, Trevor Loo and Dr. Vyacheslav Filichev for their technical assistance, and Jianyu Chen, Jordan Taylor, Niki Murray, and Dr. Matthew Savoian's assistance in optical, confocal, and scanning electron microscopy. I also thank Sebastian Blackwood, Heather Jameson, Dr. Alan Ferguson and all other current and past Telfer group members for scientific discussions and technical assistance.

A special acknowledgement goes to David Lun for his much-valued technical assistance in organic synthesis, HPLC, ES-MS, NMR training and providing some valuable ligands.

I thank Professor Randy Snurr for hosting my visit and all his group members, especially Dr. Pritha Gosh, for their training and assistance in computational MOF chemistry. I must also thank Dr. Matthew Hill, Dr. Kristina Konstas and Dr. Aaron Thornton for their assistance in measuring gas adsorption isotherms and related calculations.

I thank NeSI for providing computational resources, staff from Campbell Microanalytical Laboratory at the University of Otago for elemental analyses, Dr. Geoff Waterhouse from University of Auckland for measuring a preliminary gas adsorption isotherm, Dr. Marie Squire from University of Canterbury for some ES-MS experiments, Dr. Jack Evans for generating some hypothetical MOF structures, and Dr. Yonghwi Kim

and Professor Kimoon Kim from Pohang University of Science and Technology for generously providing a trial sample of H_3hmtt.

I would like to acknowledge the financial support from The MacDiarmid Institute for Advanced Materials and Nanotechnology for a Doctoral scholarship, Institute of Fundamental Sciences for my fourth year PhD funding, and the Chinese Scholarship Council for an Outstanding Chinese PhD student award. I also thank the IFS postgraduate travel fund and New Zealand Institute of Chemistry travel fund for supporting me to attend conferences in Dunedin, Edinburgh and Kobe, and to visit Professor Randy Snurr's group in Chicago. I greatly thank the MacDiarmid Institute for organizing and supporting annual student and postdoc symposiums and AMN-7 conference in Nelson (special thanks to Associate Professor Shane Telfer for organizing this conference).

I also thank IFS administration and technical staff for their great assistance during my PhD research and thesis writing.

Finally, I must thank my family for their support and encouragement over the last few years. Especially I would like to thank my wife Minxuan Du for her great help, understanding and support.

Abbreviations

ANG	adsorbed natural gas
BET	Brunauer-Emmett-Teller
CNG	compressed natural gas
CSIRO	Commonwealth Scientific and Industrial Research Organization
DEF	*N*,*N*-diethylformamide
DFT	density functional theory
DMF	*N*,*N*-dimethylformamide
DOE	U.S. Department of Energy
GCMC	Grand Canonical Monte Carlo
HKUST	Hong Kong University of Science and Technology
IRMOF	isoreticular metal-organic framework
IUPAC	International Union of Pure and Applied Chemistry
LNG	liquefied natural gas
MAF	metal azolate framework
MC	multicomponent
MC-MOF	multicomponent metal-organic framework
MCP	microporous coordination polymer
MIL	Matérial Institut Lavoisier
MOF	metal-organic framework
MTV	multivariate
MTV-MOF	multivariate metal-organic framework
MUF	Massey University framework
NMR	nuclear magnetic resonance
PCN	porous coordination network
PCP	porous coordination polymer
PSA	pressure swing adsorption

PSD	pore size distribution
PSM	postsynthetic modification
PXRD	powder x-ray diffraction
RH	relative humidity
SBU	secondary building unit
SC-XRD	single crystal x-ray diffraction
SEM	scanning electron microscopy
STP	standard temperature and pressure
SUMOF	Stockholm University metal-organic framework
TGA	Thermogravimetric analysis
TSA	temperature swing adsorption
UiO	University of Oslo
UMCM	University of Michigan crystalline material
VSA	vacuum swing adsorption
XRD	X-ray diffraction
ZIF	zeolitic imidazolate framework

Reference chart of common ligands

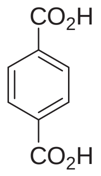

H_2bdc

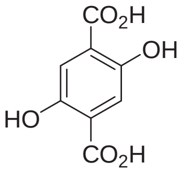

H_2dobdc

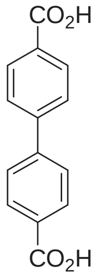

H_2bpdc

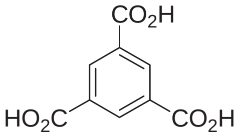

H_3btc

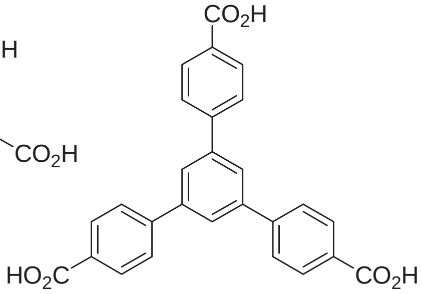

H_3btb

Reference chart of common metal clusters

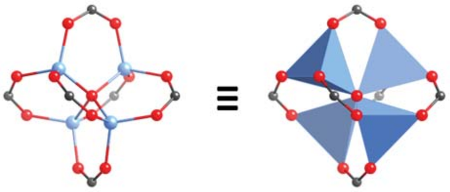

$Zn_4O(CO_2)_6$ cluster

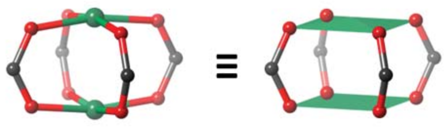

$M_2(CO_2)_4$ paddle-wheel cluster
M = Cu(II), Zn(II)

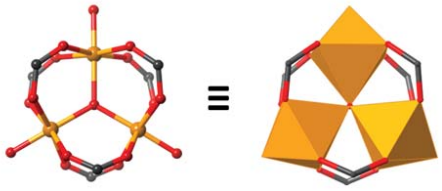

$M_3O(CO_2)_6(H_2O)_2X$ cluster
M = Cr, Fe, V, Sc; X = F, Cl, OH

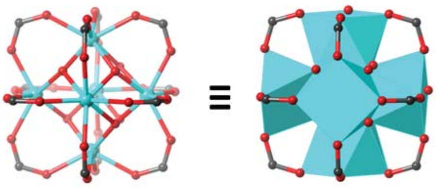

$Zr_6O_4(OH)_4(CO_2)_{12}$ cluster

Publications and thesis structure

Publications relevant to this thesis

1. **L. Liu** and S. G. Telfer, Systematic Ligand Modulation Enhances the Moisture Stability and Gas Sorption Characteristics of Quaternary Metal-Organic Frameworks, *J. Am. Chem. Soc.* **2015**, 137, 3901-3909.

   I carried out the experimental and computational work, put together the electronic supporting information, and wrote the first draft of this paper.

2. **L. Liu**, K. Konstas, M. R. Hill and S. G. Telfer, Programmed Pore Architectures in Modular Quaternary Metal-Organic Frameworks, *J. Am. Chem. Soc.* **2013**, 135, 17731-17734.

   I carried out the experimental and computational work, put together the electronic supporting information, and contributed to the writing of this paper.

Additional publications

3. J. Sirirak, D. J. Harding, P. Harding, K. S. Murray, B. Moubaraki, **L. Liu** and S. G. Telfer, Spin Crossover in *cis* Maganese(III) Quinolylaldiminates, *Eur. J. Inorg. Chem.* **2015**, 2015, 2534-2542.
4. J. Sirirak, D. J. Harding, P. Harding, **L. Liu** and S. G. Telfer, Solvatomorphism and Electronic Communication in Fe(III) N,N-Bis(salicylidene)-1,3-propanediamine Dimers, *Aust. J. Chem.* **2015**, 68, 766-773.
5. A. Ferguson, **L. Liu**, S. Blackwood and S. G. Telfer, Recent Developments in Metal-Organic Framework (MOF) Chemistry, C*hemistry in New Zealand* **2014**, 78, 113-118.
6. D. J. Harding, W. Phonsri, P. Harding, I. Gass, K. S. Murray, B. Moubaraki, J. D. Cashion, **L. Liu** and S. G. Telfer, Abrupt Spin Crossover in an Iron(III) Quinolylsalicylaldimine complex: Structural Insights and Solvent Effects, *Chem. Commun.* **2013**, 49, 6340-6342.
7. A. S. Gupta, R. K. Deshpande, **L. Liu**, G. I. N. Waterhouse and S. G. Telfer, Porosity in Metal-Organic Frameworks Following Thermolytic Postsynthetic Deprotection: Gas Sorption, Dye Uptake and Covalent Derivatisation, *CrystEngComm* **2012**, 14, 5701-5704.

Table of Contents

Chapter 1

Introduction

1.1 General introduction to metal-organic frameworks

1.1.1 Definition, terminology and nomenclature

MOFs are a class of two or three dimensional porous materials. They are constructed with metal ions or metal-containing clusters and divergent organic linkers that bridge multiple metal ions or clusters into network-like structures. According to IUPAC recommendations, *a metal-organic framework, abbreviated to MOF, is a coordination network with organic ligands containing potential voids*.[2] Here, a coordination network refers to *a coordination compound extending, through repeating coordination entities, in one dimension, but with cross-links between two or more individual chains, loops, or spiro-links, or a coordination compound extending through repeating coordination entities in two or three dimensions.* IUPAC also defines a coordination polymer as *a coordination compound with repeating coordination entities extending in one, two, or three dimensions.* As shown in Figure 1.1, MOFs are a subset of coordination networks which are again a subset of coordination polymers.

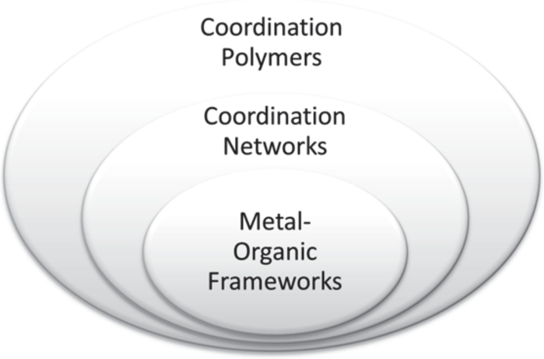

Figure 1.1 A diagram showing that MOFs are a subset of coordination networks, and that coordination networks are further subset of coordination polymers.

There are other terms that individual research groups use, or formerly used, in place of MOFs, such as porous coordination polymers (PCPs, by Kitagawa's group), porous coordination networks (PCNs, by Zhou's group), and microporous coordination polymers (MCPs, by Matzger's group). Materials initially reported using these terms are also classified as MOFs in this thesis.

An IUPAC task group is currently revising the nomenclature of coordination and inorganic polymers.[2] Generally, when referring to a MOF, its nickname (e.g. MOF-5[3]) or abbreviated formula [e.g. Mg_2(dobdc),[4-6] dobdc = 2,5-dioxido-1,4-benzenedicarboxylate], are commonly used. IUPAC also agrees researchers can give important new compounds trivial names based on their place of origin followed by a number, such as HKUST-1 (HKUST = Hong Kong University of Science and Technology),[7] MIL-101 (Matérial Institut Lavoisier),[8] and UiO-66 (UiO = University of Oslo).[9] Systematic nomenclature is usually avoided because it is too cumbersome. In some cases, when a formula is not a unique description of a MOF and can cause ambiguity, its nickname is preferred. For instance, MIL-101[8] / MIL-88B[10] and MOF-177-NH_2 / UMCM-308[11] are two pairs of polymorphic frameworks[11] with common abbreviated formulae, $Cr_3O(H_2O)_2F(bdc)_3$ (bdc = benzene-1,4-dicarboxylate) and $Zn_4O(atb)_2$ [atb = 2,4,6-tris(4-carboxyphenyl)aniline], respectively. Also, MUF-177, [12] Zn/btb-ant and Zn/btb-tsx[13] have the same formula: $Zn_4O(btb)_2$ [btb = 1,3,5-tris(4-carboxyphenyl)benzene]. IRMOF-9 and IRMOF-10 are closely related versions of $Zn_4O(bpdc)_3$ (bpdc = biphenyl-4,4′-dicarboxylate). IRMOF-10 has an open lattice while IRMOF-9 is doubly interpenetrated *i.e.*, a second copy of the framework grows inside the pores of the first.

1.1.2 A brief history of MOFs

The antecedents of MOF materials can be traced as far back as 1706 when Prussian blue was synthesized as a pigment. Its X-ray single crystal structure shows that six-coordinated Fe(II) and Fe(III) ions are connected by a linear divergent ligand CN^-, forming a three-dimensional framework-like polymeric structure with a cubic network topology (Figure 1.2). Prussian blue is a typical example of a coordination polymer. The regularity, simplicity, and beauty of this highly symmetrical cubic network inspired MOF chemists to construct materials with similar structures.

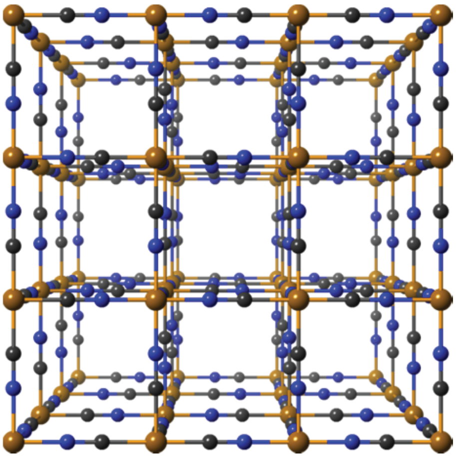

Figure 1.2 X-ray single crystal structure of Prussian blue $Fe_4[Fe(CN)_6]_3$.[14] Water molecules in the lattice are omitted for clarity. To generate a structure displaying alternating orientation of the cyano groups, the *P*m3m space group was chosen. Colour code: brown: iron; grey: carbon; blue: nitrogen.

In 1990,[15] Robson proposed that spontaneous self-assembly between four-coordinated tetrahedral or six-coordinated octahedral metal nodes and rod-like linear divergent organic ligands could potentially lead to materials with the following features:

1) High crystallinity, porosity, thermal, chemical, and mechanical stability with low density;
2) Pores that allow the diffusion, inclusion and separation of guest molecules;
3) Post-synthetic modification of the organic ligands, i.e. chemical modification of the ligands following their incorporation into the network structure;
4) Catalytically-active sites in the material for heterogeneous catalysis applications;
5) Cooperative catalytic activity between multiple sites.

As will now be outlined, over the past 25 years, most of these remarkable properties have been achieved in MOFs.

The term metal-organic framework was first used by Yaghi in 1995.[16,17] However, the properties of the two compounds, $Cu_2(4,4'\text{-bipy})_3(NO_3)_2$[16] and Co(btc)(pyridine)[17], reported at that time did not really distinguish themselves from other coordination polymers. The real breakthrough happened in 1999 when Yaghi and Williams independently reported two materials: MOF-5[3] and HKUST-1.[7]

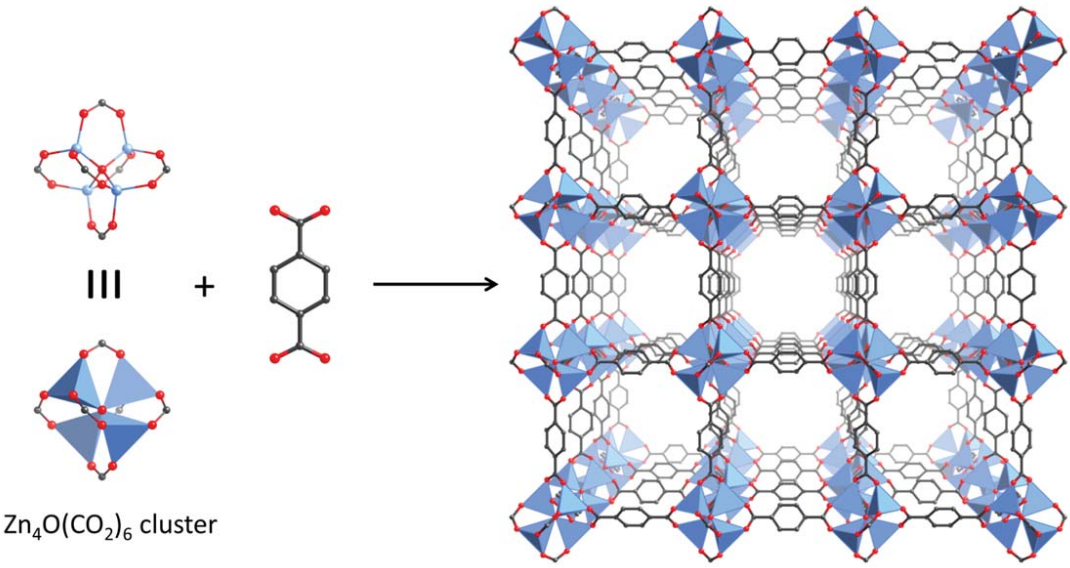

Figure 1.3 A scheme showing the conceptual route to MOF-5 by linking bdc ligands with tetranuclear zinc(II) nodes. Right: X-ray single crystal structure of MOF-5 featuring a cubic network topology (**pcu**). Hydrogen atoms are omitted for clarity. Colour code: blue: zinc; grey: carbon; red: oxygen.

MOF-5 was synthesized from zinc nitrate and 1,4-benzenedicarboxylic acid (H_2bdc). It features a cubic network (**pcu**) structure just like Prussian blue (Figure 1.3). The six-coordinate iron cations are replaced by $Zn_4O(CO_2)_6$ clusters and the cyano anions by linear bdc ligands. This zinc cluster is known from the crystal structure of basic zinc acetate $Zn_4O(CH_3CO_2)_6$.[18] The rational concept of linking existing metal carboxylate cluster chemistry with divergent organic ligands to form preconceived networks distinguished this approach from shake-and-bake chemistry. The report of MOF-5 caused great excitement because it:

1) Showed permanent porosity upon guest removal. Traditional coordination polymers synthesized with single metal nodes are usually somewhat flexible and can transform to denser phases after guest removal, thus precluding permanent porosity.

2) Displayed the highest porosity and surface area ever recorded. Its Langmuir surface area was calculated to be 2900 m^2/g and pore volume 1.04 cm^3/g. It was later found that by using optimal synthetic conditions and careful handling, its BET (Brunauer-Emmett-Teller[19]) surface area can be as high as 3800 m^2/g (4400 m^2/g for the Langmuir surface area).[20]

3) Is thermally stable up to 300 °C. This is another benefit of using metal carboxylate cluster nodes in place of metal cations. The binding strength between such clusters and

carboxylate ligands are stronger than coordination bonds between single metal cations and neutral organic ligands (see section 1.1.5.1 for further discussion).

As mentioned above, **pcu** is the symbol of a cubic network. Network symbols are usually described with three lower cases letter in bold. Detailed information regarding network symbols can be found in the literature.[21]

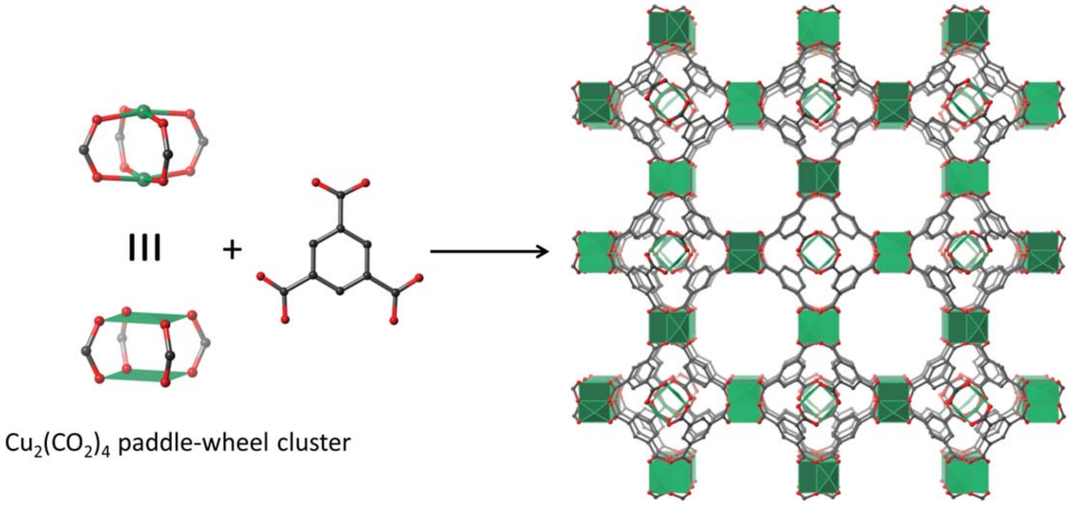

Figure 1.4 A scheme showing the conceptual route to HKUST-1 by linking btc ligands with dinuclear copper(II) paddlewheel nodes. Right: single crystal X-ray structure of HKUST-1 featuring a **tbo** network topology. Hydrogen atoms are omitted for clarity. Colour code: green: copper; grey: carbon; red: oxygen.

HKUST-1 was synthesized from copper nitrate and benzene-1,3,5-tricarboxylic acid (H_3btc). It has a three-dimensional network structure with **tbo** topology. HKUST-1 is also permanently porous upon the removal of occluded solvent molecules, and it has a high BET surface area (1850 m^2/g in a later study[22]). In the original report, the coordinated water occupying the axial coordination sites of the paddlewheel clusters of the as-synthesized material was removed to reveal open metal sites (coordinatively unsaturated metal sites, also known as exposed metal sites). These open metal sites can bind to introduced pyridine. This is one of the very earliest examples of the postsynthetic modification (PSM) of a MOF (the term post-synthetic modification was later used by Cohen in 2007).[23] PSM is the chemical modification of a MOF following its synthesis. This includes 1) Removal of coordinated small molecules to reveal open metal sites.[24-26] 2) Introduction of new ligands into the framework by coordinating to open metal sites.[6,27-30] 3) Chemical functionalization of the organic ligands.[31] 4) Deprotection of organic ligands to reveal functional sites using thermolabile[1,32,33] and photolabile[34-36] protecting groups.

5) Postsynthetic ligand and metal exchange[37-39] (PSE, also known as solvent assisted linker exchange,[40,41] SALE). 6) Postsynthetic metalation of open Lewis base sites.[42-44]

The open metal sites and ability to be chemically modified post-synthetically lead to some amazing properties of HKUST-1: to date, it is still the record-holding material for methane storage;[22,45] TCNQ (7,7,8,8,-tetracyanoquinododimethane) functionalized HKUST-1 shows ultrahigh electrical conductivity;[46] and can act as a heterogeneous catalyst.[47-49] HKUST-1 is less water sensitive than MOF-5 so it can be conveniently handled in air.[50]

Notably, merging metal carboxylates and traditional coordination polymers to construct MOFs was not a straightforward quest. Clues can be found in three MOFs reported prior to MOF-5: MOF-2, MOF-3 and MOF-4, in which zinc(II) and bdc ligands combine under different synthetic conditions.[51-53] To construct the target $Zn_4O(CO_2)_6$ cluster of MOF-5 the synthetic method was complicated: hydrogen peroxide was used to generate the μ_4-oxygen that sits at the centre of the tetranuclear zinc(II) cluster. This synthetic protocol was greatly improved in 2002 when Yaghi's group found that simply heating zinc nitrate and H_2bdc in DEF (*N,N*-diethylformamide) could afford MOF-5 crystals. This method is also generally applicable to fifteen other MOFs reported in the same paper.[54] Solvothermal reactions of organic ligands in combination with a metal source in DMF (*N,N*-dimethylformamide), DEF or other formamide solvents has become a general synthetic protocol for zinc(II)-carboxylate MOFs.[12,55-57] It is generally believed that trace water in the reaction mixture can serve as the source of the central μ_4-oxygen of the $Zn_4O(CO_2)_6$ clusters and the use of hydrogen peroxide is not necessary.[58]

Another milestone established in Yaghi's 2002 paper is that ligands that are chemically functionalized or elongated are compatible with this general synthetic route. As shown in Figure 1.5, under the same reaction conditions, all of these ligands can form MOFs with the same overall network structures. Because the resulting frameworks share the same network topology, these MOFs are categorized as isoreticular MOFs (IRMOFs). Isoreticularity is a very important concept in MOF chemistry. The term is derived from "reticular synthesis", which is described as *the process of assembling judiciously designed rigid molecular building blocks into predetermined ordered structures (networks), which are held together by strong bonding.*[59]

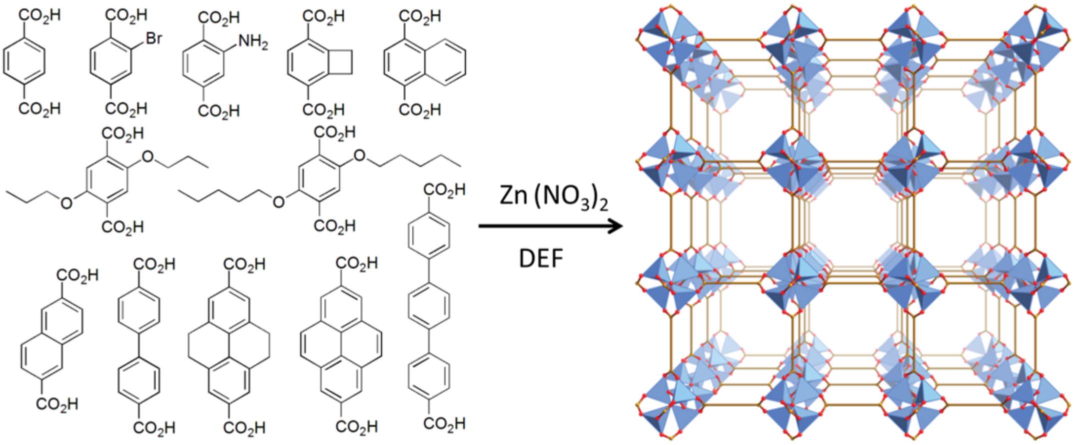

Figure 1.5 Isoreticular MOFs synthesized from ligands that are differently functionalized or altered in their lengths.

An exponential expansion of MOF chemistry started at that time. Since 2009, the number of publications on metal-organic frameworks produced each year has exceeded that of coordination polymers (Figure 1.6). The actual number of publications on MOFs are underestimated because some research groups used (or are still using) alternative terms instead of "MOF".

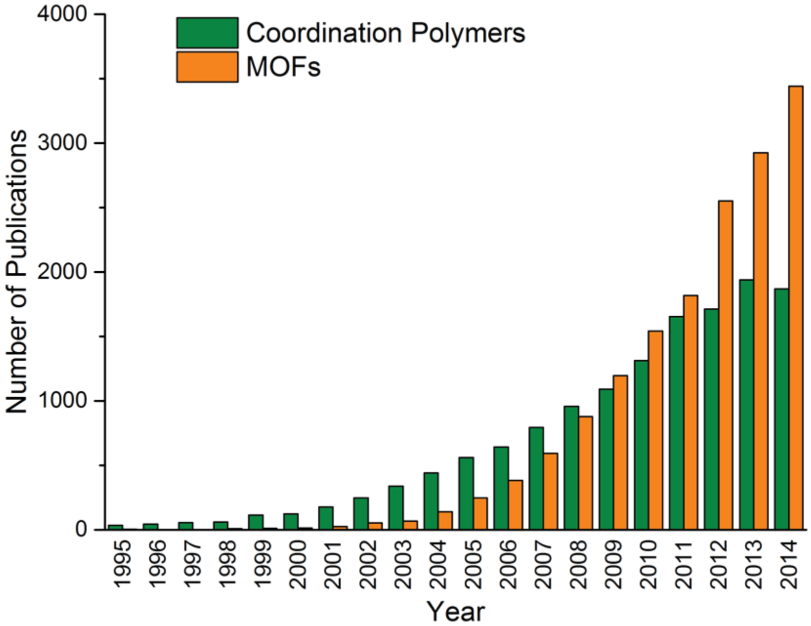

Figure 1.6 Number of publications with the topic coordination polymers (green) and metal-organic frameworks (orange) in the past 20 years (source: SciFinder, 15/05/2015).

1.1.3 Other archetypal MOFs

MIL-101 was reported by Ferey's group in 2005.[8] It was initially synthesized under hydrothermal conditions by mixing chromium(III) nitrate and H_2bdc in the presence of hydrofluoric acid. HF-free synthetic conditions were developed later.[60] Four six-connected $Cr_3O(H_2O)_2F(CO_2)_6$ clusters and six bdc ligands define the vertices and edges, respectively, of a tetrahedral cage (Figure 1.7). Each tetrahedral cage is linked with four other identical cages through sharing their vertices. An **mtn** network that has the same topology as zeolite MTN is produced.[61-63] This framework features two types of mesopores which have diameters of 29 Å and 34 Å. MOFs with such large pores were very rare at that time.[61,62] These large pores enable MIL-101 to encapsulate a lacunary Keggin anion $PW_{11}O_{39}^{7-}$ with a diameter of 13.1 Å. The hydrolytic and chemical stability of MIL-101 together with MIL-100[61] set another milestone in MOF history because most of the MOFs reported earlier are prone to hydrolysis when exposed to atmospheric water vapour or liquid water.[8,50,64-70] This superior stability makes MIL-101 compatible with sulfonic acid functional groups and the corresponding MOF, MIL-101-Cr-SO_3H, can be used as a solid Brønsted acid catalyst.[71,72] The coordinated water molecules on the $Cr_3O(H_2O)_2F(CO_2)_6$ cluster can be removed to reveal open metal sites, and these open metal sites can be further functionalized for enantioselective catalysis[73] and selective gas adsorption.[28,29,74] For instance, polyethyleneimine functionalized MIL-101s have shown great promise in real-life flue gas treatment and natural gas purification systems because of their high performance, excellent stability and low cost.[28,29,74] When replacing chromium by other trivalent metals, such as Fe(III)[75], Sc(III)[76] and V(III),[77] isoreticular frameworks can be obtained. Among these variants, iron based MILs are biodegradable and exhibit acceptably low biotoxicity. Their potential applications in biomedical imaging and drug delivery have been investigated.[78,79]

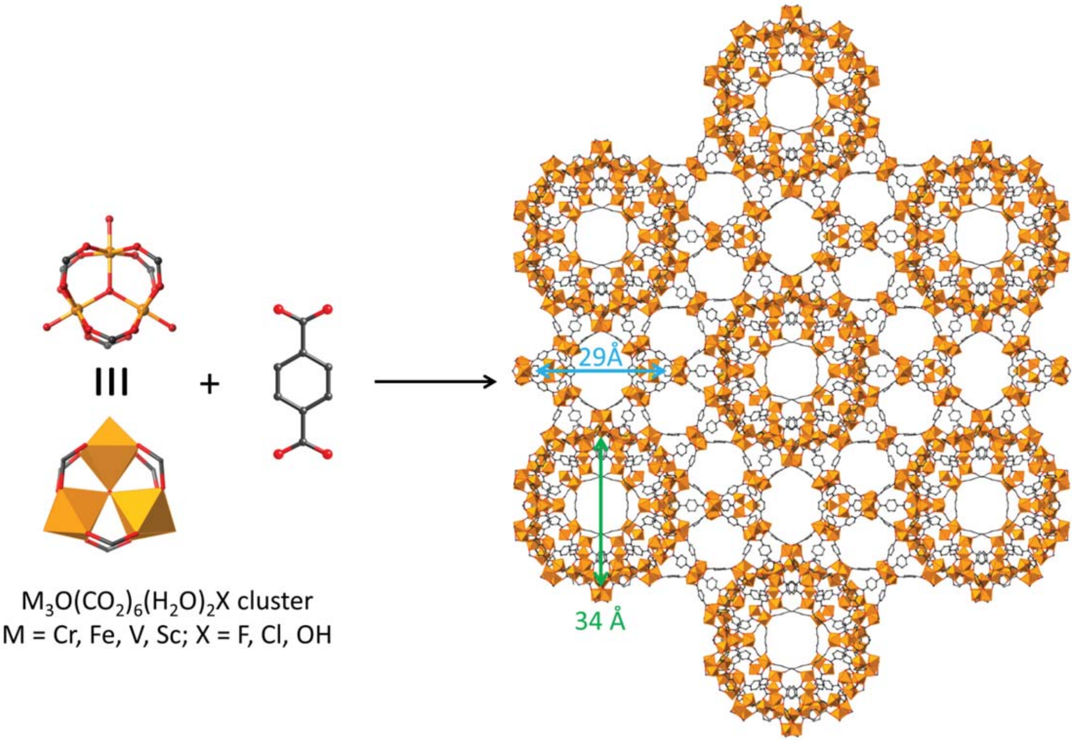

Figure 1.7 A scheme showing the conceptual route to MIL-101 by linking bdc ligands with trinuclear trivalent metal nodes. Right: X-ray single crystal structure of MIL-101 featuring two types of mesopores. Hydrogen atoms are omitted for clarity. Colour code: orange: chromium; grey: carbon; red: oxygen.

UiO-66 was reported by Lillerud's group in 2008.[9] It was synthesized from zirconium(IV) chloride and H_2bdc in DMF. Twelve-connected $Zr_6O_4(OH)_4(CO_2)_{12}$ clusters are linked by linear bdc linkers into a **fcu** network. UiO-66 is also found to be extremely stable in water, aqueous acid, base and common organic solvents.[80] The $Zr_6O_4(OH)_4(CO_2)_{12}$ cluster is the key to its stability due to its high thermodynamic stability.[81] The hydrolysis of the first carboxylate site has an energy penalty of 38.2 kcal mol^{-1}.[82] The stability of UiO-66 makes it highly tolerant to a wide range of ligand functional groups which are typically incompatible with other MOFs.[83-87] Both the metal and organic ligands of UiO-66 can be exchanged post-synthetically to deliver UiO-66 derivatives that are unable to be synthesized directly.[37,39] The $Zr_6O_4(OH)_4(CO_2)_{12}$ cluster has also been used to construct other MOFs with high porosity and extraordinary stability towards acids and bases.[88-94]

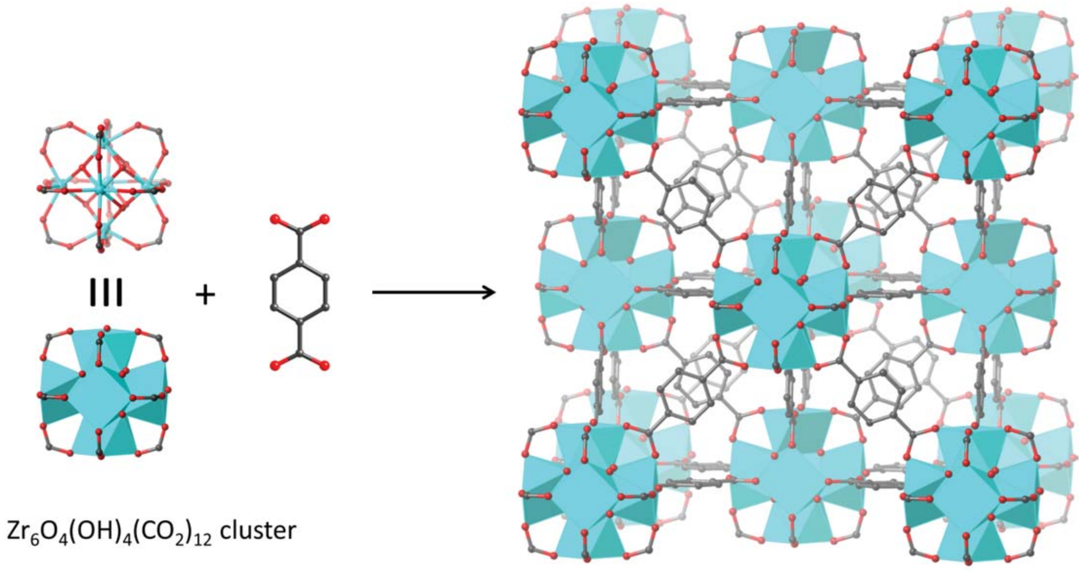

Figure 1.8 A scheme showing the conceptual route to UiO-66 by linking bdc ligands with hexanuclear nodes. Right: X-ray single crystal structure of UiO-66 featuring a cubic network topology (**fcu**). Hydrogen atoms are omitted for clarity. Colour code: blue: zinc; grey: carbon; red: oxygen.

ZIF-8 (ZIF = zeolitic imidazolate framework), also known as MAF-4 (MAF = metal azolate framework), was first reported by Chen's group in 2006.[95] Later in the same year, Yaghi's group independently reported the same compound, and found it to be extremely stable in water and aqueous base (boiling 8 M NaOH).[96] It is synthesized from zinc nitrate and 2-methylimidazole in DMF or water.[97] The hydrolytic stability of ZIF-8 can be explained by the strong coordination bond between the zinc cation and imidazolate nitrogen atoms. However, ZIF-8 is very sensitive to acid. The effective cage diameter of ZIF-8 is 12.5 Å with a window size about 3.3 Å.[95]

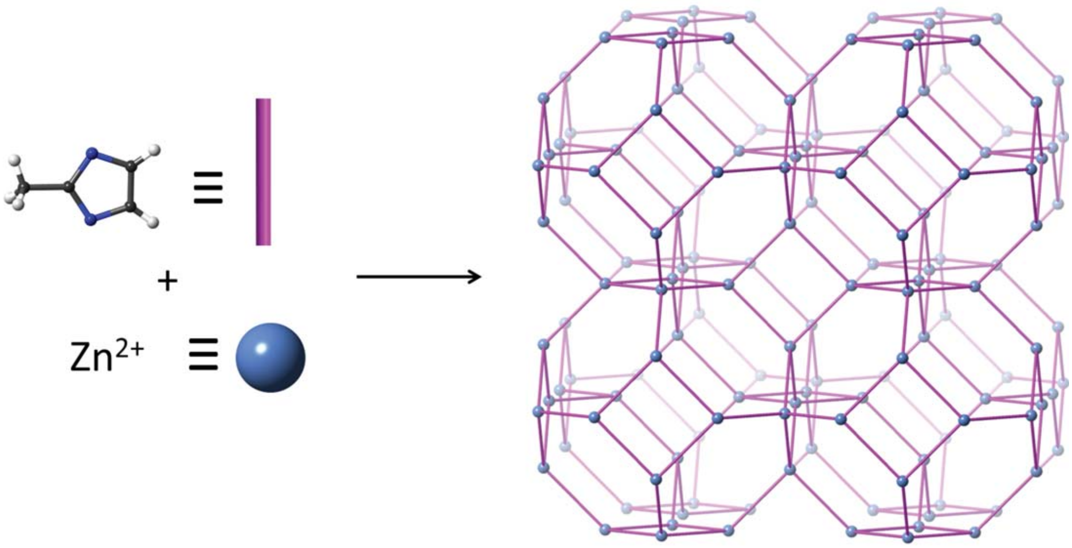

Figure 1.9 A scheme showing the conceptual route to ZIF-8 by linking 2-methylimidazolate ligands with mononuclear Zn(II) nodes. Right: X-ray single crystal structure of ZIF-8 featuring a **sod** network topology that resembles sodalite. Hydrogen atoms are omitted for clarity. Colour code: blue: zinc; purple: 2-methylimidazole.

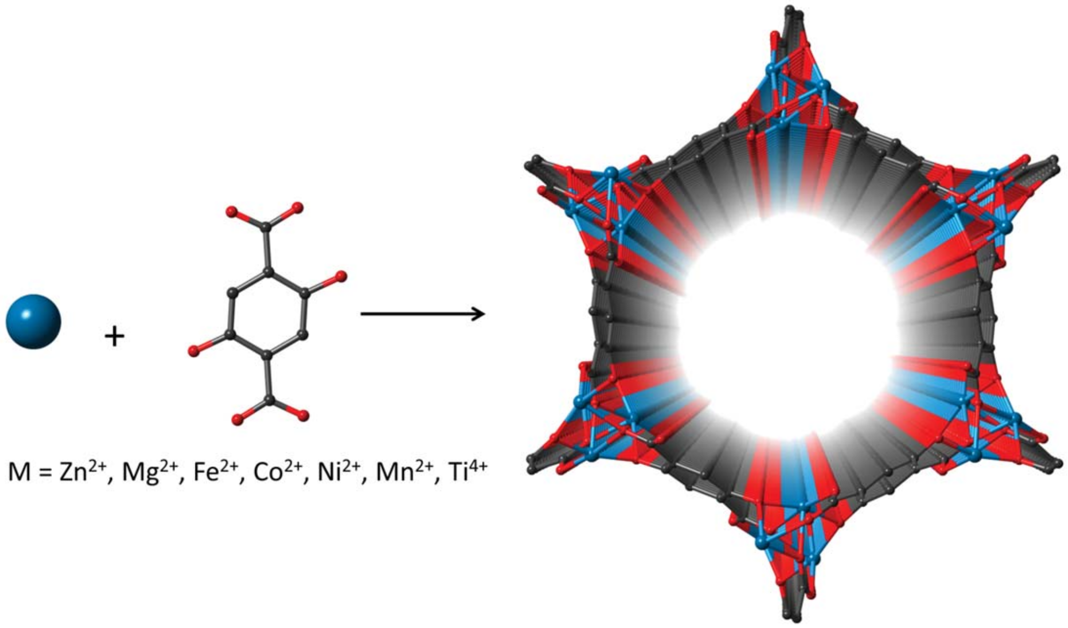

Figure 1.10 A scheme showing the synthetic route to MOF-74. Right: X-ray single crystal structure of MOF-74 featuring a one-dimensional channels. Hydrogen atoms are omitted for clarity. Colour code: blue: M^{2+}; grey: carbon; red: oxygen.

Zn-MOF-74, also known as CPO-27-Zn or Zn$_2$(dobdc) (dobdc = 2,5-dihydroxo-1,4-benzenedicarboxylate), was first reported by Yaghi's group.[98] The metal cations are coordinated with both phenoxide and carboxylate oxygens from the ligand to form a one-dimensional infinite chain. MOF-74s feature hexagonal 1D channels (Figure 1.10) and the channel diameter can be tuned by changing the length of the ligand.[99] The MOF with the largest channel of 85 Å is constructed with a ligand that is 50 Å long (Figure 1.11) and it is large enough to encapsulate green fluorescent proteins.[99] Many other divalent metals can form MOF-74 structures such as Co(II),[100] Ni(II),[25] Mn(II, III),[101] Mg(II),[4,6,27] and Fe(II, III).[102-104] MOF-74 containing 10 different metals are also known.[105]

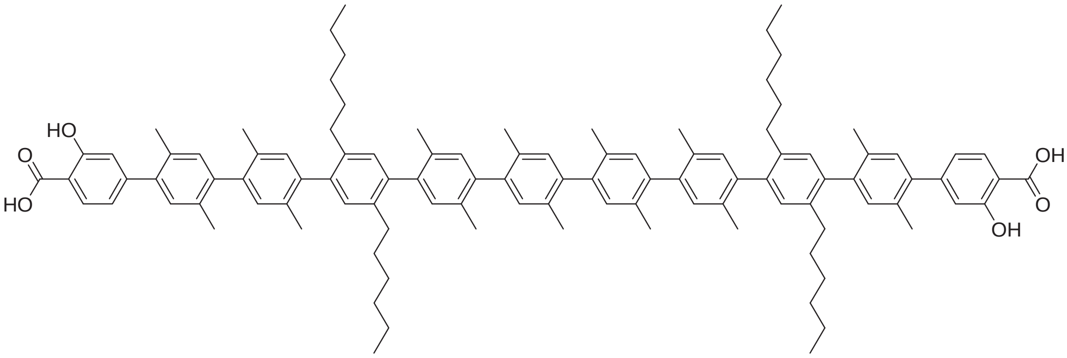

Figure 1.11 Structure of an elongated ligand that generates an isoreticular MOF-74 featuring a 85 Å diameter channel.

Coordinated water molecules in MOF-74s can be removed to reveal open metal sites. Fe-MOF-74 with open metal sites can effectively separate olefin/paraffin mixtures.[103] It can also oxidize ethane to ethanol by N_2O when the iron(II) sites are diluted with magnesium(II).[104] Open metal sites in MOF-74 can be also further functionalized for various purposes. For example, Long's group has demonstrated that a series of ethylenediamine functionalized MOF-74s [mmen-M_2(dobpdc), M= Mg, Mn, Fe, Co, Zn].[6,27,106] can adsorb a significant amount of CO_2 at low pressure. Among these MOFs, mmen-Mg_2(dobpdc) and mmen-Mn_2(dobpdc) have shown great promise for the capture of CO_2 from flue gas mixtures, especially at high working temperatures.[6]

Figure 1.12 shows how many times these typical MOFs were mentioned in the literature. It should be noted these numbers are well underestimated for MOF-5, HKUST-1, and MOF-74 because of their many alternative names.

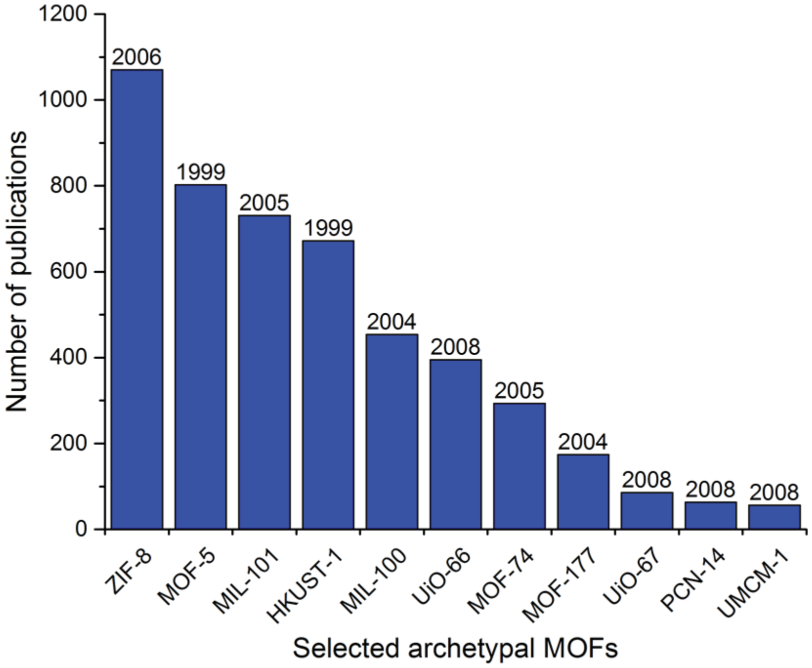

Figure 1.12 The number of publications containing the exact names of some typical MOFs. The number on each bar shows when the MOF was first reported. Source: Scifinder, 25th May, 2015.

1.1.4 Synthesis of MOFs

The initial synthesis of MOF-5 involved the slow diffusion of triethylamine into a solution of zinc nitrate and H_2bdc in a solvent mixture of DMF, chlorobenzene and small amount of hydrogen peroxide.[3] At room temperature, triethylamine gradually diffused into the solution to deprotonate the H_2bdc ligand. This triggers the formation of MOF-5. The development of using DEF (or DMF) as a solvent for solvothermal MOF synthesis is based on the well-known acid catalysed decomposition of formamides which can occur in the presence of water at elevated temperature:[107] Diethylamine is produced gradually, which deprotonates H_2bdc and promotes the formation of MOF-5.[11,58]

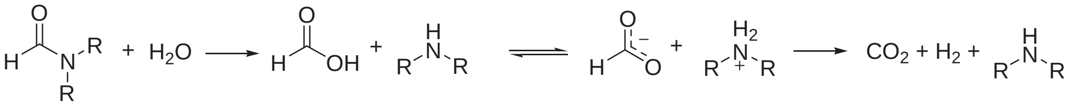

Scheme 1.1 Hydrolysis of formamide solvents in the presence of water generates diethylamine. R = Me, Et, ^{i}Pr, ^{n}Bu.

The concentration of water also plays an important role in the formation of Zn_4O-carboxylate MOFs because in solvothermal reactions water is the source of the central oxide ion. We observed recently that the on-set crystallization time of such MOFs are water-concentration dependent. When using very dry solvents, it takes longer to form MOF crystals. On the other hand, when the water concentration is too high, due to the strong propensity of zinc(II) to coordinate with water, other phases can form.[51-53,98]

When it comes to the syntheses of MOFs that use trivalent or tetravalent metals, modulators are usually used to slow down MOF growth. For example, the structures of UiO-66 (Figure 1.8), UiO-67, and UiO-68 were first solved from powder X-ray diffraction patterns because large single crystals could not be grown.[9] It was later found that the addition of benzoic acid to the reaction mixture afforded a product with better crystallinity and larger crystal size[108] to enable the first single-crystal structure of a zirconium MOF to be determined. The role of the modulator is to compete with the ligand for the metal coordination sites. This reduces the number of viable crystal nuclei that form and promotes the formation of a smaller number of larger crystals rather than a large number of microcrystals.

Solvothermal reactions are usually carried out in scintillation vials (Figure 1.13). The advantage of using glass vials as compared to autoclaves is that the reactions can be monitored easily without changing the reaction temperature. Other conditions such as hydrothermal,[8] microwave,[109] mechanochemical,[110] sonochemical[111] and electrochemical[112,113] reactions are also known to produce MOFs.[114]

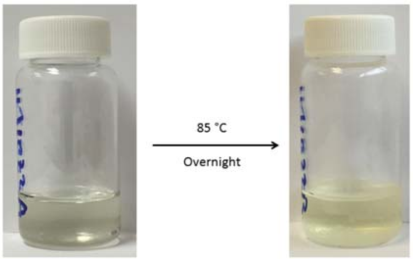

Figure 1.13 Left: a picture of a MOF precursor solution prepared by dissolving ligands and zinc nitrate in DEF. Right: After reacting the precursor solution at 85 °C overnight, colourless MOF crystals were found to grown on the surface of the glass vial.

1.1.5 Structural diversity of metal-organic frameworks

Structural diversity is one of the most fascinating features of MOFs. Unlike other porous materials, such as carbons, zeolites and mesoporous silicas, in which the number of the building blocks and their geometries are very limited, MOFs can draw from a very extensive library of inorganic metal ions and clusters as well as an unlimited array of organic ligands. By February 2015, the total number of MOF structures deposited in the Cambridge Structural Database had already exceeded 100,000.[115]

1.1.5.1 Diversity of inorganic clusters

As shown in the MOF examples described earlier, most MOFs are constructed with metal clusters instead of single metal ions (except for ZIFs). Clusters bring several advantages: 1) Bidentate ligands are often used and being part of the clusters and this aids stability. 2) The flexible geometry of a single metal ion that is coordinated with multiple monodentate ligands can usually cause framework to collapse upon removal of occluded solvent molecules, whereas the rigidity of clusters enables permanent porosity. 3) This rigidity also helps to create materials with predictable structures. 4) The binding energy between organic ligands and clusters is usually higher than that of metal ions and monodentate ligands, thus the resulting frameworks with clusters are more thermally stable.[59,116] The examples show earlier highlight the most typical clusters. $Zn_4O(CO_2)_6$ is six-connected and has octahedral geometry. $Cu_2(CO_2)_4$ is four-connected and adopts square planar geometry. The axial positions of this copper paddlewheel SBU (secondary building unit) can also coordinate with divergent monodentate ligands such as dabco (1,4-diazabicyclo[2.2.2]octane),[117] 4,4′-bipyridine,[118] and SiF_6^- anions[119] as “pillars” to form “pillar-layer” MOFs. $Cr_3F(H_2O)_2(CO_2)_6$ is six-connected and has a trigonal prismatic geometry. This geometry is common for six-connected SBUs that are constructed with trivalent metals. The versatility of SBUs is further described in the literature.[116]

1.1.5.2 Diversity of organic ligands

The essential requirement of the organic ligands used to build up MOFs is that they feature two or more binding sites that can coordinate to different clusters and thus produce a polymeric (rather than discrete) structure. A vast number of ligand structures are compatible with this requirement. Figure 1.14a shows some typical organic linkers: linear ditopic,[120] triangular tritopic,[12] square planar tetratopic,[121] tetrahedral tetratopic,[122,123] and planar hexatopic[124] linkers. These ligands can also be desymmetrized (Figure 1.14b). In addition, functional groups can be also introduced on the ligands to tune to the chemical characteristics of the MOF pores (Figure 1.14c).

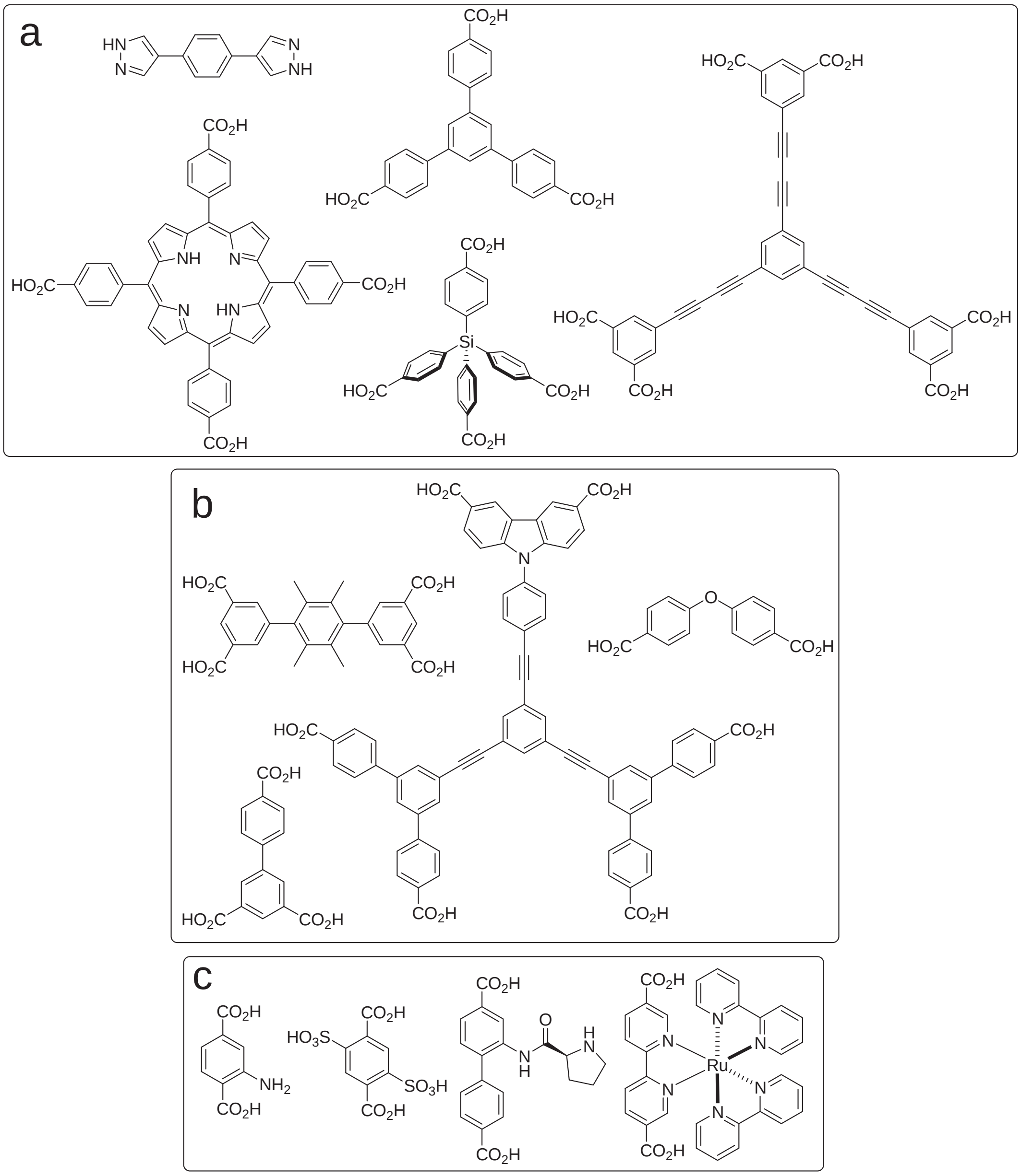

Figure 1.14 Examples of typical organic ligands featuring a) high symmetry with 2-,[120] 3-,[12] 4-,[121-123] and 6-connectivity,[124] b) 2-[125], 3-,[126] 4-,[127] and 6-connectivity[128] with reduced symmetry, c) different functional groups that endow MOFs with useful properties.

1.2 MOFs comprising more than one type of ligand

1.2.1 Multivariate MOFs (MTV-MOFs)

The MTV approach involves co-assembling groups of organic ligands that have the same backbone but different appended functional groups into the same framework. The term MTV-MOF was first used by Yaghi in 2010 when up to eight different ligands

(H_2bdc and its derivatives) were incorporated into a MOF-5 type structure (MTV-MOF-5, Figure 1.15).[129] The most complex MTV-MOF-5 contains eight different ligands. The different ligands are not placed in specific locations in the lattice because they are not well discriminated during MOF growth. Their distribution may not be altogether random, however, and some clustering of ligands is thought to occur. Evidence to support this comes from advanced solid state NMR techniques.[130] The individual ligands do not cluster in specific regions of these crystals, as evidenced by ^{1}H NMR spectra of digested crystal sections. Non-random local distribution of the ligands is probably responsible for the unexpected gas adsorption characteristics of these materials.

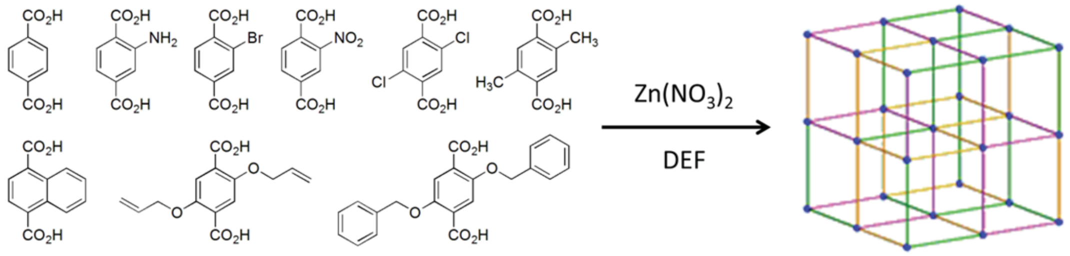

Figure 1.15 A scheme showing that MTV-MOF-5 family are synthesized by mixing multiple ligands from the left hand side ligand library and reacting with zinc nitrate in DEF to afford MOFs comprising multiple ligands.[129]

To the best of my knowledge, the earliest MTV-MOF was reported in 2005 by Kim's group.[131] H_2bdc, H_2tmbdc (tmbdc = 2,3,5,6-tetramethylbenzene-1,4-dicarboxylate), dabco and zinc nitrate are reacted in DMF to form a pillar-layer MOF with a formula $Zn_2(bdc)(tmbdc)(dabco)$. $Zn_2(CO_2)_4$ paddlewheel clusters connect four carboxylate ligands in 2D layers which are linked in the third dimension by dabco "pillars". The position of dabco is distinct from the other two ligands whereas the distribution of bdc and tmbdc ligands is indistinguishable by diffraction experiments and is considered as a solid solution *i.e.*, they are distributed randomly. Cohen's group has recently shown that a MTV-MOF can act as a tandem catalyst by introducing two ligands that have different catalytic moieties.[132] MTV-MOFs can also be built up from sets of different metal ions, rather than different ligands. For example, Yaghi's group demonstrated that up to ten different metals can be incorporated into a MTV-MOF-74.[105]

From these examples, we can see that the MTV approach reliably produces MOFs with predictable lattice structures and containing multiple functional groups. However, this approach lacks of control over the location of these functional groups. This means that the pores of MTV-MOFs are heterogeneous, which is a drawback for applications involving guest adsorption and catalysis. To overcome this challenge, we turned our attention to multicomponent MOFs (MC-MOFs).

1.2.2 Multicomponent MOFs (MC-MOFs)

In contrast to the MTV approach, MC-MOFs are built up from ligands that are geometrically distinct. These ligands are differentiated during the crystallization process and occupy specific positions in the resulting lattice. Therefore, if functional groups are appended to these ligands, they will also be located in precise locations in the framework.

The first MC-MOF, which contains two distinct ligands (H_3btc and H_2bdc) and one metal cluster [$Zn_3(CO_2)_8$], was reported in 2003.[133] This ternary MC-MOFs did not arouse too much attention until 2008, when Matzger's group reported a ternary MOF constructed from Zn_4O clusters, bdc and btb and known as UMCM-1 (UMCM = University of Michigan crystalline material).[55] Since bdc is a linear ditopic ligand and btb is a triangular tritopic ligand, they are located in distinct lattice sites and the framework is ordered and periodic. UMCM-1 also had a recording-breaking BET surface area at that time of 4160 m^2g^{-1}. Since the discovery of UMCM-1, many more ternary MOFs with a ditopic and a tritopic ligands have been reported.[56,134-137] Interestingly, new examples often surpass previous records for the most porous known material.[56,134]

A practical challenge faced when synthesizing MC-MOFs is that the individual ligands can independently form MOFs. This introduces at least two competing phases during the synthesis of a ternary MC-MOF. The production of phase-pure UMCM-1 required careful adjustment of the feed ratio of H_3btb and H_2bdc. High H_3btb/H_2bdc ratios produce phase pure MOF-177 [(Zn_4O(btb)$_2$]$^{[12]}$ or a mixed phase of MOF-177 and UMCM-1, while lower ratios lead to phase pure UMCM-1. If this ratio is too low, however, a mixture of UMCM-1 and MOF-5 is produced. Instead of using a tritopic and a ditopic ligand as described above, it is possible to use two ditopic or two tritopic ligands to synthesize ternary MOFs. For example, SUMOF-4 [Zn_4O(bdc)$_{3/4}$(bpdc)$_{3/4}$],[138] UMCM-8 [Zn_4O(bdc)$_{3/4}$(2,6-naphthalenedicarboxylate)$_{3/4}$],[139] and UMCM-9 [Zn_4O(bdc)$_{3/4}$(2,6-naphthalenedicarboxylate)$_{3/4}$][139] are three examples where two ditopic ligands of different lengths build up ternary MOFs. Lah *et al.* reported an anionic MOF, ($NH_2(CH_3)_2)_3[Zn_6$(btc)$_4$(bdc)], which used two tritopic ligands of different size, btb and btc.[140]

1.3 Applications of metal-organic frameworks

The scope of applications of MOFs is very broad. They can be used in chemical sensing,[141] non-linear optics,[142] electron[143-147] and proton[148-150] conduction, battery cathode materials,[151] photovoltaics,[46] semiconductors,[46,144] guest inclusion,[8,99,152] biomedical imaging,[79] drug delivery,[78,153] cancer therapy,[154] just to name a few areas. *Chemical Society Reviews* has published *two* themed issues on the topic metal-organic frameworks: one in 2009[155] and a recent one in 2014.[156] *Chemical Reviews* also had a MOF themed issue in 2012.[157] A selection of the more important applications of MOFs will be briefly introduced here.

1.3.1 Gas storage and separation

Perhaps the most significant applications of MOFs are in gas storage and separation. Although this was proposed by Robson back in 1990, the prevention of framework collapse upon solvent guest removal was an outstanding challenge.[15] The first breakthrough was made by Yaghi's group when they found MOF-2 to be permanently porous and able to take up ~120 cm^3 of N_2 (at STP) per gram of MOF material at 77 K.[53] After that, various applications for gas storage and separation have been developed.[158-161] These include a hydrogen fuel cell powered vehicle, Mercedes-Benz F125, which uses a MOF as a hydrogen storage material.[162] Other practical applications relating to gas storage and separation have shown great promise, and MOF materials are now in the process of industrialization and commercialization.[163]

1.3.1.1 Natural gas storage

Natural gas is predominantly methane. It has the highest gravimetric energy density and emits the least amount of CO_2 per unit of energy production among all fossil fuels. Because methane has a low boiling point (112 K), it is normally a gas at room temperature. It has a critical point of 190.6 K and 46 bar, which means it is impossible to liquefy methane at room temperature no matter how much pressure is applied.[164] These thermodynamic characteristics make it challenging to provide methane with the volumetric energy density requirements of automobile applications. To tackle this challenge, two technologies have been developed and are most commonly used nowadays: liquefied natural gas (LNG) and compressed natural gas (CNG).

LNG systems are operated at low temperature (111 K) which makes them difficult to be implemented in automobiles. In a CNG system, which operates at room temperature, methane is pressurized to 200-250 bar in an on-board hard container and can provide volumetric energy densities that are 240-290 times greater than methane at atmospheric pressure. There are several drawbacks to this technology: 1) The volumetric energy density is still lower than petroleum or diesel and the fuel tank usually takes up more space. 2) Fuel tank walls are usually very thick to hold that pressure so they are heavy. 3) Such high pressures arouse safety concerns. 4) CNG refuelling stations need to operate at very high pressure so methane can be delivered to the vehicle tanks. This process is very energy intensive and it is very expensive to build the required infrastructure.

Alternatively, adsorbed natural gas (ANG) seems to be a promising solution to overcome these disadvantages. In an ANG system, porous materials are placed in the gas tank to adsorb the fuel gas molecules on their internal surfaces. As a result, most of the methane molecules are adsorbed on the surface and no longer contribute to the bulk pressure. To store the same amount of methane, the pressure of an ANG tank is much lower than that of a CNG system. This could result in lighter and safer natural gas tanks as well as cheaper operation costs. The U.S. Department of Energy (DOE) had set a target for ANG system by 2015: 180 v/v STP at 298 K and 35 bar.[161]

To test whether MOFs can meet this goal, their high pressure methane adsorption isotherms are measured. The first such isotherm was measured in 1997 by Kitagawa's group. A capacity of 77 v/v STP at 30 bar was measured, which means that every volume unit of MOF can adsorb the amount of methane found in 77 volume units at STP.[165] Since then, researchers have been synthesizing new materials with tailored structures with better performance. MOF-5 and MOF-177 showed promise for methane storage in the early stage of MOF history.[54,56] MOF-177 was used to build the first prototype vehicle that is powered by an ANG system with a MOF adsorbent. The vehicle was tested by driving around the world using local natural gas supplies.

In 2007, Zhou's group reported a MOF, PCN-14, showing a methane uptake capacity of 230 v/v STP at 290 K and 35 bar. This capacity is 28% higher than the DOE target and outperformed the best known porous carbon, which has a capacity of ~200 v/v STP.[24] This MOF is constructed with square planar $Cu_2(CO_2)_4$ paddlewheel clusters and a planar tetratopic carboxylate ligand, adip [5,5′-(9,10-anthracenediyl)di-isophthalate]. Upon activation, the coordinated solvent molecules occupying the axial positions of the SBUs are removed to reveal open metal sites. These open metal sites of the copper paddle wheel interact strongly with methane molecules and are believed to be the key to the high methane storage capacity. Since then, a few research groups competitively reported new copper paddlewheel MOFs with open metal sites, exhibiting high methane storage capacity.

Similar materials (PCN-14 and NOTT-107[127]), or even the exact same materials (NU-125[166] and NOTT-122[167]) were reported and published back to back. In addition to these copper paddlewheel MOFs, other MOFs with open sites, such as MOF-74 variants were also investigated and were found to have high methane uptake.[26]

Besides open metal sites, another key structural feature of high methane uptake materials was identified by a computational study conducted by Wilmer, Snurr and co-workers. They selected some existing organic ligands and SBUs and generated a library of nearly 140,000 hypothetical MOF structures *in silico*.[168] By calculating the theoretical methane storage capacities of these materials using a grand canonical Monte Carlo (GCMC) method, an optimal pore size which is the same size (or as twice the size) as a methane molecule was identified, *i.e.*, pores should be 4 Å or 8 Å wide.

In 2013, Hupp's and Long's groups independently published two papers with a striking finding: the MOF material with the highest storage and working capacity for storing methane is actually HKUST-1, which was reported back in 1999 (227 v/v STP at 35 bar, 267 v/v STP at 65 bar, and 190 v/v STP working capacity)![22,45] HKUST-1 has copper paddlewheel clusters with open metal sites and pores with diameter of ~4, 10 and 11 Å. A subsequent in-depth study showed that open metal sites are the primary adsorption sites responsible for adsorbing the methane molecules, which are then distributed throughout the framework cavities.[169]

HKUST-1 has seemingly met the new DOE target for methane storage. However, two practical challenges still need to be considered. 1) The packing loss between individual MOF crystals in an ANG tank would lead to ~25% space being unoccupied. 2) Minor components of the natural gas, especially water vapour, can have much strong binding strengths to open metal sites, which could drastically reduce the storage and working capacity of an ANG system that uses MOFs with open metal sites. 3) Due to the presence of water vapour, the long term stability and capacity of the filling material in an ANG tank also needs to be considered. Copper paddlewheel MOFs and MOF-74 with open metal sites are known to be susceptible to hydrolysis.[81]

To tackle the last two concerns, people are now turning their attention to robust MOFs that are also highly porous. These MOFs are usually constructed with highly charged metal ions, M(III) or M(IV), which are generally known to be resistant to hydrolysis even after being immersed in water. Zirconium(IV) MOFs are currently being widely studied and notable progress has also been made with aluminium(III) MOFs.[170]

MOF-based ANG systems have now been industrialized and thoroughly tested on small and heavy-duty vehicles. Due to the oil price change, BASF has postponed the release of these products into the market. Nevertheless, consumers will likely find them on the market in the next couple of years.[163]

1.3.1.2 CO_2 capture

Global CO_2 emissions exceeded 30 gigatonnes in 2012. 44% of CO_2 emissions come from the burning of coal in electricity plants (Figure 1.16).[171] To prevent CO_2 from being released into the atmosphere, capturing CO_2 from the post-combustion flue gas is potentially the most practical and effective solution. The major component of flue gas is nitrogen (~70%), followed by CO_2 (10-15%), water vapour (10-12%) and other minor gases. To selectively capture CO_2 from the flue gas mixtures, current technology involves using aqueous organic amine solutions. This is a highly effective method but suffers from a major drawback: the desorption of CO_2 from a saturated amine solutions is energy intensive. This is because the desorption of CO_2 requires a high temperature and water has a high thermal capacity. This process typically consumes around 30% of the total energy generated from burning coal.[159] To reduce this energy penalty, porous adsorbents, which have generally lower enthalpies for adsorbing CO_2, are currently being investigated. The tunable pore sizes and chemical characteristics of MOFs make them ideal candidates for flue gas treatment. Some MOFs have already shown great promise and better performance than the current state-of-the-art technology.[6]

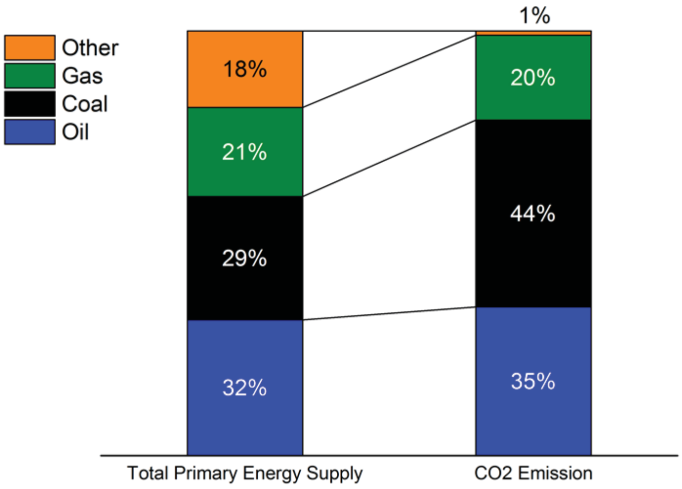

Figure 1.16 Global total primary energy supply and total CO_2 emission contributed by fossil fuel and other energy sources in 2012.

To adsorb CO_2 from flue gas mixtures, several design principles need to be considered. First, the sorbent should be highly selective for CO_2 over other components, especially N_2 and H_2O. Second, the material should be stable to saturated water vapour under standard operating conditions. Third, the working capacity of the material should be as high as possible. And last, the regeneration energy should be optimal, *i.e.*, as low as possible. This implies that the adsorption enthalpy for binding CO_2 should be as low as possible while meeting the first three criteria.

Over the years, researchers have found several strategies that can increase the adsorption selectivity of CO_2 over N_2. For example, open metal sites,[4,49] tuning the window size to allow CO_2 (kinetic diameter = 3.3 Å) to pass through the framework but not nitrogen (kinetic diameter = 3.64 Å),[172] introducing polar functional groups to enhance electrostatic interactions between the framework and CO_2,[28,29,173] and tuning the pore size for optimal CO_2 adsorption.[28,29] However, some of these strategies may have drawbacks for practical applications. First, MOFs constructed with divalent metals with open metal sites are generally susceptible to hydrolysis in the presence of water vapour, and water is more likely to occupy these open metal sites thus reduce the adsorption capacity. Second, blocking nitrogen from entering the MOF pores can cause permeability issues. Third, overly strong non-covalent interactions between the host and CO_2 can increase the heat of adsorption to the point where regeneration of the material is energy intensive.

A recent advance in the field mitigates many of these concerns. In 2015, Long's group reported a series of "phase changing" MOF adsorbents.[6] These MOFs are extended MOF-74 materials with their open metal sites functionalized by *N*,*N′*-dimethylethylenediamine. As shown in Figure 1.17, rather than forming carbamates with dangling uncoordinated amine groups (as originally thought),[103,106] CO_2 molecules are inserted into the metal-nitrogen bond to form infinite one-dimensional carbamate chains. This chain reaction results in cooperative CO_2 capture: negligible adsorption of CO_2 occurs at very low pressures but this is followed by a steep rise in the adsorption isotherm over a very small pressure range (Figure 1.18b). These "phase changing" MOF adsorbents outperform state-of-the-art technologies in several ways: 1) They have exceptionally high working capacities as compared to conventional porous materials (Figure 1.18a). 2) Impressively, these MOFs are capable of working under saturated water vapour and exhibited no loss in working capacities after ten adsorption-desorption cycles. 3) They are capable of adsorbing CO_2 from flue gas at high temperatures. 4) The temperature gap for adsorption and desorption are small so that the energy penalty for sorbent regeneration is low. Long's group has started a company to scale up these "phase changing" MOF adsorbents to implement this technology in coal power plants.

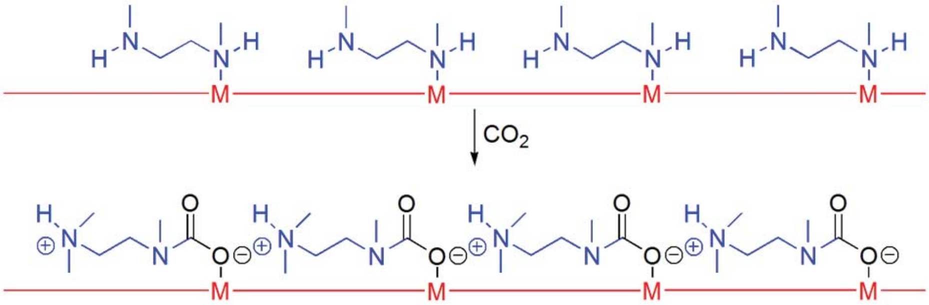

Figure 1.17 A mechanism of CO_2 adsorption in "phase changing" MOF adsorbents: mmen-M_2(dobpdc) (M = Mg, Mn, Co, Fe). CO_2 molecules were inserted into the metal-nitrogen bond to form one-dimensional carbamate chains along the channels of the MOFs.

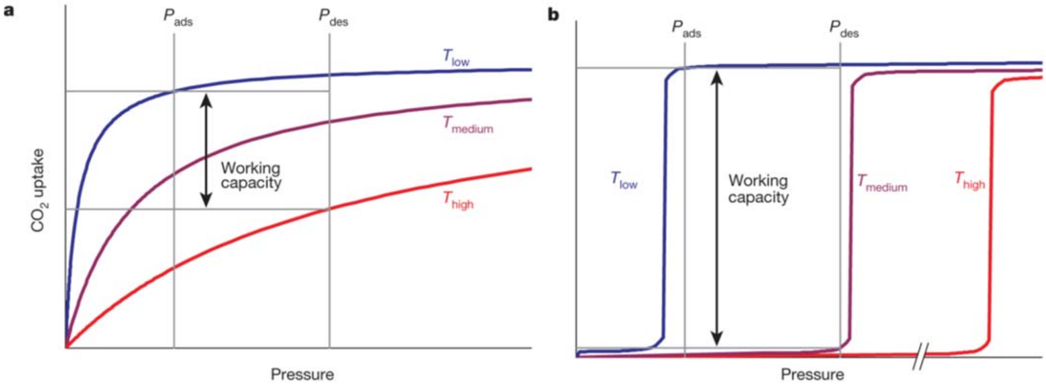

Figure 1.18 A comparison of classical microporous adsorbents (a) and "phase changing" MOF adsorbents (b) showing higher working capacities and lower temperature requirements for "phase changing" MOF adsorbents. Reproduced from reference[6] with permission from Nature Publishing Group.

1.3.1.3 Other separations using MOFs

In industry, gas separation often involves cryogenic distillation. This process is very energy intensive and is usually carried out on a large scale due to its nonlinear cost-scale relationship. As an alternative technology, adsorption-based gas separation is more flexible and cost-effective.[174] Capturing specific gases with an adsorbent is achieved based on the different adsorption characteristics of individual gas components. To release adsorbed gas molecules, adsorbents are treated either by reducing the pressure to one atmosphere (pressure swing adsorption, PSA), applying controlled vacuum to subatmospheric pressure (vacuum swing adsorption, VSA), or heating to a higher temperature (temperature swing adsorption, TSA).[158] The measurement of adsorption isotherms of gas mixtures is difficult therefore the potential of a material to perform gas separations is typically assessed using single component gas adsorption isotherms. These isotherms are fitted using an isotherm model (described below in section 1.4.1) then the gas adsorption selectivity is calculated using ideal adsorbed solution theory (IAST).[175] This yields selectivity as a function of total pressure for a binary gas mixture with known composition. To test materials experimentally for their ability to separate gas mixtures, breakthrough experiments can be conducted. In 2012, Long's group discovered that Fe-MOF-74 can be used to separate paraffin/olefin mixtures[103] by using breakthrough experiments. An equimolar propane/propylene mixture was flowed in to a column packed with Fe-MOF-74 with a constant flow rate. The outlet gas was analysed with gas chromatography and 100% pure propane was initially collected, indicating that the propylene had been retained by the MOF. Once the MOF reached saturation, the propylene broke through and was detected by gas chromatography. To collect the propylene that was bound to the open iron sites of the MOF, a flow of pure nitrogen was passed through the column. They also developed a method to simulate breakthrough curves from single gas adsorption isotherm data and found that the simulated curves matched very well with the experimental breakthrough data. This method is now being used to assess separation capabilities for other gas mixtures and MOFs.[176]

In 2013, Long's group reported a MOF with one-dimensional triangular channels and its application in the enrichment of branched hexanes from hexane mixtures to produce petroleum with a higher research octane number (RON).[177] When a hexane mixture is flowed through a column packed with this MOF, *n*-hexane is strongly adsorbed in the pores while the branched hexane can easily pass through. This process can produce hexane mixtures with RON greater than 92. Conversely, current technology uses a zeolite-sieving process can produce a final RON of nearly 83 and requires subsequent distillation.

In steel manufacturing, exhaust CO is mixed with N_2 and burned to produce CO_2. Separating CO from N_2 can eliminate this energy waste and reduce CO_2 emissions. It is challenging to separate these gases using zeolite-based adsorbents due to their size similarity. The current technology for CO separation employs an energy-intensive chemical adsorption method.[178] To improve this process, Kitagawa's group discovered a flexible MOF, which can adsorb weakly coordinated CO. The binding of CO is cooperative in that the initial binding event triggers a global structural change which promotes the adsorption of more CO.[179] This material is effective in enriching CO from CO/N_2 mixtures.

1.3.2 Highlights of other applications

1.3.2.1 Crystalline sponge

In 2013, Fujita's group reported a zinc based MOF which is capable of adsorbing a range of guest molecules and aligning them with periodic order. This enables the structural determination of these guests by X-ray crystallography.[180] These crystalline sponges thus have transformative potential for determining the structures of natural products and pharmaceuticals since these compounds do not need to be themselves crystallized for the diffraction experiments. This method is applicable to: 1) Substrates which are liquids at room temperature. 2) Samples on a sub-microgram scale. 3) Enantiopure compounds for absolute structure determination. 4) Analytes collected as fractions from HPLC as a prototype HPLC-SCXRD analytical method. It is estimated that 20-30% of organic compounds can be crystallized in this crystalline sponge.

In the original paper, the authors also completely determined the stereochemistry of all three chiral centres of a scarce natural product, Miyakosyne A. However, in a later announcement these authors declared that the determination of these chiral centres might be incorrect. Fujita's group subsequently published an article in *Nature Protocols* with detailed step-by-step procedures for this method.[181]

MOFs that can be used as crystalline sponges are very rare. There are two key features of this Fujita's MOF. First, its ligand has an electron-deficient core, which is the basis of the strong host-guest interactions. Second, the MOF itself crystallizes in a low symmetry space group C2/c, which means the guests can be taken up without crystallographic disorder.

1.3.2.2 Toxic gas adsorption and destruction

Back in 2011, Navarro's group reported on toxic warfare gas removal using MOFs as adsorbents.[182,183] More recently, three striking papers have been published on the rapid hydrolysis of toxic gases and their analogues.[184-186] In these studies, UiO-66 functionalized with LiO^{t}Bu,[9] NU-1000[187] and MOF-808[188] were used. Hupp's group found that Zr_6 clusters with low ligand connectivity exhibit fast catalytic turnover due to their high concentrations of Lewis acid sites.[185,186] Navarro's group found that LiO^{t}Bu functionalized UiO-66 can accelerate the hydrolysis of warfare gases despite its highest connectivity (12-connected).[184] They also integrated this UiO-66@LiO^{t}BU with a textile and found this composite is also highly active.

1.4 Introduction to selected experimental and computational techniques

1.4.1 Gas adsorption

1.4.1.1 Essentials of the adsorption process

To better understand how a MOF adsorbs, stores, sieves and separates gases, some basics of the adsorption process are introduced below.

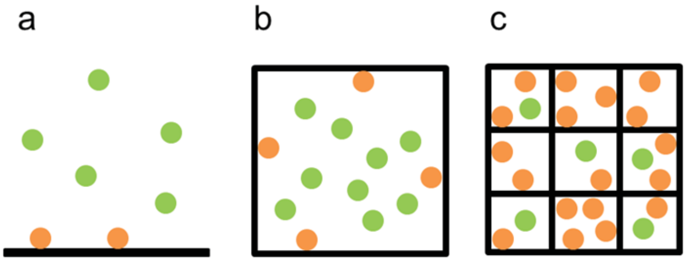

Figure 1.19 A schematic representation of a) gas molecules in contact with a surface. Green circles represent molecules in the gaseous phase and orange circles represent adsorbed gas molecules, b) gas molecules in a container showing some of them are adsorbed on the surface, c) an illustrative view of a container with a higher surface area for adsorbing gas molecules.

Figure 1.19a illustrates the adsorption of gas molecules on a surface. Green circles represent bulk gas molecules while orange circles represent adsorbed molecules. For physisorption, where the interaction between the gas molecules and the surface is reversible, adsorption is attributed to the noncovalent interactions between gas molecules and the surface. Figures 1.19b and c highlight how an increased surface area in a given volume of space will increase the fraction of molecules that are adsorbed to the surface and thus reduce the pressure.

An adsorption isotherm plots the amount of gas adsorbed on the surface as a function of the pressure at a constant temperature. Several theoretical models have been developed to describe adsorption isotherms, such as Henry, Langmuir, Brunauer-Emmett-Teller (BET),[19] and others.[189]

1.4.1.2 BET surface area calculations

The BET model is the most widely accepted by the porous materials community to calculate a material's apparent surface area. Experiments are usually carried out by measuring a nitrogen isotherm at 77 K (Figure 1.20a as an example). It was found in the past that often the entire isotherm doesn't fit well with the model (Figure 1.20c is derived from experimental data and supposed to be linear according to the BET equation). In order to obtain a reportable value, researchers have chosen a region of the isotherms which appear to be linear when the BET equation is applied. The choice is often arbitrary and can cause large deviations in surface area depending on the pressure region selected.[137] To regulate this chaos, Walton and Snurr proposed a procedure for deciding on appropriate pressure ranges for calculating BET surface areas,[190] which were followed in this thesis:

1) The isotherm region where $v(1-P/P_0)$ increases versus P/P_0, where v is the amount of N_2 adsorbed, was identified. Here, P/P_0 is the relative pressure, P being the pressure at for the adsorbent in equilibrium with the porous material at each point of measurement and P_0 is the condensation pressure of the adsorbent at the temperature of measurement.

2) Within this isotherm region, sequential data points that led to a positive intercept in the plot of $\frac{P/P_0}{v(1-P/P_0)}$ against P/P_0, were found. This plot yields a slope a, and a positive intercept b. The number of gas molecules adsorbed in the initial monolayer is $v_m = \frac{1}{a+b}$.

3) The BET surface area was then calculated according to the following equation:

$$A_{BET} = v_m(cm^3g^{-1}) * \frac{1\ (mol)}{22400\ (cm^3)} * \sigma_0(\text{Å}^2) * N_A(mol^{-1}) * 10^{-20}(\frac{m^2}{\text{Å}^2})$$

Where N_A is Avogadro's constant, and σ_0 is the cross-sectional area of a N_2 molecule, which is 16.2 Å^2.

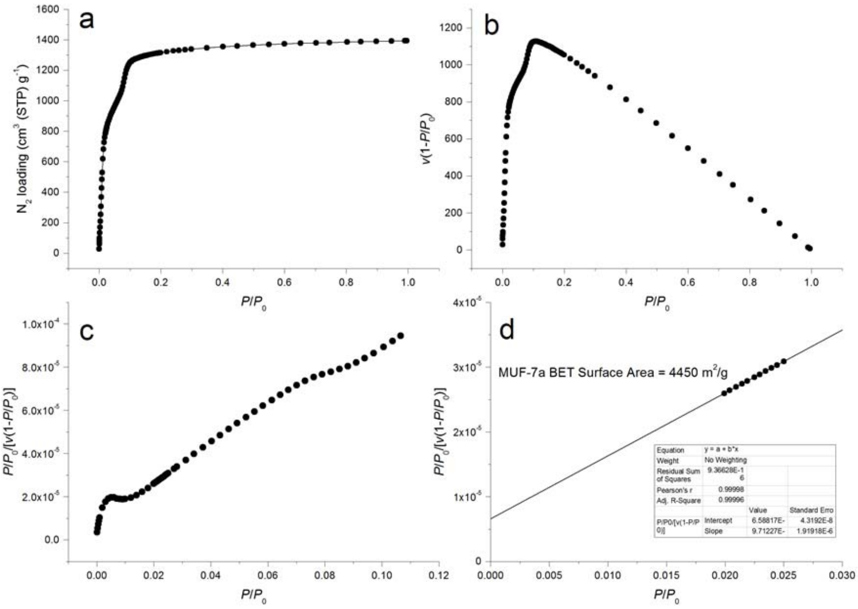

Equation	y = a + b*x		
Weight	No Weighting		
Residual Sum of Squares	9.36628E-16		
Pearson's r	0.99998		
Adj. R-Square	0.99996		
		Value	Standard Erro
P/P0/[v(1-P/P0)]	Intercept	6.58817E-	4.3192E-8
	Slope	9.71227E-	1.91918E-6

Figure 1.20 a) An example N_2 adsorption isotherm measured at 77K for MUF-7a.[191,192] b) A plot to find the pressure region that meets the first consistency criterion for BET surface area calculation according to the method proposed by Walton and Snurr.[190] c) A plot to find the pressure region that meets the second consistency criterion. d) BET plot.

1.4.1.3 Pore volume calculations

When adsorption reaches saturation, the isotherm plateaus. At this point, the total pore volume of the material can be calculated by assuming that the adsorbed gas is in a condensed liquid-like phase. Because the amount of adsorbed gas is known, its corresponding volume is simply calculated based on the density of the liquid adsorbate. The total mass of the adsorbing material is always precisely measured prior to an isotherm measurement.

1.4.1.4 Isosteric heat of adsorption calculations

Heats of adsorption (Q_{st}) are quantitative enthalpic measures of the affinity of a porous material for a given guest molecule. These values are calculated according to the method described in the literature.[193] Briefly, two isotherms that are measured at two different temperatures are first fit to a virial equation:

$$\ln \boldsymbol{P} = \ln \boldsymbol{N} + \frac{\mathbf{1}}{\boldsymbol{T}}\sum_{i=0}^{m} \boldsymbol{a_i N^i} + \sum_{i=0}^{n} \boldsymbol{b_i N^i}$$

where N is the amount of gas adsorbed at the pressure P.

Then, to calculate Qst, the fitting parameters from the virial equation are used in the following equation:

$$\boldsymbol{Q_{st}} = -\boldsymbol{R}\sum_{i=0}^{m} \boldsymbol{a_i N^i}$$

where R is the universal gas constant.

1.4.1.5 Introduction to a gas adsorption analyser

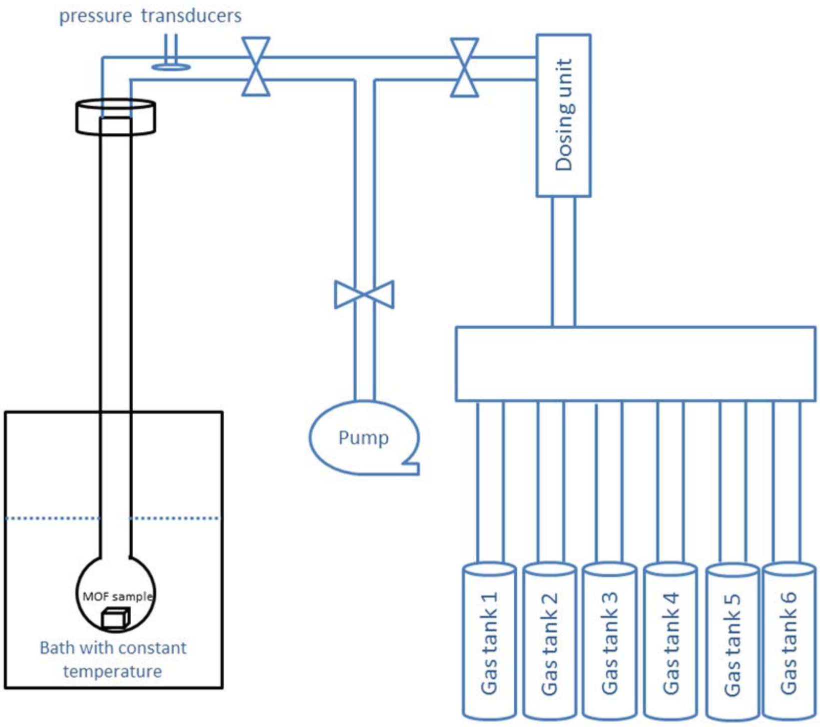

Figure 1.21 A cartoon showing the essential components of a gas adsorption analyser.

Figure 1.21 illustrates the key components of a gas adsorption analyser. A sample tube containing MOF crystals is evacuated and immersed in to a bath with a constant temperature. The instrument then doses a known amount of gas into the sample tube and reads the pressure frequently. The equilibration of adsorbed and non-adsorbed gas is known to be reached when the pressure reaches a constant value. The amount of gas adsorbed in the MOF sample can be calculated by taking the difference of pressure expected from the real gas law and the equilibrated pressure. This process is repeated so a plot of amount adsorbed versus equilibration pressure is obtained as an adsorption isotherm.

1.4.1.6 Reliability of measurements and calculations

The reliability of gas adsorption measurements were tested on a MOF sample prepared in our lab using our Quantachrome Autosorb iQ2 instrument. The average total N_2 uptake saturation at 77 K of this sample was 991.4 cm^3/g (STP) with a standard deviation of 1.2 cm^3/g (STP) based on four independent measurements. Because the standard error is only 0.12 % of the mean value, the error bar is much smaller than the symbol size on a typical gad adsorption isotherm plot (Figure 1.20a). For this reason, standard deviation, or other error or uncertainty estimates, are thus not conventionally reported for adsorption isotherms. When the amount of gas adsorbed in a MOF sample is very low, the instrument can struggle to produce accurate measurements. When this happens, an isotherm curve is usually not smooth, indicating the background noise is significant.

Sample preparation and activation can significantly impact gas adsorption measurements. BET surface areas and pore volumes calculated from a N_2 adsorption isotherm measured at 77 K can be used to compare with the theoretical values[194,195] of a MOF. This comparison can provide an idea of how well a given MOF sample was prepared and activated and whether regions that are closed off to guest molecules are present.

When calculating BET surface areas, the choice of the pressure region is still somewhat arbitrary even when strictly following the consistency criteria mentioned earlier. The choice of pressure range can have a pronounced impact on the surface area.[137]

Once the pressure region for the BET equation has been decided, linear regression using a least squares method produces standard deviations for the slope and intercept, which provide a good estimate of the uncertainty in the BET surface area (Figure 1.20d). In the example described in section 1.4.1.2, the standard deviation in the BET surface area is 8 m^2/g. Therefore, in this thesis, all BET surface area values are rounded to the nearest 10 m^2/g.

1.4.2 Grand Canonical Monte Carlo (GCMC) simulations

Gas adsorption in MOFs can be simulated by calculating the amount of gas adsorbed by a porous material as a function of pressure at a given temperature.[196] Because the number of molecules in a system can be quite large, it is impractical to employ quantum mechanical calculations. Less computationally-intensive force-field based simulations are generally used. In force-field based simulations, the Lennard-Jones interactions are used to describe the potential between two atoms (framework plus guest and guest plus guest):

$$V_{LJ} = 4\varepsilon\left[\left(\frac{\sigma}{r}\right)^{12} - \left(\frac{\sigma}{r}\right)^{6}\right] = \varepsilon\left[\left(\frac{r_m}{r}\right)^{12} - 2\left(\frac{r_m}{r}\right)^{6}\right]$$

where V_{LJ} is the Lennard-Jones potential, ε is the depth of the potential well, σ is the distance of two atoms when their potential is zero, r is the distance of two atoms, r_m is the distance of two atoms where their Lennard-Jones potential is minimum (Figure 1.22). In addition to the Lennard-Jones potential, charge interactions between atoms are also calculated to mimic interactions between framework atoms and polar molecules.

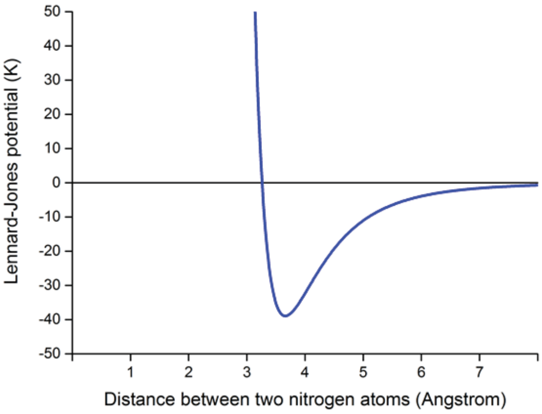

Figure 1.22 Lennard-Jones potential plot of nitrogen with its parameters taken from DREIDING force field.

In a typical simulation, each gas molecule is randomly inserted to the internal void of a MOF and the total Lennard-Jones potentials are calculated. If this random insertion Monte Carlo (MC) move is energetically favourable, then it is accepted and contributes to the ensemble. Other MC moves used in simulations are rotation of a gas molecule, deletion-reinsertion, and swapping gas identities. All simulations in this thesis were conducted using the RASPA code with the permission from the authors.[197]

Chapter 2

The First Quaternary Zinc-Carboxylate Metal-Organic Framework

2.1 Introduction

Since ternary multicomponent MOFs (MC-MOFs) that are constructed with two distinct organic ligands are well established, we wondered whether it would be possible to introduce a third organic ligand and thus synthesize some quaternary MC-MOFs. Another ligand would add a new dimension of complexity and functionality to the frameworks and could potentially open up a whole new area of exciting chemistry. This potential was identified by Yaghi's group in a review article published in *Science* in 2013.[57] They proposed that the 'materials beyond' will feature *multiple kinds of building units* (ligands) that are arranged within crystals with *specific sequences*. Although it is clear that MC-MOFs will be ideal candidates to explore this exciting chemistry, synthesizing MC-MOFs using *as few as three or four* distinct ligands remained *an outstanding challenge* at that time, *because such chemistry* was *believed to give mixed phases rather than a single phase comprising mixed components*.

One stern challenge that is encountered in the synthesis of quaternary (and higher order) MOFs is finding sets of linkers that are mutually compatible for inclusion in a lattice. Although clear design rules have not yet emerged, it is likely that the relative metrics (length and topology) of the ligands are a key factor.[136,191] A second challenge is presented by the multitude of phases that compete for formation with the desired product.[55] For sets of organic linkers and only one type of metal node, using the simplifying assumption that each organic linker and linker pair only forms a single phase, the total number of theoretical possible competing phases, N, can be deduced by the following equation:

$$N = \sum_{i=1}^{n} \frac{n!}{i!\,(n-1)!} - 1$$

where n is the number of linkers in the set. Thus, there are six phases that compete with a quaternary MOF, which increases to 14 for a quinary MOF, and 1022 for a MOF comprising ten distinct linkers (Electronic Appendix B).

2.2 Results and discussion

Reacting three geometrically distinct ligands, H_3btb (btb = benzene-1,3,5-tribenzoate), H_2bpdc (bpdc = 4,4′-biphenyldicarboxylate) and H_2bdc (bdc = 1,4-benzenedicarboxylate) with $Zn(NO_3)_2$ in DEF (*N*,*N′*-diethylformamide) at 85 °C for 16 hours afforded colourless crystals with well-defined edges, as shown in the right hand side of Figure 2.1 (the green colour comes from the glass slide and was exaggerated by white balance settings of the camera). Single-crystal X-ray diffraction experiments showed that it belongs to the cubic space group *I*-43*d*. By solving the single crystal structure, we found the presence of all three ligands in this MOF. The three ligands in MUF-7a are aligned in a perfect order with precise locations (Figure 2.2). This was the first known quaternary MOF, which we termed Massey University Framework – 7a (MUF-7a). It has a formula $[Zn_4O(btb)_{4/3}(bpdc)_{1/2}(bdc)_{1/2}]$.

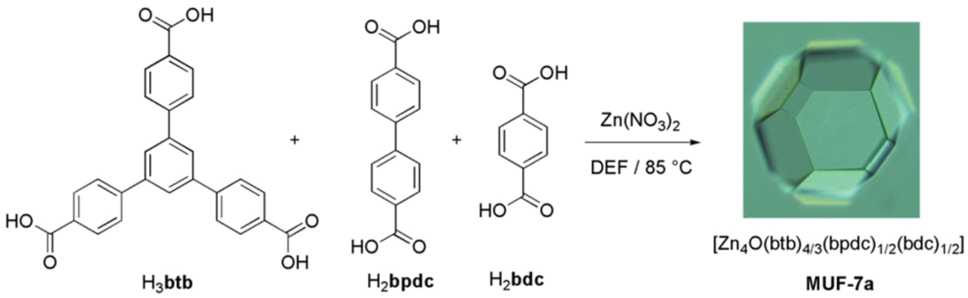

Figure 2.1 Synthetic route to MUF-7a with an optical microscopy image of a single crystal with a truncated rhombic dodecahedron geometry.

The three ligands, together with Zn_4O nodes, describe two types of cavities: i) dodecahedral cavities constructed with twelve Zn_4O nodes, eight btb linkers, three bpdc linkers, and three bdc linkers (Figure 2.3), and ii) pseudo-tetrahedral cavities which are delineated by four Zn_4O nodes, four btb linkers and two linear linkers. There are three subtypes of pseudo-tetrahedral cavities that differ by the identities of the two linear linkers that define them (Figure 2.4): a) two bpdc linkers, b) a bpdc / bdc linker pair and c) two bdc linkers.

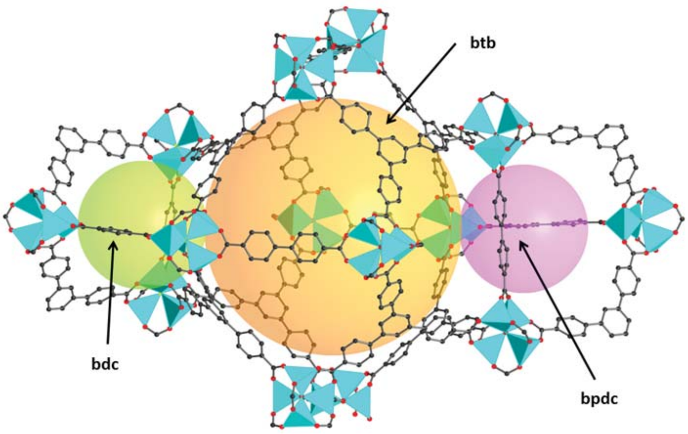

Figure 2.2 A view of the single crystal X-ray structure of MUF-7a showing the positions of three ligands: btb, bpdc, and bdc.

Table 2.1 Summary of x-ray crystallography data collection and refinement details of MUF-7a

MOF	**MUF-7a**
Formula	$C_{47}H_{26}O_{13}Zn_4$
Formula weight	1060.16
Crystal size (mm)	1.20×1.12×1.01
Temperature (K)	293(2)
Wavelength (Å)	1.54178
Crystal system	cubic
Space group	*I*-43*d*
Unit cell length (Å)	60.2324(11)
Unit cell volume ($Å^3$)	218520(12)
Z	48
D_{calc} (g cm^{-3})	0.387
μ (mm^{-1})	0.733
F(000)	25536
Reflns coll./unique, R_{int}	1694151/31006, 0.0601
Data range	6.6°< θ <65° or 6.7 Å > d > 0.85 Å
Index ranges	$-67 \le h \le 70$, $-70 \le k \le 70$, $-70 \le l \le 70$
Completeness	99.8%
T_{min}, T_{max}	0.47, 1.00
R indices for data with I>2 (I)	$R_1 = 0.0829$; $wR_2 = 0.2387$
R indices for all data	$R_1 = 0.0888$; $wR_2 = 0.2463$
Largest difference peak and hole (e $Å^{-3}$)	0.68 / −0.40

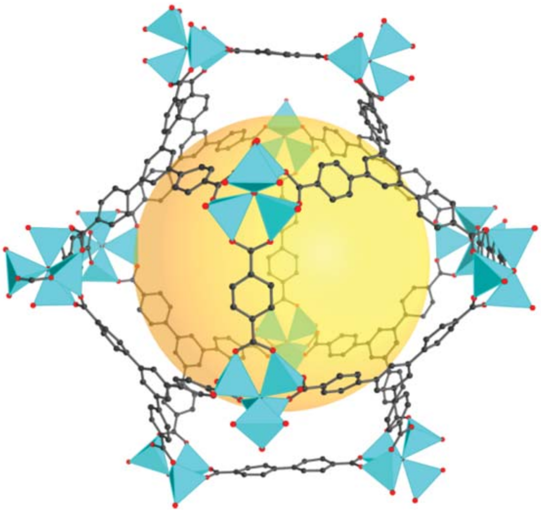

Figure 2.3 Single crystal X-ray structure of MUF-7a highlighting the dodecahedral cavity as an orange sphere.

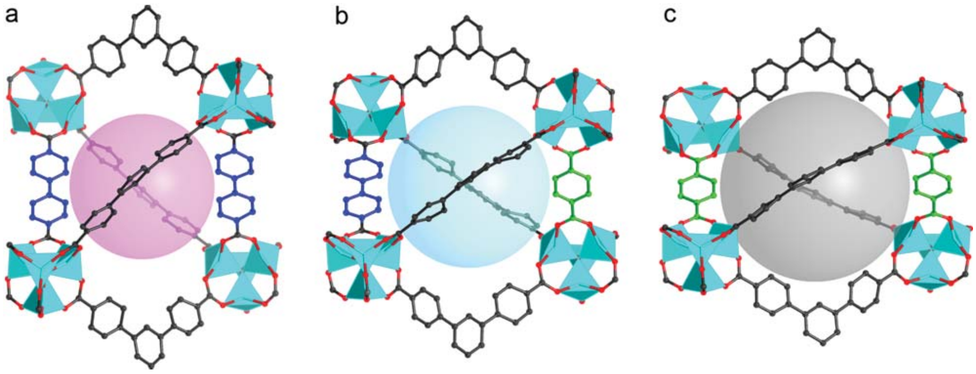

Figure 2.4 Single crystal X-ray structure of MUF-7a highlighting three kinds of pseudo-tetrahedral cavities delineated with four Zn_4O nodes, four btb linkers and (a) two bpdc linkers (pink), (b) a bpdc / bdc linker pair (blue) and (c) two bdc linkers (grey). Ligand colour code: btb: grey, bpdc: blue, bdc: green.

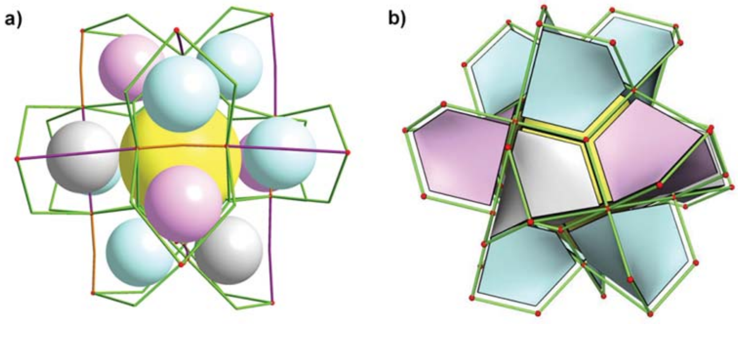

Figure 2.5 Representations of the crystal structure of MUF-7a showing (a) the relationship between the large dodecahedral cavity (yellow) and the three types of surrounding pseudo-tetrahedral cavities (blue, grey and pink). The three ligands are color-coded: green = btb; orange = bdc; purple = bpdc; and (b) A tiling image, produced using 3dt,[198] highlighting the central dodecahedral cavity in yellow and the three types of surrounding pseudo-tetrahedral cavities (blue, grey and pink).

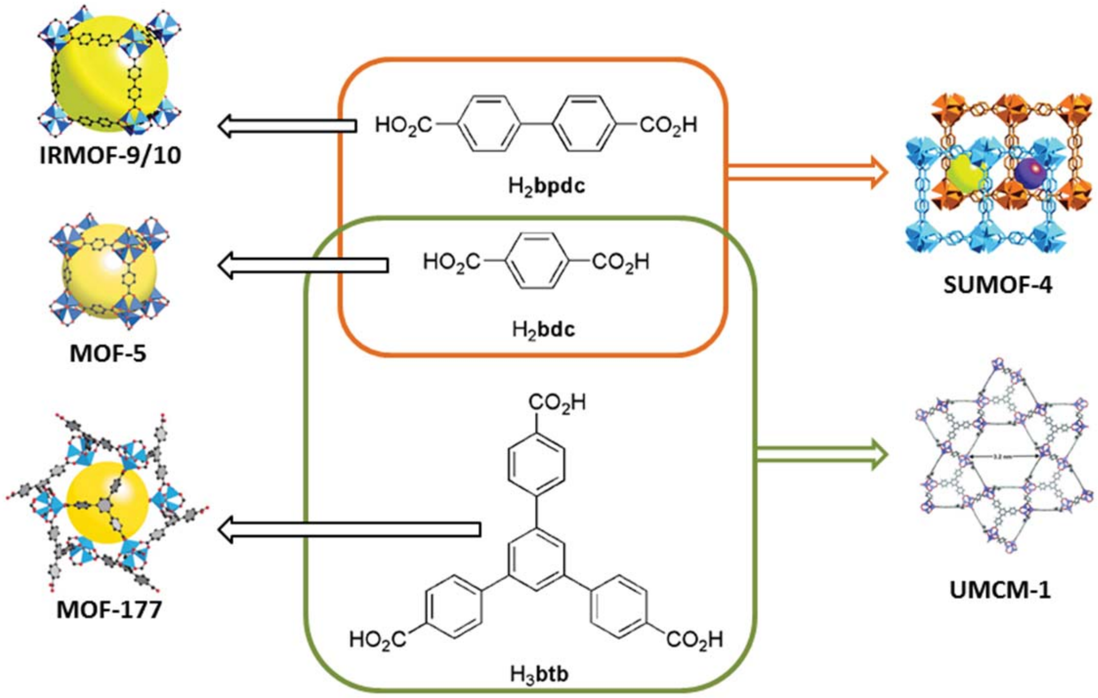

Figure 2.6 Competing phases that could form during the synthesis of MUF-7a. A Zn_4O MOF that is constructed with bpdc and btb is unknown.[136]

It was a great challenge to obtain MUF-7a in phase-pure form because each of the three organic linkers could form a MOF by itself (Figure 2.6). The btb ligand readily combines with Zn_4O clusters to produce MOF-177, $[Zn_4O(btb)_2]$,[12] which was found to be a persistent impurity in the first attempts at synthesizing MUF-7a. IRMOF-9, $[Zn_4O(bpdc)_3]$,[54] and MOF-5 $[Zn_4O(bdc)_3]$,[3] can also form from the linear linkers. Pairs of linkers can also combine to produce ternary MOFs: UMCM-1 $[Zn_4O(btb)_{4/3}(bdc)]$[55] and SUMOF-4 $[Zn_4O(bpdc)(bdc)_2]$.[138] A MOF containing btb and bpdc together with Zn_4O clusters is not known, presumably because of the size mismatch between these ligands. Post-synthetic purification methods that usually work for small molecule chemistry would not work in this case because the reaction products are not soluble. We thus sought to adjust the synthetic conditions so that only MUF-7a forms during the synthesis.

When the stoichiometry of the three linkers in MUF-7a was used as the feed ratio (btb: bpdc: bdc = 8: 3: 3), the major product was MOF-177. This is because all carboxylate groups are equally reactive.[55] Thus the probability of H_3btb reacting with zinc is 1.5 times higher than H_2bpdc or H_2bdc. To prevent the formation of MOF-177, the amounts of

H_2bpdc and H_2bdc in the reaction mixture were gradually increased (btb: bpdc: bdc = 3: 4: 4). This suppressed the formation of MOF-177, though led to the formation of UMCM-1 as a major side product. To eliminate UMCM-1, we increased the concentration of H_2bpdc and dropped H_2bdc (btb: bpdc: bdc = 3: 5: 3). After a reaction time of 24 hours, MUF-7a was the major product with IRMOF-9 as a minor impurity. It was then found that the IRMOF-9 phase only starts to form when the reaction was left for longer than 18 hours. To achieve the highest yield without any impurities, a reaction time of 16 hours was found to be optimal.

To confirm the phase purity of MUF-7a, we conducted a range of experiments. First, optical microscopy images (Figure 2.7) showed only one type of crystal and no other solid material is present after synthesis. Under crossed polarizers on an optical microscope, all of the crystals remained permanently extinguished, regardless of their rotational position, indicating they all belong to a cubic crystal system. To eliminate the possibility that other MOFs with cubic systems, such as MOF-5 or IRMOF-10 were present, we measured the powder X-ray diffraction pattern of the bulk sample and found it agrees very well with the simulated pattern predicted from its single-crystal structure (Figure 2.8). Thus, the presence of any other phases is eliminated. To check whether there are any unreacted ligands trapped in the MOF pores, we digested as-synthesized MUF-7a crystals in a solution of DCl / DMSO-d_6, and measured its ^{1}H NMR spectra (Figure 2.9). The integral ratio between the three ligands is in perfect agreement with the stoichiometry of MUF-7a, indicating no unreacted ligands are trapped inside the MOF. In addition, we did elemental analysis and the result was in good agreement with theory.

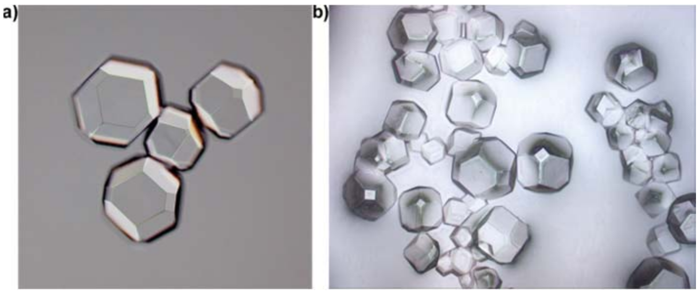

Figure 2.7 Microscopy images of MUF-7a showing its phase purity. a) A cluster of four MUF-7a crystals. b) A stacked image with multiple images that were taken with different focal planes.

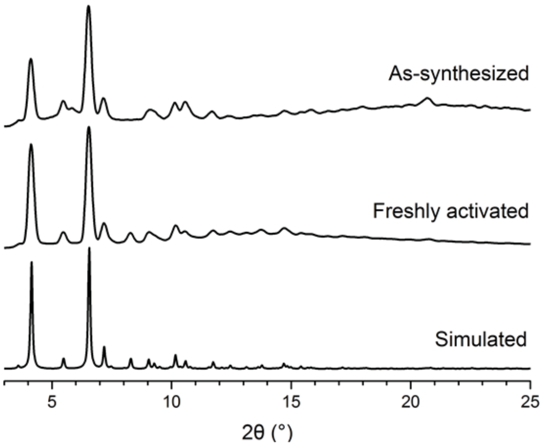

Figure 2.8 Powder XRD patterns of as-synthesized, freshly activated (by heating crystals exchanged with CH_2Cl_2 under vacuum) bulk samples, and the pattern of MUF-7a simulated from its single crystal structure.

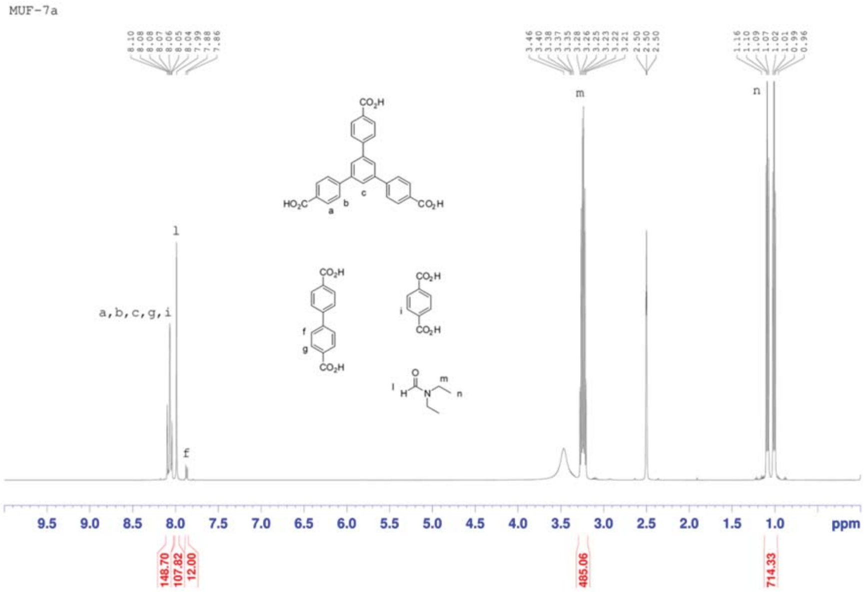

Figure 2.9 ^{1}H NMR spectra of digested MUF-7a with occluded DEF solvent molecules showing the integrals that match with the formula $[Zn_4O(btb)_{4/3}(bpdc)_{1/2}(bdc)_{1/2}]$.

The ^{1}H NMR spectrum of digested MUF-7a showed the presence of significant amount of DEF solvent molecules (20 DEF molecules per formula). This finding indicates that MUF-7a is highly porous and could potentially show permanent porosity after removal of these DEF molecules. To confirm this hypothesis, we decided to do some gas adsorption experiments.

MUF-7a was first activated to remove the solvent occluded in its pores during synthesis. To accomplish this, as-synthesized crystals of MUF-7a were soaked in fresh anhydrous DMF and the solvent was replenished several times over a period of three days. The crystals were then soaked in CH_2Cl_2 for three days, replacing the CH_2Cl_2 every day. The CH_2Cl_2-solvated crystals were then transferred to a pre-weighed gas adsorption sample tube and were desolvated by heating under dynamic vacuum with a rate of 1 °C/minute to 80 °C and held for 10 hours. Gas adsorption measurements were then conducted.

Gas adsorption experiments were conducted at CSIRO on a Micromeritics ASAP 2040 instrument. First, a nitrogen adsorption isotherm was measured at 77 K. As shown in Figure 2.10a, MUF-7a takes up 1251 cm^3 (STP)/g nitrogen at 77 K at saturated loading ($P/P_0 = 0.995$). P/P_0 is a partial pressure defined by the ratio of the actual pressure and the condensation pressure of the adsorbate gas at the measurement temperature. A two-step steep rise of the uptake below $P/P_0 = 0.1$ is characteristic of materials that have both micropores (pore diameter < 2 nm[199]) and mesopores (2 nm ≤ pore diameter ≤ 50 n). This two-step event is thus in good agreement with the single crystal x-ray structure of MUF-7a, which showed the pores in these size ranges exist. The BET surface area of MUF-7a was calculated to be 4050 m^2/g. We later found that MUF-7a prepared in DMF instead of DEF can be better activated and takes up more N_2 (1394 cm^3/g, STP). The corresponding BET surface area is 4450 m^2/g. This value is very close to the calculated[194] geometric surface area (4483 m^2/g). The pore volume calculated from the N_2 isotherm of MUF-7a prepared in DMF is 2.16 cm^3/g, which compares well with the calculated[195] pore volume of 2.31 cm^3/g.

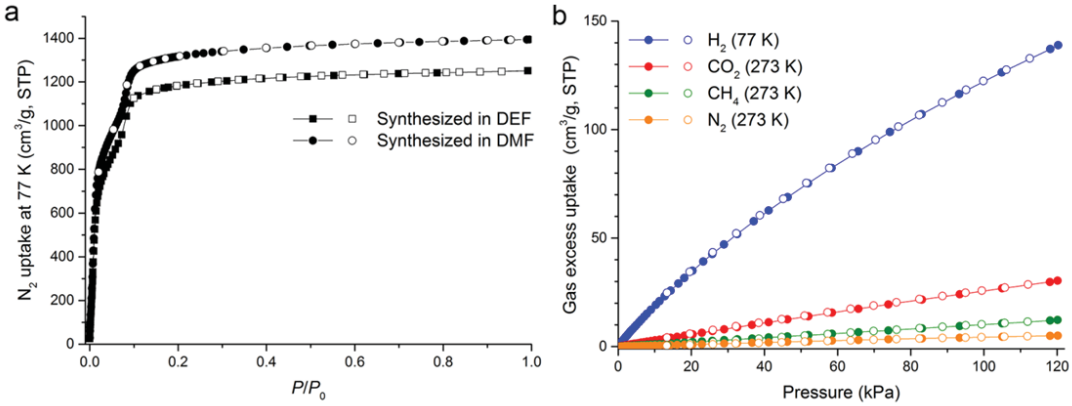

Figure 2.10 a) Nitrogen adsorption (filled symbols) and desorption (open symbols) isotherm measured at 77 K. Material synthesized in DMF takes up higher amount of N_2. b) Gas adsorption (filled circles) and desorption (open circles) isotherms of MUF-7a measured at 77 K (H_2: blue) and 273 K (CO_2: red, CH_4: green, and N_2: orange).

Gas adsorption isotherms were also measured for a range of other gases. MUF-7a adsorbs a moderate amount of CO_2 at 273 K and 120 kPa (30.4 cm^3/g, Figure 2.10b). Due to the strong noncovalent interactions between polar CO_2 molecules and porous hosts, as expected this is higher than N_2 (5.0 cm^3/g) and CH_4 (12.3 cm^3/g). Such selective adsorption of gases is characteristic of MOFs and enables potential applications such as flue gas treatment, landfill gas separation and natural gas purification.[200]

MUF-7a also adsorbs a considerable amount of hydrogen at 77 K. To compare with other known MOFs, the amount of adsorbed hydrogen is best expressed in units of mass of hydrogen per mass of framework. MUF-7a takes up 12.4 mg/g hydrogen at 77 K and 120 kPa (Figure 2.10b), which is comparable to MOF-5 (13.2 mg/g at 77 K and 101 kPa) and MOF-177 (12.5 mg/g at 77 K and 101 kPa).[201] An uptake value for 12.4 mg/g converts to a total volumetric uptake of 5.13 mg/cm^3 by taking the bulk mass of H_2 into consideration. It is worth noting that the bulk mass of H_2 under the same conditions but without an adsorbent is only 0.37 mg/cm^3 (Figure 2.11a). By introducing MUF-7a as an adsorbent, the volumetric storage capacity of H_2 is increased nearly 13 fold compared to an empty vessel at ambient pressure and cryogenic temperature. This illustrates the promise of MOFs as fuel tank filler materials for hydrogen powered vehicles.

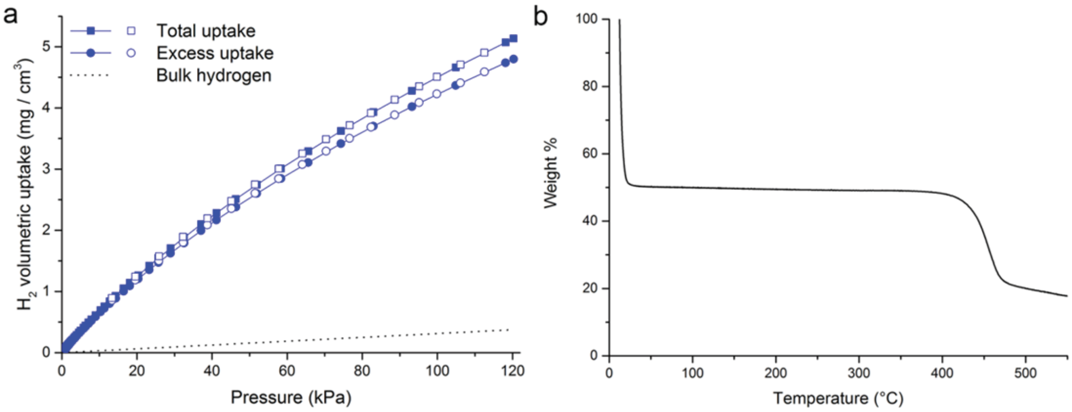

Figure 2.11 a) Volumetric H_2 excess (circles) and total (squares) uptake at 77 K for MUF-7a compared with the bulk hydrogen (black dotted line). b) Thermogravimetric analysis (TGA) trace of CH_2Cl_2-solvated MUF-7a.

In addition to its high porosity and ability to take up gases, MUF-7a also displays excellent thermal stability. Thermogravimetric analysis (TGA) of CH_2Cl_2-solvated MUF-7a crystals shows a mass loss of 50%, when the sample was heated to 30 °C due to escape of the solvent. The remaining desolvated framework is stable up to 400 °C before the onset of thermal decomposition is observed (Figure 2.11b).

2.3 Conclusion

In conclusion, the first quaternary MC-MOF, MUF-7a, has been discovered. This was achieved by copolymerizing btb, bpdc, bdc and Zn_4O metal nodes. Through careful adjustment of reaction time and the feed ratio of the organic components, phase pure material was obtained. The single crystal X-ray structure of MUF-7a shows the three organic linkers are aligned in specific location in the framework lattice. The crystal structure of MUF-7a exhibits a range of pore types, and this void space can be accessed by guest molecules following framework activation. This cavity makes MUF-7a an ideal platform to explore more sophisticated chemistry involving linkers with functional groups, as presented in the next chapter.

2.4 Experimental section

2.4.1 General procedures

All starting compounds and solvents were used as received from commercial sources without further purification unless otherwise noted. H_3btb[202] was prepared via a literature procedure. Column chromatography was carried out on silica gel (grade 60, mesh size 230-400, Scharlau). NMR spectra were recorded at room temperature on Bruker-400 and Bruker-500 Avance instruments, with the use of the solvent proton as an internal standard. IR spectra were collected on a Thermo Scientific Nicolet 5700 FT-IR spectrophotometer equipped with an attenuated total reflection (ATR) module (Smart Omni sampler, Ge crystal). Spectra were measured at a resolution of 4 cm^{-1}. Elemental analyses were performed by the Campbell Microanalytical Laboratory at the University of Otago, New Zealand. Care was taken to limit the exposure of all MOFs to the atmosphere.

2.4.2 MOF synthesis and characterization

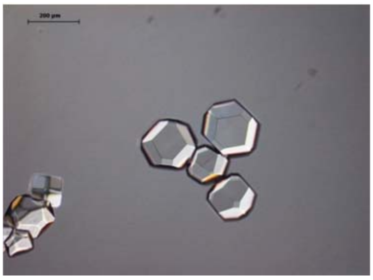

1,3,5,-Tris(4-carboxyphenyl)benzene (13.2 mg, 0.030 mmol), 4,4′-biphenyldicarboxylic acid (12.1 mg, 0.050 mmol) and benzene-1,4-dicarboxylic acid (5.0 mg, 0.030 mmol) were combined with $Zn(NO_3)_2\cdot 4H_2O$ (55.2 mg, 0.211 mmol) in dry DEF (4.0 mL) in a 20 mL vial and sonicated for 5 minutes before being heated in an 85 °C isothermal oven for 16 hours to obtain colorless crystals of MUF-7a. Yield: 37.4 mg. Anal.

calcd. for $[C_{47}H_{26}O_{13}Zn_4]\cdot 4H_2O$: C, 49.86; H, 3.03; Found: C, 49.73; H, 2.73. FT-IR: 1608 (s), 1586 (s), 1537 (s), 1260 (m), 1181 (w), 1104 (w), 1059 (m), 1016 (m), 854 (m), 808 (m), 779 (s), 749 (w), 704 (w). To scale up the synthesis, a parallel synthetic method was adopted (multiple vials using the scale described above).

DMF method: H_3btb (329 mg, 0.75 mmol), biphenyl-4,4′-dicarboxylic acid (365 mg, 1.5 mmol) and 1,4-benzenedicarboxylic (62 mg, 0.37 mmol) were combined with $Zn(NO_3)_2\cdot 4H_2O$ (1.388 g, 5.3 mmol) in dry DMF (100 mL) and water (1.5 mL) in a 500 mL Schott bottle which had been treated with Sigmacote and sonicated for 5 minutes before being heated in an 85 °C isothermal oven for 24 hours to obtain colorless crystals of MUF-7a.

2.4.3 ^{1}H NMR analysis of digested MOF samples

For ^{1}H NMR spectroscopy, the mother liquor of the as-synthesized MOF crystals was replaced with fresh dry DEF multiple times. The MOF crystals were then filtered through a sintered glass filter funnel under suction and the surfaces of the crystals were allowed to dry. The crystals were then digested using the following protocol: 23 μL of a 35% DCl solution in D_2O was mixed with 1 mL of DMSO-d_6 to give a DCl/DMSO-d_6 stock solution. Around 5 mg of MOF was digested in 150 μL of this stock solution together with 500 μL of DMSO-d_6. Spectra were acquired immediately following dissolution.

2.4.4 Thermogravimetric Analysis (TGA)

Thermogravimetric analyses were performed on a TA Instruments Q50 instrument. Freshly prepared MOF samples were washed with DMF then activated by soaking in CH_2Cl_2 for several days. Samples were then transferred to an aluminum sample pan, the solvent bound to the surface of the crystals was evaporated, and then measurements were commenced under an N_2 flow with a heating rate of 5 °C /min.

2.4.5 Single crystal X-ray diffraction

MOF crystals were mounted together with some dry DEF in a polymer sleeve on a Rigaku Spider diffractometer equipped with a MicroMax MM007 rotating anode generator (Cu_{α} radiation, 1.54180 Å), high-flux Osmic multilayer mirror optics, and a curved image-plate detector. Data were collected at 293 K and were integrated and scaled and averaged with FS Process.[203] XPREP[204] was used to determine the space group and the structures were solved using SHELXS[204] and refined with SHELXL.[204]

All atoms were found in the electron density difference map. Electron density difference maps were carefully analyzed for the possible presence of disordered framework components. All non-hydrogen atoms were refined anisotropically. Unrestrained atomic displacement parameters sometimes produced high U_{eq} values during the refinement thus ISOR, DELU and SIMU commands were introduced as appropriate with careful adjustments of the standard deviations. FLAT commands were introduced when necessary for some phenyl rings. Most of the bridging phenyl rings of the btb ligands were disordered. A free variable was used in each case to define the relative occupancies of the two sites.

2.4.6 Powder X-ray diffraction patterns

All powder X-ray diffraction experiments were carried out on a Rigaku Spider X-ray diffractometer with Cu K_α radiation (Rigaku MM007 microfocus rotating-anode generator), monochromated and focused with high-flux Osmic multilayer mirror optics, and a curved image plate detector. The data were obtained from freshly prepared MOF samples that had been ground into slurry in a small amount of DEF and kept damp with DEF throughout the measurement. The two-dimensional images of the Debye rings were integrated with AreaMax[205] to give 2θ vs I diffractograms. The predicted powder pattern of MUF-7a was generated from its single-crystal structure using Mercury v3.0.

2.4.7 Gas adsorption measurements

Low pressure adsorption isotherms were measured by a volumetric method using a Micromeritics ASAP 2420 instrument. Freshly prepared MOF samples were washed with DMF then activated by soaking in CH_2Cl_2 for several days, transfer to a pre-dried and weighed analysis tube contained in specially designed Schlenk glassware under a constant positive flow of argon atmosphere. Excess CH_2Cl_2 was removed under vacuum before the sample tube was stoppered with a Transeal cap, heated at 1 ºC per minute to 80 ºC under vacuum then held under a dynamic vacuum at 10^{-6} Torr for 24 h. Accurate sample masses were calculated using degassed samples. All adsorption measurements used ultra-high purity gases.

2.4.8 Computational details

The geometric surface area of MUF-7a was calculated to be 4181 m^2/g by the method described by Düren *et al*.[206] This involves rolling a spherical probe, with diameter was set to the van der Waals diameter of N_2 (3.72 Å),[207] over the framework atoms. The diameters of the framework atoms were also set to their van der Waals diameters which were calculated by multiplying their Lennard-Jones collision diameters, σ, by $2^{1/6}$. The σ values of all framework atoms were taken from the DREIDING force field.[208] The total pore volumes of these materials that are accessible to helium were calculated by a method detailed in the literature.[195]

Chapter 3

Programmable Pore Architectures in Quaternary Zinc-Carboxylate Metal-Organic Frameworks

3.1 Introduction

The three linkers in MUF-7a are positioned in predetermined locations in the lattice. If functional groups are appended to the three ligands, they too will be located in specific framework sites. These functional groups will point into certain pore regions of the MOF. If multiple functional groups are introduced to a particular pore, this creates a relatively complex pore environment. If the ligands are modular, then this pore environment can be rationally designed and tuned. This kind of chemistry is not known in the literature. The closest examples are MTV-MOFs and functionalized versions of UMCM-1,[34,42] both of which suffer a random or near-random distribution of functional groups and thus heterogeneous sets of pores.

Based on the results of Chapter 2, MUF-7a is an ideal platform to demonstrate the proof-of-principle of this concept. Figure 3.1 presents a conceptual illustration of the aims of this chapter. We planned to synthesize functionalized analogues of H_2bdc, H_2bpdc, and H_3btb, and introduce them into isoreticular variants of MUF-7a.

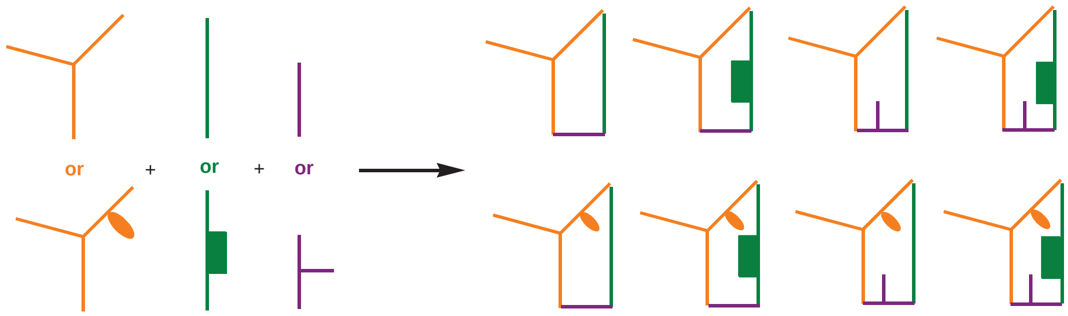

Figure 3.1 A schematic illustration showing how programmed pores can be generated by precisely organising ligands with appended functional groups.

3.2 Results and discussion

3.2.1 Designing functionalized ligands to circumvent crystallographic disorder

MOFs commonly crystalize in high symmetry space groups. This means that the atoms comprising a ligand are often crystallographically identical. For example, in both MOF-5[3] [Zn$_4$O(bdc)$_3$] and HKUST-1[7] [Cu$_2$(btc)$_{4/3}$], only two carbon atoms of the ligand's phenyl ring are in the asymmetric unit. This can create disorder when the linkers are functionalized in a way that is inconsistent with the crystallographic symmetry. A good example of this is replacement of the bdc linker of IRMOF-3, the MOF-5 analogue with 2-amino-1,4-benzenedicarboxylate. Because the space group of MOF-5 and IRMOF-3 is the same, the amino group is disordered over four sites.

With respect to MUF-7a, single-crystal X-ray diffraction reveals that there are three symmetry elements that can potentially generate disorder: twofold axes for the linear linkers and a threefold axis for one of the btb linkers (Figure 3.2). To combat disorder in functionalized variants of MUF-7a, functional groups should be introduced in a way that is compatible with these ligand site symmetries.

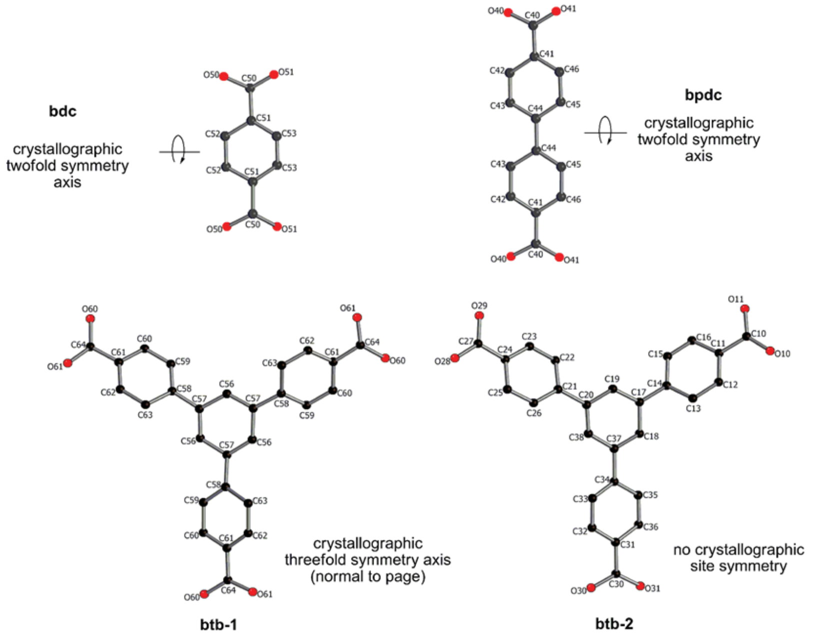

Figure 3.2 Crystallographic site symmetries of the bdc, bpdc and btb ligands in MUF-7a. Atoms with the same number are related by crystallographic symmetry operations.

Since bdc resides on a two-fold rotational axis parallel to its short axis (Figure 3.2), it should be functionalized with identical groups on its 2 and 3 positions or on its 2, 3, 5, and 6 positions to avoid disorder by symmetry. Co-planarity of the carboxyl groups and phenyl rings, which is probably important to maintain the overall lattice structure, is much more likely in the former case than the latter. This informed the choice of naphthalene-1,4-dicarboxylate (ndc, Figure 3.3) as an analogue of bdc. Similarly, the bpdc ligand also has a two-fold crystallographic symmetry axis that relates the two phenyl rings, so a 2,2′ or 2,2′,6,6′ substitution pattern will prevent disorder. In addition, ligands that can maintain perfect planarity will be geometrically disposed to adopting the fully planar conformation observed for bpdc in MUF-7a. The benzo[*c*]-cinnoline ligand (bcc) was chosen with these considerations in mind (Figure 3.3).

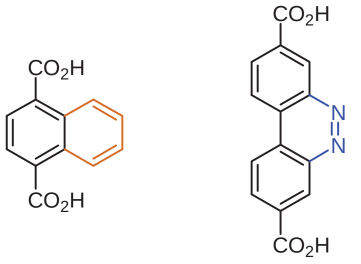

H_2ndc **H_2bcc**

Figure 3.3 Substituted bdc and bpdc ligands designed according to their crystallographic site symmetry elements to generate programmed-pore analogues of MUF-7a.

Two crystallographically independent btb ligands are present in MUF-7a. One of these has a three-fold rotational axis perpendicular to its central phenyl ring, while the other does not have crystallographically imposed symmetry (Figure 3.2). H_3**L1**, H_3**L2** and H_3**L3** were initially chosen or designed to be compatible with the three-fold rotational axis (Figure 3.4). However, **L1** was later found to be incompatible with the synthesis of MUF-7 and did not generate functionalized MUF-7 even when btb was used to dope the synthesis. This is probably due to its propensity to form a known zinc(II)-based MOF.[209]

Efforts to incorporate **L2** into a MUF-7a analogue were also unsuccessful. Instead, it produced a new MOF (detailed in the Electronic Appendix A). This MOF has large dihedral angles between the central and peripheral phenyl rings, and this phenomenon was also observed by others in a closely related ligand.[210] The bulkiness of methoxy groups on the central phenyl ring of **L2** forced the peripheral phenyl rings to be twisted (Figure 3.5 and Table 3.1, DFT: B3LYP/6-31G). This implies that the dihedral angle in the three-fold symmetrical ligand is a key factor in the propensity of MUF-7 type frameworks to form.

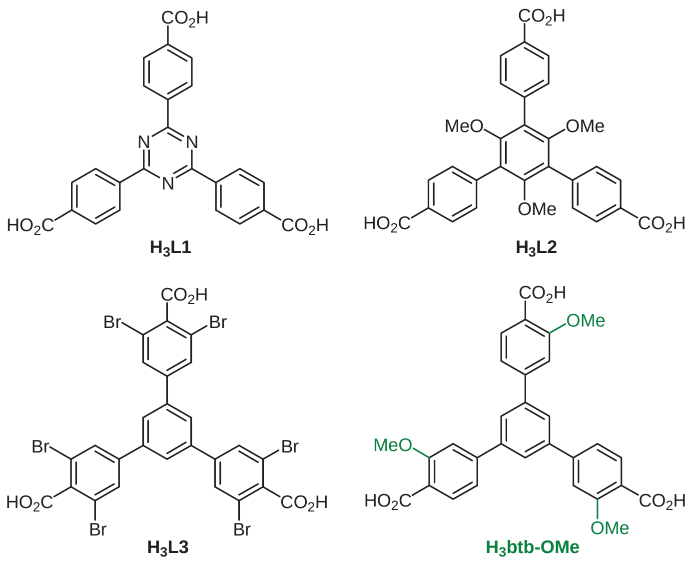

Figure 3.4 Substituted btb ligands designed to be compatible with the crystallographic site symmetry of btb in MUF-7a.

The synthesis of H_3**L3** was not successful, so we finally chose to use H_3btb-OMe[211] as the functionalized version of btb to generate variants of MUF-7a. Since its calculated dihedral angles between the central and peripheral phenyl rings are very similar to those of btb (Figure 3.5 and Table 3.1), btb-OMe is likely to be compatible with the synthesis of MUF-7a derivatives.

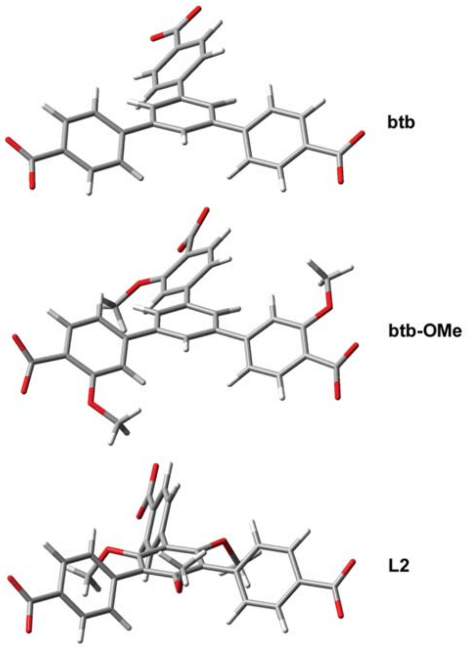

Figure 3.5 Calculated structures of btb^{3-}, btb-OMe^{3-} and **L2**$^{3-}$ showing the different dihedral angles of central-peripheral phenyl rings.

Table 3.1 Summary of geometry optimized structures of btb^{3-}, btb-OMe^{3-} and **L2**$^{3-}$

Ligand	Dihedral angles of central-peripheral phenyl rings (°)[a]		
btb^{3-}	35.4	35.4	35.6
btb-OMe^{3-}	34.4	34.6	35.2
L2^{3-}	51.8	53.7	69.6

[a] Ligand geometries were optimized using a DFT method (B3LYP/6-31G) implemented by the Gaussian 09**[212]** software package

3.2.2 Synthesis and X-ray crystal structures of programmed-pore MOFs (PP-MOFs)

As illustrated in Figure 3.6, there are eight possible combinations of bdc/ndc, bpdc/bcc, and btb/btb-OMe that can produce MUF-7a analogues. All seven new MOFs, named as MUF-7b-h, were successfully synthesized. Single crystal X-ray diffraction experiments revealed that they all adopt *I*-43d space group and have **ith-d** topology (Table 3.2). They are isoreticular to MUF-7a (Table 3.3).

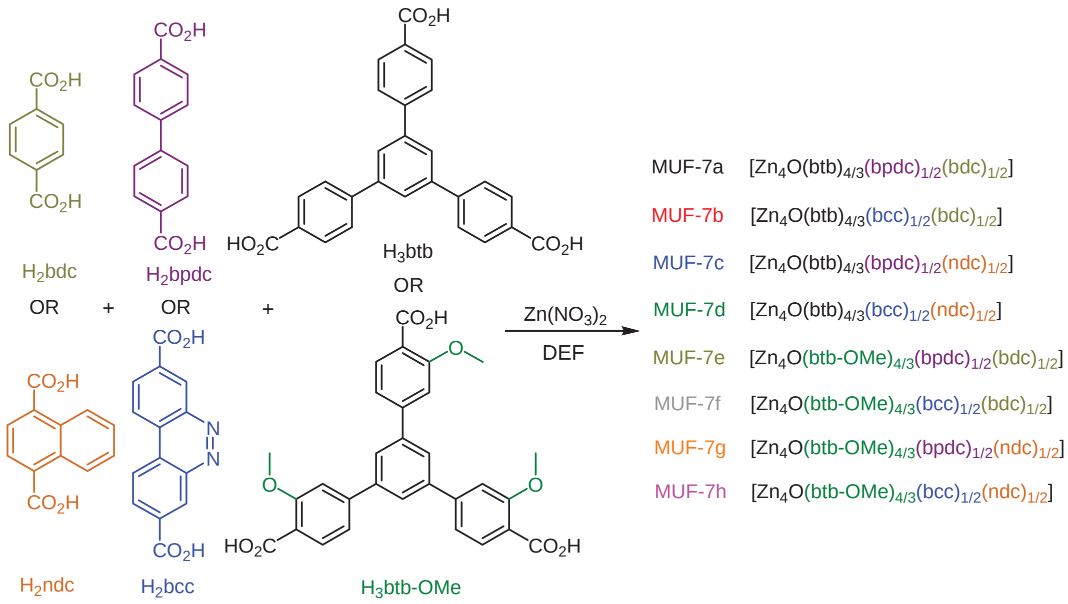

Figure 3.6 Synthetic routes to MUF-7a-h.

The synthetic routes to MUF-7b-h are broadly similar to that to MUF-7a. However, due to the subtle differences in the reactivity and solubility of the functionalized ligands, each reaction condition was carefully adjusted to obtain phase-pure materials in good yields. It is also found in some cases that direct synthesis failed to reliably produce phase-pure MOFs with high crystallinity. We solved this problem by developing a seeding technique that uses a small amount of crystal seeds to induce crystallization of the desired phase. Similar to MUF-7a, optical microscopy, powder XRD (Figure 3.7) and ^{1}H NMR spectroscopy were used and all these results indicate phase purity of MUF-7b-h.

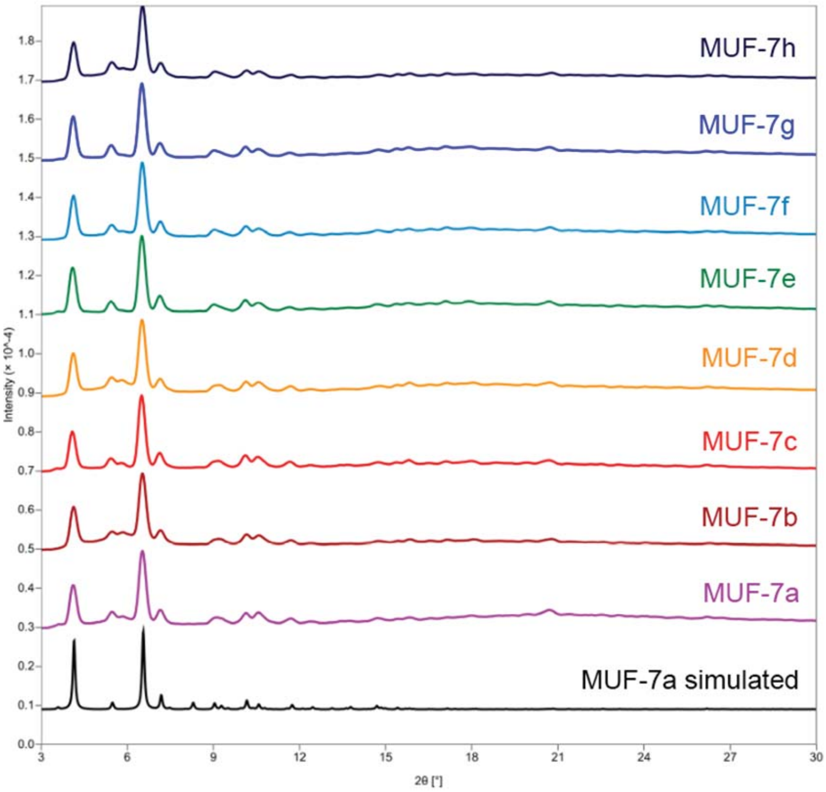

Figure 3.7 Simulated PXRD pattern of MUF-7a and experimental patterns of MUF-7a-h.

Table 3.2 X-ray crystallography: summary of data collection and refinement details for MUF-7b-h

MOF	**MUF-7b**	**MUF-7c**	**MUF-7d**	**MUF-7e**	**MUF-7f**	**MUF-7g**	**MUF-7h**
Formula	$C_{47}H_{25}NO_{13}Zn_4$	$C_{49}H_{27}O_{13}Zn_4$	$C_{49}H_{26}NO_{13}Zn_4$	$C_{51}H_{34}O_{17}Zn_4$	$C_{51}H_{33}NO_{17}Zn_4$	$C_{53}H_{35}O_{17}Zn_4$	$C_{53}H_{34}NO_{17}Zn_4$
Formula weight	1073.16	1085.18	1098.19	1180.26	1193.26	1205.29	1218.29
Crystal size (mm)	0.99×0.84×0.63	0.62×0.61×0.39	2.08×2.07×1.79	0.93×0.87×0.56	1.32×1.27×0.78	1.76×1.37×1.12	1.66×1.50×1.13
Temperature (K)	293(2)	293(2)	293(2)	293(2)	293(2)	293(2)	293(2)
Wavelength (Å)	1.54178	1.54178	1.54178	1.54178	1.54178	1.54178	1.54178
Crystal system	cubic	cubic	cubic	cubic	cubic	cubic	cubic
Space group	*I*-43*d*	*I*-43*d*	*I*-43*d*	*I*-43*d*	*I*-43*d*	*I*-43*d*	*I*-43*d*
Unit cell length (Å)	60.2289(7)	60.2326(6)	60.2136(6)	60.3052(11)	60.2594(6)	60.290(2)	60.2419(6)
Unit cell volume ($Å^3$)	218482(8)	218522(7)	218315(7)	219313(12)	218814(7)	219146(24)	218623(7)
Z	48	48	48	48	48	48	48
D_{calc} (g cm^{-3})	0.392	0.396	0.401	0.429	0.435	0.438	0.444
μ (mm^{-1})	0.737	0.737	0.741	0.765	0.770	0.769	0.775
F(000)	25824	26160	26448	28608	28896	29232	29520
Reflns coll./unique, R_{int}	241351/30774, 0.0413	303394/35419, 0.0430	182962/34683, 0.0417	332821/35614, 0.0710	206005/30770, 0.0318	207518/32777, 0.0370	252312/34736, 0.0453
Data range	$6.6° < \theta < 65°$ $6.7 > d > 0.85$ Å	$6.6° < \theta < 72°$ $6.7 > d > 0.81$ Å	$6.6° < \theta < 72°$ $6.7 > d > 0.81$ Å	$6.6° < \theta < 72°$ $6.7 > d > 0.81$ Å	$6.6° < \theta < 65°$ $6.7 > d > 0.85$ Å	$6.6° < \theta < 72°$ $6.7 > d > 0.81$ Å	$6.6° < \theta < 72°$ $6.7 > d > 0.81$ Å
Index ranges	$-41 \le h \le 70$, $-69 \le k \le 67$, $-41 \le l \le 54$	$-71 \le h \le 28$, $-53 \le k \le 55$, $-58 \le l \le 74$	$-40 \le h \le 64$, $-39 \le k \le 71$, $-73 \le l \le 17$	$-73 \le h \le 73$, $-69 \le k \le 69$, $-59 \le l \le 63$	$-70 \le h \le 42$, $-67 \le k \le 53$, $-32 \le l \le 58$	$-39 \le h \le 69$, $-34 \le k \le 57$, $-74 \le l \le 52$	$-70 \le h \le 36$, $-71 \le k \le 66$, $-65 \le l \le 41$
Completeness	99.5%	99.5%	99.4%	99.4%	99.6%	99.1%	97.9%
T_{min}, T_{max}	0.55, 1.00	0.62, 1.00	0.59, 1.00	0.43, 1.00	0.63, 1.00	0.67, 1.00	0.55, 1.00
R indices for data with $I > 2\sigma(I)$	$R_1 = 0.0885$; $wR_2 = 0.2526$	$R_1 = 0.0878$; $wR_2 = 0.2476$	$R_1 = 0.0833$; $wR_2 = 0.2365$	$R_1 = 0.1063$; $wR_2 = 0.3041$	$R_1 = 0.0897$; $wR_2 = 0.2541$	$R_1 = 0.0884$; $wR_2 = 0.2573$	$R_1 = 0.1053$; $wR_2 = 0.3133$
R indices for all data	$R_1 = 0.1148$; $wR_2 = 0.2854$	$R_1 = 0.1273$; $wR_2 = 0.2819$	$R_1 = 0.1194$; $wR_2 = 0.2825$	$R_1 = 0.1404$; $wR_2 = 0.3269$	$R_1 = 0.1160$; $wR_2 = 0.2939$	$R_1 = 0.1190$; $wR_2 = 0.2939$	$R_1 = 0.1243$; $wR_2 = 0.3240$
Largest difference peak and hole (e $Å^{-3}$)	0.72 / −0.55	0.76 / −0.39	0.70 / −0.52	0.89 / −0.37	1.07 / −0.64	0.86 / −0.43	1.02 / −0.51

Single crystal XRD experiments showed that, as hoped for, the ligands of MUF-7a are simply replaced by their functionalized counterparts in the lattice of MUF-7b-h (Figure 3.8). Since their space group and unit cell parameters remain unchanged (Table 3.3), the crystallographic site symmetries of the ligands are also retained.

It is also possible for the ligands to suffer from positional disorder. For example, the pyridazine ring of the bcc ligand can be positioned on either side of the carboxyl-carboxyl axis of the ligand. To determine whether positional disorder exists in these MOFs, we carefully analysed the observed electron density maps generated from their single crystal XRD data (Figure 3.9 and Electronic appendix A). No disorder of this kind was found: all functional groups were located on these maps exclusively on one side of the carboxyl-carboxyl axis (bcc and ndc) or of the centroid-carboxyl axes (btb-OMe). The important conclusion from this analysis is that the functional groups of each ligand occupy specific positions in the lattice.

Table 3.3 Summary of the key properties of MUF-7a and its programmed-pore analogues, MUF-7b-h

	MUF-7a	**MUF-7b**	**MUF-7c**	**MUF-7d**	**MUF-7e**	**MUF-7f**	**MUF-7g**	**MUF-7h**
linker set	btb bpdc bdc	btb bcc bdc	btb bpdc ndc	btb bcc ndc	btb-OMe bpdc bdc	btb-OMe bcc bdc	btb-OMe bpdc ndc	btb-OMe bcc ndc
unit cell length[a]	60.2324 (11)	60.2289 (7)	60.2326 (6)	60.2136 (6)	60.3052 (11)	60.2594 (6)	60.2920 (2)	60.2419 (6)
space group	*I*-43*d*	*I*-43*d*	*I*-43*d*	*I*-43*d*	*I*-43*d*	*I*-43*d*	*I*-43*d*	*I*-43*d*
density[b]	0.387	0.392	0.396	0.401	0.429	0.435	0.438	0.444
surface area[c]	4450	4480	3910	3790	3910	3000	3820	4000
pore volume[d]	2.16	2.15	1.84	1.84	1.84	1.30	1.74	1.93
void fraction[e]	0.892	0.894	0.888	0.891	0.858	0.858	0.853	0.853
CO_2 uptake[f]	30.3	32.3	31.5	30.5	46.4	37.5	52.7	58.8

[a]In Å. [b]In g/cm^3, determined from X-ray crystal structures. [c]In m^2/g, derived from N_2 adsorption isotherms at 77 K using the BET method.[190] [d]In cm^3/g, calculated from N_2 adsorption isotherms at 77K. [e]Calculated using helium insertion method[195] in the RASPA code.[197] [f]Excess adsorption at 273 K and 120 kPa, in cm^3/g (STP).

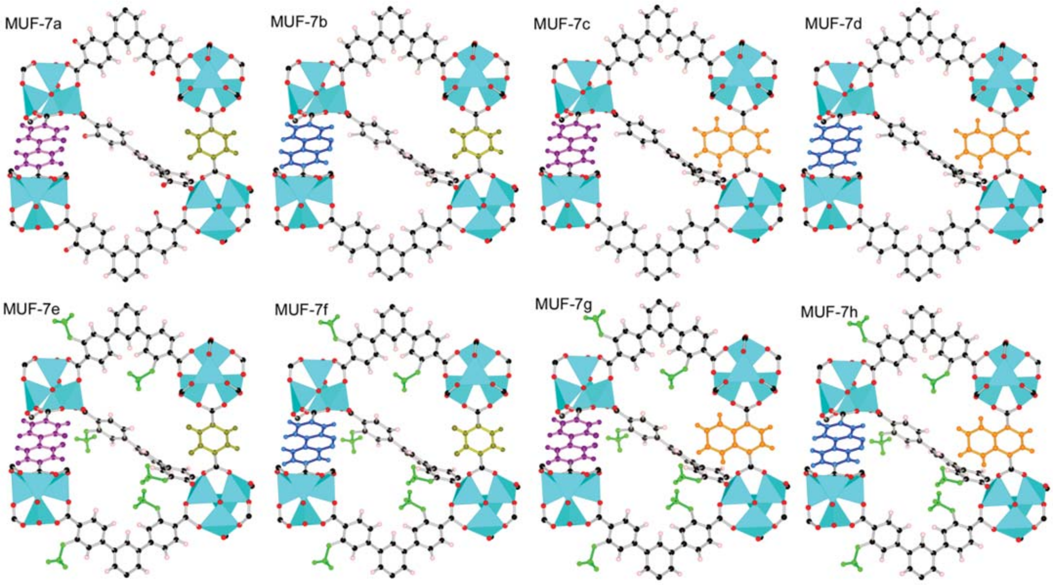

Figure 3.8 Systematic modulation of the three ligands of MUF-7a to produce MUF-7b-h. This delivers an isoreticular set of MOFs with programmed pores. The bpdc ligand is highlighted in purple, bcc in blue, bdc in khaki, ndc in orange, and the methoxy groups of btb-OMe in green.

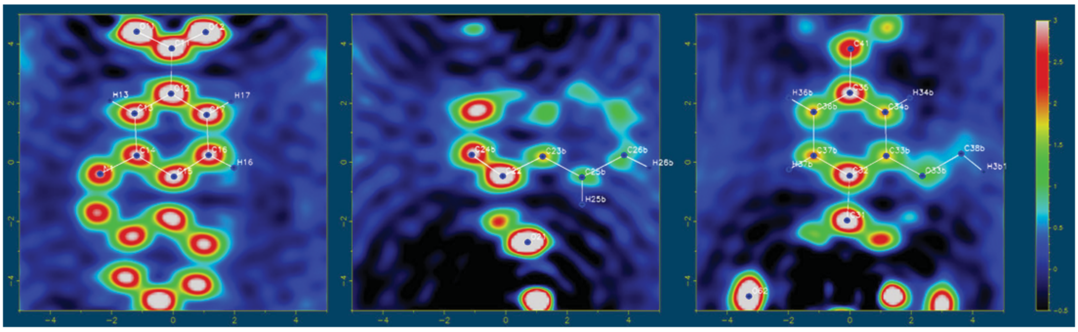

Figure 3.9 Selected observed electron density maps generated from the single crystal XRD data of MUF-h showing the functional groups of bcc (left), ndc (middle) and btb-OMe (right) are exclusively on one side of their carboxyl-carboxyl axes without positional disorder.

Table 3.4 Structures and bending angles of bpdc, bcc, bdc and ndc ligands obtained from MUF-7a/h crystal structures and DFT calculations

	MUF-7a	MUF-7h	Geometry optimized[b]
ligand structures and bending angles (°)[a]	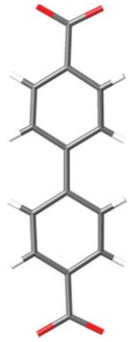 178.1	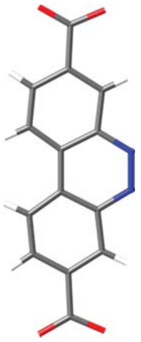 172.6	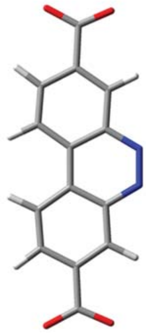 173.5
	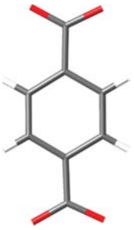 178.8	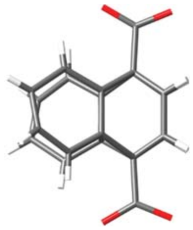 176.3	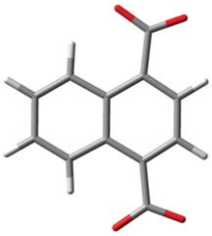 172.9

[a]Bending angles for bpdc/bcc linkers are defined by the two carboxyl carbon atoms and the centroid of 4 and 4′ carbon atoms. Bending angles for bdc/ndc linkers are defined by the two carboxyl carbon atoms and the centroid of the bdc phenyl ring. [b]DFT/B3LYP/6-31G.

The preferred rotational orientations of the linear linkers can be explained by comparing their crystallographic ligand geometries and their optimized ligand structures using DFT methods. The single crystal structure of MUF-7a shows that the carboxyl-carboxyl axes of the bpdc and bdc ligands are both slightly bent even without functional groups (Table 3.4). This distortion probably arises to accommodate the bpdc and bdc linkers, which have different lengths in the same lattice (Figure 2.3). Geometry-optimized structures of the functionalized linear ligands, bcc and ndc, also exhibit a degree of bending even as free anions. This distortion is maintained when they are incorporated into the MOF lattice and ensures that their appended functional groups are positioned exclusively on one side of their carboxyl-carboxyl axis.

The three linkers of MUF-7b-h are perfectly ordered in the crystal lattice. This has a very interesting consequence for one of the tetrahedral pores in these MOFs: it accommodates both the bcc and ndc functional groups (Figure 3.8). This pore has a complex pore environment yet it is perfectly ordered and all pores in the crystal are identical. Therefore we termed MUF-7b-h “programmed-pore” MOFs since their pore environments are regular and are determined by the substituents on the component ligands.

3.2.3 Porosity and gas adsorption studies

The ^{1}H NMR spectra of acid digested as-synthesized crystals of MUF-7b-h show a significant amount of occluded DEF solvent. Thermogravimetric analysis (TGA) reveals significant weight loss up to 50 °C, showing that the frameworks retain ~50-70 wt% solvent upon exchange with CH_2Cl_2 (Figure 3.10). These results are consistent with the large void spaces observed by X-ray crystallography and in good agreement with their calculated void fractions (Table 3.3).

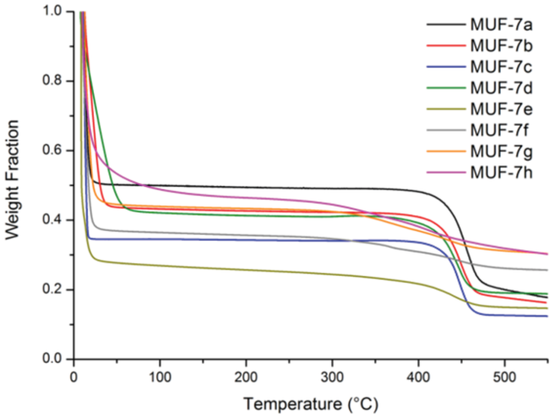

Figure 3.10 Thermogravimetric analysis (TGA) traces of CH_2Cl_2-solvated MUF-7a-h.

MUF-7b-h are permanently porous upon careful activation (heating to 80 °C with a rate of 1 °C/min under dynamic vacuum). At 77 K, N_2 adsorption isotherms display a saturation uptake capacity between 800 and 1400 cm^3(STP)/g (Figure 3.11). Two-step steep rises in these isotherms were observed for all samples, corresponding to Type II isotherms,[213] which are characteristic of mesoporous materials and consistent with the pore dimensions observed by X-ray crystallography. The BET surface areas of MUF-7b-h calculated from their N_2 adsorption isotherms are between 3000 and 4500 m^2/g (Table 3.3), and their total pore volumes are estimated to be between 1.30 and 2.15 cm^3/g (Table 3.3). We note that MUF-7f exhibits slightly reduced values due to the difficulties in fully activating this material.

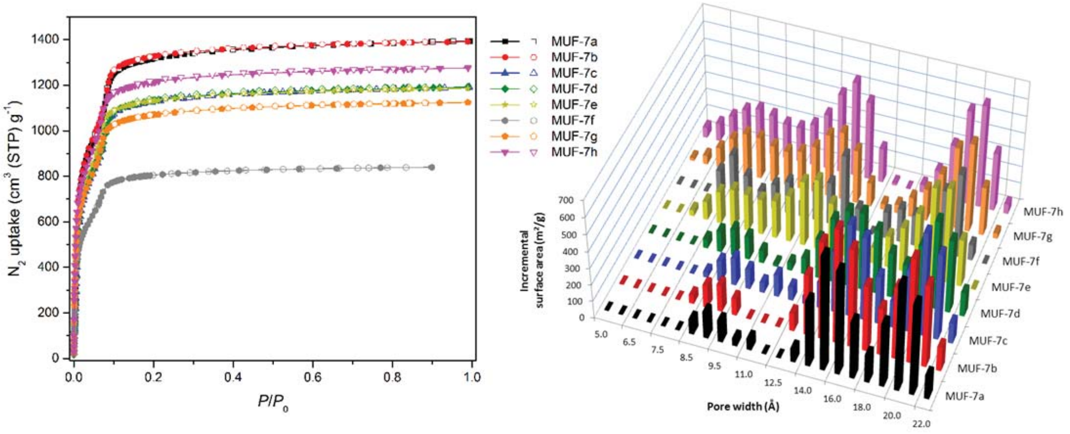

Figure 3.11 Left: N$_2$ adsorption (closed symbols) and desorption (open symbols) isotherms measured at 77K for MUF-7a-h. Right: Pore size distribution plots for MUF-7a-h, calculated from N$_2$ isotherms measured at 77 K.

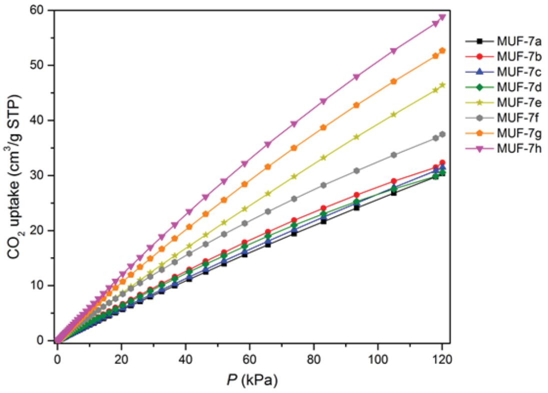

Figure 3.12 CO$_2$ adsorption isotherms measured for MUF-7a-h at 273 K.

This series of MOFs displays a fascinating trend in its CO$_2$ adsorption isotherms (Figure 3.12). For MOFs with btb ligands (MUF-7a-d), the CO$_2$ adsorption capacities are clustered within a small range. Conversely, differences are pronounced for MOFs with btb-OMe ligands (MUF-7e-h,). The functional groups on bcc and ndc ligands exert an impact on CO$_2$ adsorption only when methoxy groups are present, enhancing CO$_2$ adsorption capacity by up to 94%. Similar levels of enhancement typically require the introduction of highly polar functional groups on the pore surface.[159]

It appears that a synergistic effect operates amongst these ligands since the CO$_2$ uptake capacities are nonlinear. This synergistic effect may arise from the pore topography of these MOFs. Their pore-size distributions, calculated from their N$_2$ adsorption isotherms measured at 77 K, are modulated by the ligand functional groups (Figure 3.11). Across the MUF-7a-h series, a larger population of smaller tetrahedral pores (6 - 12 Å) appears due to the increasing bulk of the ligands. On the other hand, the large dodecahedral pores, with a diameter of ~19 Å, are largely unaffected by the ligand substituents, consistent with the X-ray crystallographic results. The relationship between pore size and CO_2 adsorption capacity is illustrated in a recent theoretical study: Wilmer et al. simulated CO_2 adsorption of over 130,000 hypothetical MOFs and found the optimal pore diameter is around 6 – 12 Å.[200] The appearance of pores in the size regime in MUF-7e-h underlines their high CO_2 adsorption capacities.

3.3 Conclusion

In summary, to generate MOFs that are complex and modular yet well ordered, we developed a strategy of systematic functionalization of a quaternary MOF that is constructed with three topologically distinct linkers. By introducing substituted analogues of these ligands, a set of isoreticular frameworks is delivered, with the MOF structure rationally varied while the topology is maintained. To combat randomness and disorder, the substitution patterns of the ligands are judiciously designed to be compatible with their crystallographic site symmetries. MOFs produced in this way feature "programmed-pores" – multiple functional groups compartmentalized in a predetermined array with a periodic lattice – and are capable of complex functional behaviour. Synergistic effects between multiple functional groups introduced *via* a pore-programming approach elevate the properties of PP-MOFs beyond conventional frameworks. In these examples, unconventional CO_2 adsorption trends, including capacity enhancement close to 100%, emerge from synergistic effects.

Shortly after we published our report on MUF-7a-h, Matzger's group reported another family of Zn_4O based quaternary MOFs.[214] Zhou's group also reported some zirconium based quaternary MOFs around the same time is as the results from Chapter 4 were published.[215]

3.4 Experimental section

General procedures, TGA, PXRD and gas adsorption measurements follow the same protocols described in Chapter 2. ^{1}H NMR spectroscopy of digested MOF samples are acquired using the same procedure with the spectra available in Electronic Appendix A.

3.4.1 Ligand synthesis

H_3**L1**[216,217] and H_3btb-OMe[211] were synthesized following literature procedures with their NMR spectra match those originally reported.[211] The synthesis of H_3**L2** and partial synthesis of H_3**L3** is available in Electronic Appendix A.

H_2bcc was synthesized according to the following route with detailed procedures and characterization data of its intermediates available in Electronic Appendix A:

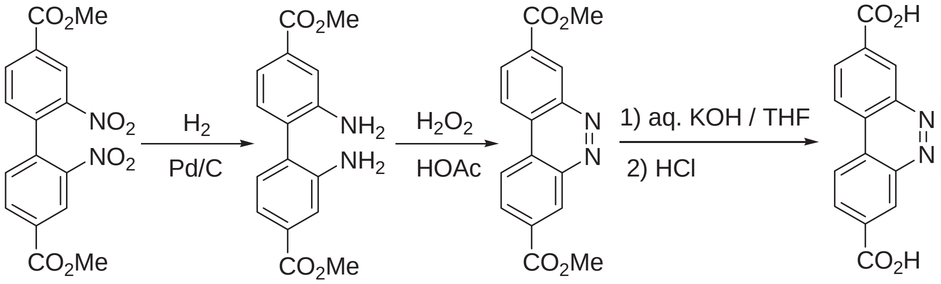

H_2bcc: ^{1}H NMR (400 MHz, DMSO-*d*$_6$): δ 8.53 (dd, *J* = 8.5 Hz, 1.7 Hz, 2H), 9.08 (d, *J* = 8.6 Hz, 2H), 9.20 (d, *J* = 1.5 Hz, 2H), 13.7 (s, 2H) ppm. ^{13}C NMR (125 MHz, D_2O/KOH): δ 121.71, 121.93, 129.91, 132.62, 138.36, 143.48, 173.03 ppm. ES-MS (negative mode, H_2O/KOH/CH_3OH): m/z = 133.22 ($[C_{14}H_6N_2O_4]^{2-}$, calcd. 133.02). Anal. calcd. for $(C_{14}H_8N_2O_4)\cdot 1.25H_2O$: C, 57.83; H, 3.64; N, 9.64; Found: C, 57.84; H, 3.17; N, 9.53. FT-IR: 1699 (s), 1619 (m), 1577 (w), 1543 (w), 1479 (w), 1418 (m), 1363 (w), 1286 (s), 1220 (s), 1152 (w), 1126 (w), 916 (m), 835 (m), 755 (s), 731 (m).

3.4.2 MOF synthesis and characterization

MOF synthesis was carried out in at oven maintained at 85 °C. For IR spectroscopy, the mother liquor was removed and the crystals were washed with fresh dry DEF three times. Solvent exchange with CH_2Cl_2, which was exchanged three times over three days, was then carried out. Where necessary, complete desolvation was achieved in an 80 °C vacuum oven.

In general, three ligands and zinc nitrate tetrahydrate were dissolved or well-suspended in DEF in a scintillation vial. Crystal seeds were added when needed. The vial was heated to 85 °C for various period of time and allowed to cool naturally. This yields crystals of MUF-7b-h. To scale up the synthesis, multiple reactions were carried out and the crystals were combined for further analyses. Detailed procedures and additional characterization data (^{1}H NMR spectra and optical microscopy images) of MUF-7b-h is available in Electronic Appendix A.

3.4.3 Single crystal x-ray diffraction

MOF crystals were mounted together with some dry DEF in a polymer sleeve on a Rigaku Spider diffractometer equipped with a MicroMax MM007 rotating anode generator (Cu radiation, 1.54180 Å), high-flux Osmic multilayer mirror optics, and a curved image-plate detector. Data were collected at 293 K and were integrated and scaled and averaged with FS Process.[203] XPREP[204] was used to determine the space group and the structures were solved using SHELXS[204] and refined with SHELXL.[204]

All atoms were found in the electron density difference map except the carbon atoms of some of the methoxy groups of the btb-OMe ligands, which were placed in chemically reasonable positions. Electron density difference maps were carefully analyzed for the possible presence of disordered framework components. All non-hydrogen atoms were refined anisotropically (except for some methoxy groups of the btb-OMe ligands as described below). Unrestrained atomic displacement parameters sometimes produced high U_{eq} values during the refinement thus ISOR, DELU and SIMU commands were introduced as appropriate with careful adjustments of the standard deviations. FLAT commands were introduced for some phenyl rings.

The ndc ligands in MUF-7c, MUF-7d, MUF-7g and MUF-7h were found to be disordered across a twofold symmetry element that results in slightly different orientations of this ligand. In certain cases FLAT and SADI commands were employed to produce a chemically realistic model of the naphthyl rings. In MUF7a-d, most bridging phenyl rings of the btb ligands were disordered. A free variable was used in each case to define the relative occupancies of the two sites corresponding to two slightly different conformation of this ligand. In MUF-7e-h, most bridging phenyl rings and appended methoxy groups of the btb-OMe ligands were disordered over two sites. Again, a free variable was used in each case to define the relative occupancies of the two sites. This disorder hampered an unrestrained refinement of these phenyl rings and methoxy substituents therefore the following restraints were used when necessary: (i) C and O atoms were refined isotropically, (ii) DFIX restraints were employed for the C—OMe bond, (iii) a FLAT command to ensure the O atom was co-planar with the phenyl ring, and (iv) the phenyl rings were modeled as ideal hexagons.

3.4.4 Computational details

Geometric surface area, theoretical pore volume and void fraction calculations follow the exact same procedure in Chapter 2. Geometry optimization calculations were performed using Gaussian 09.[212] Calculations were carried out by using density functional theory (DFT), with Becke's three-parameter exchange functional (B3)[218] in combination with the correlation functional of Lee, Yang and Parr (LYP).[219] The 6-31(G) basis set was used for all geometry optimization calculations. Tables containing atomic coordinates for optimized structures for ligand anions are available in Electronic Appendix A.

Chapter 4

Quaternary MOFs with Enhanced Water Stability

4.1 Introduction

In Chapter 3, we demonstrated the chemistry of pore programming in quaternary MOFs for the first time. The success in this proof-of-concept study provides a solid ground for further pursuing more complicated and advanced chemistry in quaternary MOFs. However, there is one practical challenge that needs to be addressed before we move in this direction – the water sensitivity of the MUF-7 family. In fact, the water sensitivity of Zn_4O-carboxylate MOFs is one of the biggest concerns in the MOF community, especially given the numerous advantages of using zinc, such as its low toxicity, huge abundance, relative low density and reliable synthesis that usually produce crystals suitable for structure determination.[20,81,220] Studies focusing on enhancing the hydrolytic stability of Zn_4O MOFs are rarely documented in the literature.[182,221-224] Most of these early studies used PXRD alone to determine whether these MOFs are stable after exposure to liquid or gaseous water, which could be deceptive. This is because if a MOF is partially collapsed, say 80% of its porosity is lost after water exposure, the remaining 20% of the crystalline portion will strongly contribute to the PXRD signal, whereas the 80% portion, which is usually amorphous, is undetectable.

4.2 Results and discussion

4.2.1 Synthesis and structure of MUF-77-ethyl

To induce greater water stability in MUF-7 analogues, we decided to employ truxene-based ligands in place of btb. These ligands maintain the three-fold symmetry of btb, but are much more rigid and can be easily functionalized with hydrophobic alkyl groups (R groups, Scheme 4.1). The first member of this truxene series of ligands is H_3hett (Figure 4.1, hett = 5,5',10,10',15,15'-hexaethyltruxene-2,7,12-tricarboxylate). This ligand has been reported in the literature, as has its hexamethyl analogue.[202,225] The other truxene ligands reported in this chapter were not known prior to this study. A more efficient synthetic route than that described in the literature was developed for these ligands. This relied on the Friedel-Crafts acetylation of alkylated truxene rather than bromination followed by carboxylation.

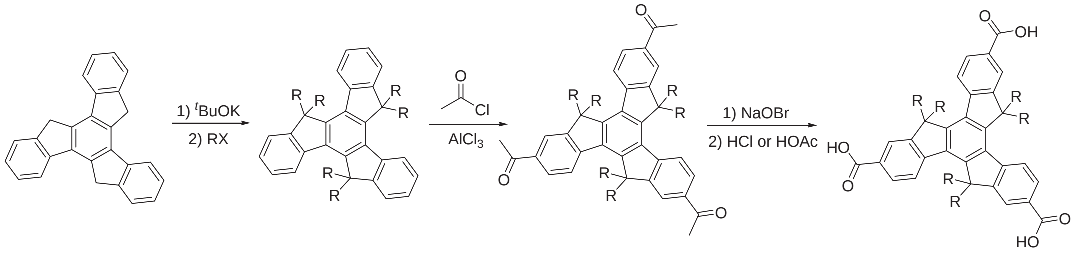

Scheme 4.1 The synthetic route to truxene ligands

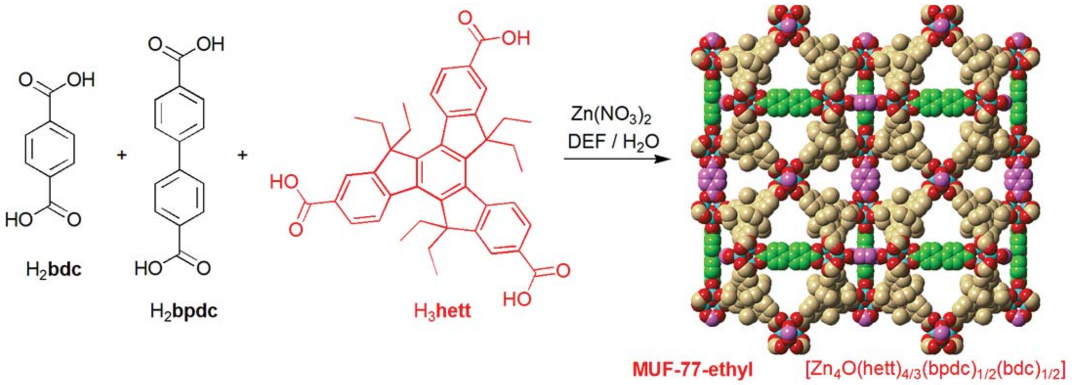

Figure 4.1 The synthetic route to MUF-77-ethyl and a view of its network structure, as determined by X-ray crystallography. Three ligands in the network structure are coloured as light brown (hett), green (bpdc) and pink (bdc).

Reacting H_3hett, H_2bpdc, and H_2bdc with $Zn(NO_3)_2$ produces MUF-77-ethyl, a quaternary metal-organic framework with the formula $[Zn_4O(hett)_{4/3}(bpdc)_{1/2}(bdc)_{1/2}]$ (Figure 4.1). Single crystal x-ray diffraction experiment indicates that MUF-77-ethyl belongs to the cubic space group *Pm*-3 with a density of 0.49 cm^3/g (Table 4.1). Similar to MUF-7a, the bulk phase purity of MUF-77-ethyl was determined by powder X-ray diffraction (Figure 4.2), ^{1}H NMR spectroscopy of a digested sample (Figure 4.3), optical microscopy, and elemental analysis.

By optimizing the synthetic route to MUF-77-ethyl we were able to obtain this material in high yield and with perfect phase purity. MUF-77-ethyl appears to be a thermodynamically stable phase that is readily assembled at the expense of competing phases. In contrast to many members of the MUF-7 family, the formation of MUF-77-ethyl is not particularly sensitive to the feed ratio of the three ligands and does not require crystal seeding.

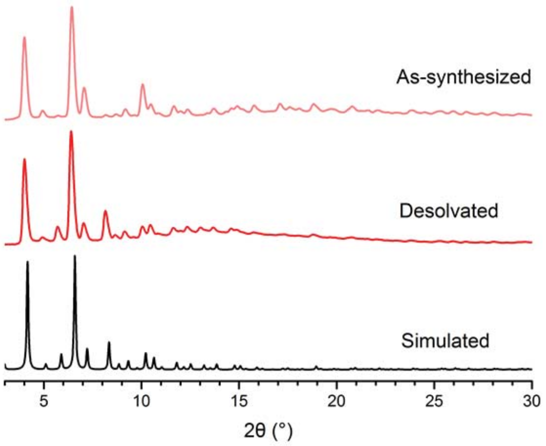

Figure 4.2 Simulated and experimental PXRD patterns of MUF-77-ethyl.

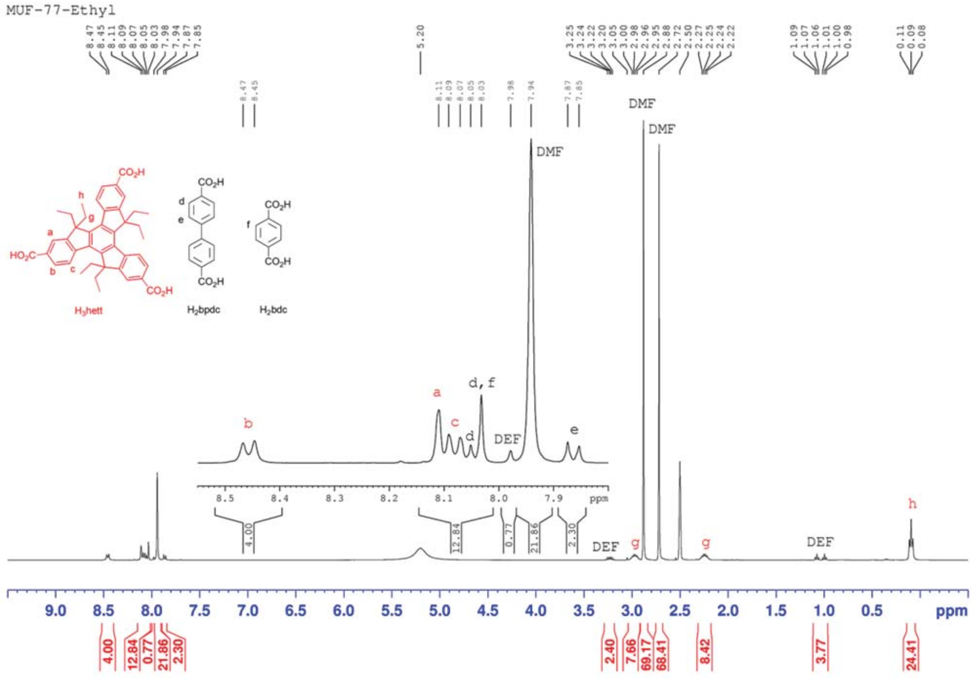

Figure 4.3 ^{1}H NMR spectrum of MUF-77-ethyl (with occluded DMF solvent molecules) digested with DMSO-d_6/DCl showing the integrals that match with the formula $[Zn_4O(hett)_{4/3}(bpdc)_{1/2}(bdc)_{1/2}]$.

MUF-77-ethyl features two types of dodecahedral cavity and one type of tetrahedral cavity, as highlighted in Figure 4.4. The larger dodecahedral cavity is defined by twelve Zn_4O clusters, eight hett ligands and six bpdc ligands, while bdc ligands replace the bpdc ligands around the smaller dodecahedral cavity. Each tetrahedral cavity is delineated by four Zn_4O clusters, four hett ligands, a bpdc ligand and a bdc ligand.

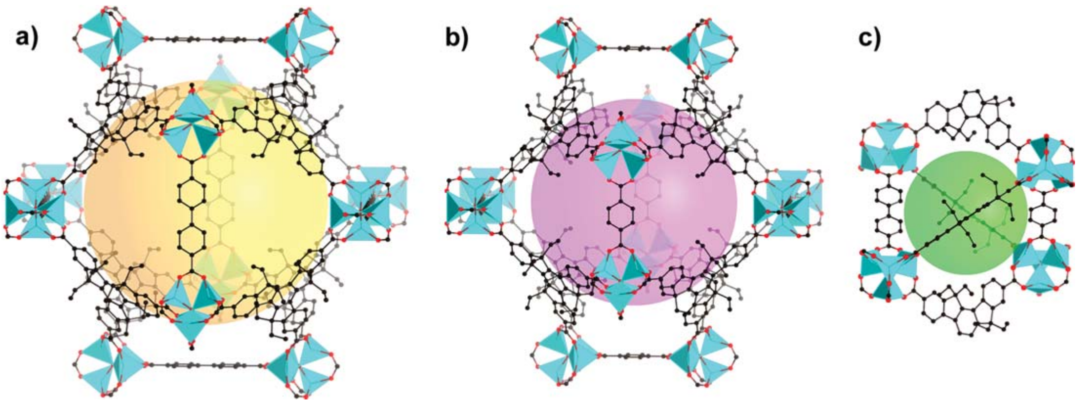

Figure 4.4 Views of the X-ray crystal structure of MUF-77-ethyl highlighting (a) the larger dodecahedral cavity, (b) the smaller dodecahedral cavity, and (c) the tetrahedral cavity. Hydrogen atoms are omitted for clarity.

The larger dodecahedral mesopore of MUF-77-ethyl spans 34.5 Å at its widest point and can accommodate a sphere with a diameter of 18.5 Å (Figure 4.4a). The smaller dodecahedron has an interatomic span of 32.6 Å and accommodates a 16.5 Å sphere (Figure 4.4b). The tetrahedral cavity can house a sphere of diameter ~10 Å (Figure 4.4c). The free pore diameter, which is defined as the diameter of the largest sphere which can freely pass throughout the framework, is calculated to be 6.5 Å.[226]

It is illustrative to compare the structural characteristics of MUF-77-ethyl with those of MUF-7a, which is constructed from Zn_4O SBUs and bdc, bpdc and btb linkers (Figure 4.5).[191] In both cases the three ligands are linked by six-connected Zn_4O SBUs into a framework with **ith-d** topology. At each SBU four tritopic ligands occupy the equatorial positions, and one bpdc and one bdc ligand fill the axial sites. Differences arise due to the lower symmetry of MUF-7a, which generates three distinct tetrahedral cavities with diameters of ~10 Å, along with a unique dodecahedral cavity which spans 33.7 Å at its widest point. The free pore diameter of MUF-7a is 9.1 Å, which is larger than that of MUF-77-ethyl due to the bulky truxene ligand of the latter.

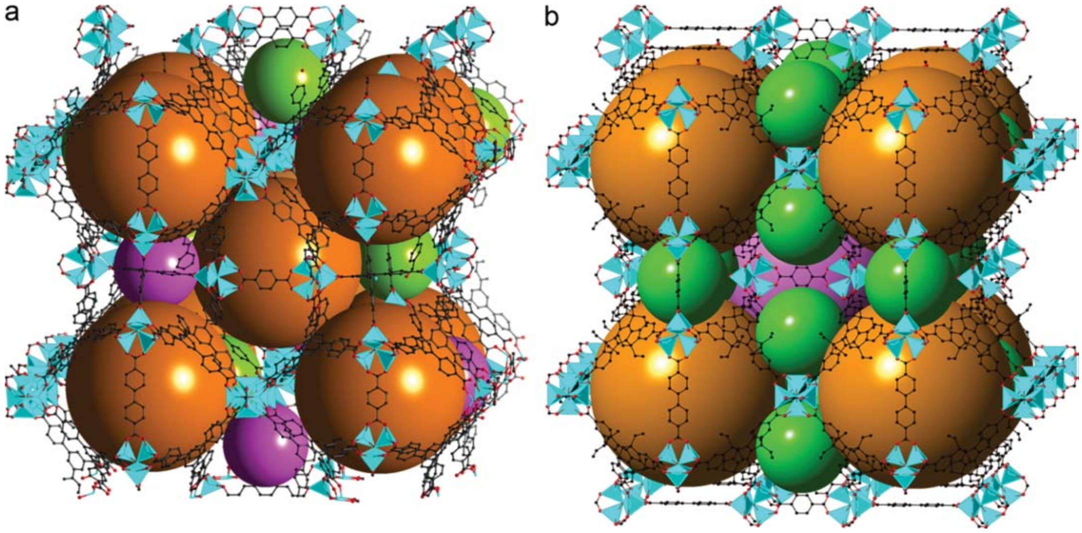

Figure 4.5 Comparison of MUF-7a (a) and MUF-77-ethyl (b).

The solvent occluded in the pores of MUF-77-ethyl during synthesis is easily removed to produce an activated material that has a high affinity for molecular guests. Its capacity for taking up N_2 at 77 K is 1004 cm^3/g. A BET surface area of 3600 m^2/g and a pore volume of 1.53 cm^3/g were calculated from the adsorption isotherm (Figure 4.6). The close agreement of these values to the calculated geometric surface area (3850 m^2/g)[194] and the theoretical pore volume (1.52 cm^3/g, calculated by PLATON[227]) underscore the stability of the framework in the absence of guest solvent.

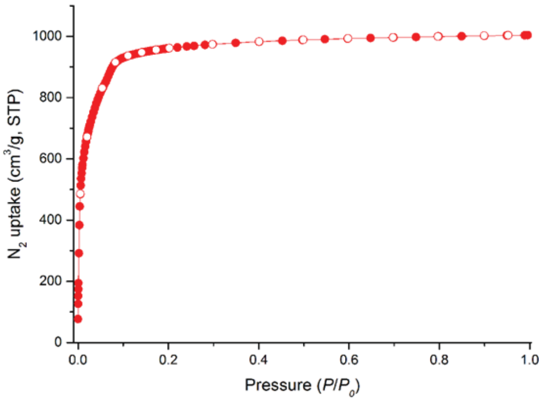

Figure 4.6 Nitrogen adsorption (filled circles) and desorption (open circles) isotherm of MUF-77-ethyl measured at 77 K.

4.2.2 Water stability of MUF-77-ethyl

We were delighted to find that MUF-77-ethyl is relatively stable towards water vapour. Following removal of the occluded solvent, a sample was exposed to ambient air (40-50 % RH) at 20 °C for 205 days. No changes to the morphology or transparency of the crystals were detectable by optical microscopy (Figure 4.7). Powder XRD patterns were recorded throughout the exposure period and they were found to remain unchanged (Figure 4.8). A single crystal of MUF-77-ethyl exposed to ambient air for 35 days displayed an excellent single-crystal X-ray diffraction pattern to a resolution beyond 0.81 Å (Figure 4.9). A full set of crystallographic data recorded on this aged crystal yielded refinement statistics superior to a freshly-prepared, solvated specimen. As a point of comparison, activated MUF-7a exposed to air for only 32 hours produces a poor single-crystal diffraction pattern, indicating a loss of crystallinity (Figure 4.9), and notable changes are evident in its PXRD pattern after several days (Electronic Appendix B).

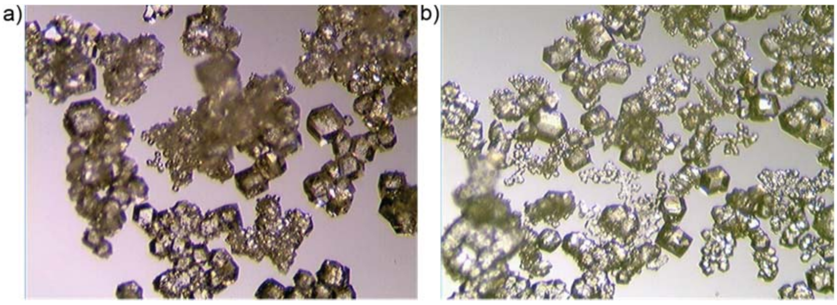

Figure 4.7 Microscopy images of MUF-77-ethyl crystals after being aged at 40-45 % RH for a) 24 hours and b) 205 days.

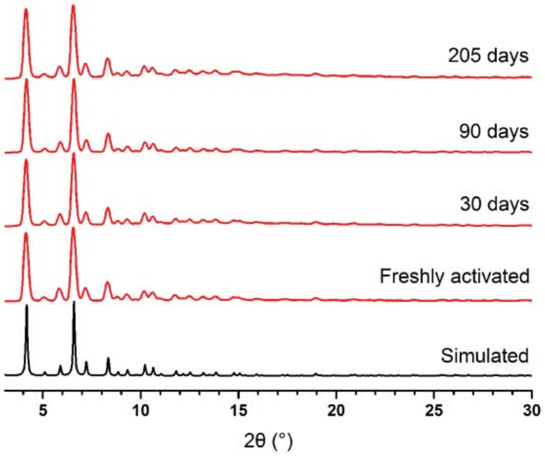

Figure 4.8 Powder X-ray diffraction patterns (Cu_{α} radiation) of MUF-77-ethyl; freshly activated and aged samples exposed to 40-50 % relative humidity at 20 °C for the stated period.

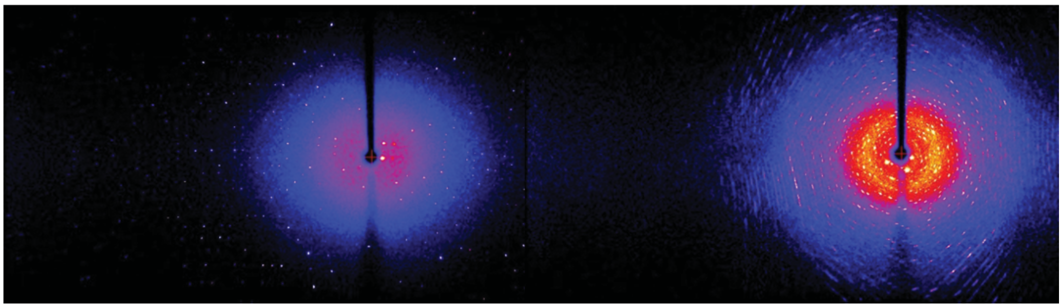

Figure 4.9 Left: A representative diffraction image of a desolvated single crystal of MUF-77-ethyl which had been aged at 40-50% relative humidity at 20 °C for 35 days. Right: A representative diffraction image of a desolvated single crystal of MUF-7a which had been aged at 40-50% relative humidity at 20 °C for 32 hours.

To quantify the stability of MUF-77-ethyl towards humid air we turned to the measurement of gas adsorption isotherms before and after periods of exposure to ambient air. This allows the porosity of an aged sample to be compared to its pristine state. Following the exposure of MUF-77-ethyl to humid air (RH = 40 – 50%) for 3 and 11 days, CO_2 (273 K) and N_2 (77 K) isotherms were measured (Figure 4.10 and Table 4.2). The uptake of CO_2 by aged MUF-77-ethyl is 42.8 and 42.6 cm^3/g (at 1 atm) after 3 and 11 days, respectively, which is almost identical to a pristine sample (42.9 cm^3/g). The pore volumes calculated from N_2 adsorption isotherms after 3 and 11 days aging are 1.54 and 1.51 cm^3/g, respectively, which are close to its pristine state (1.55 cm^3/g). Remarkably, prolonged aging for 100 days did not reduce its pore volume (1.59 cm^3/g, Figure 4.10). Conversely, considerable losses in porosity and CO_2 uptake capacity were found for MUF-7a under the same conditions (Figure 4.11 and Table 4.2)

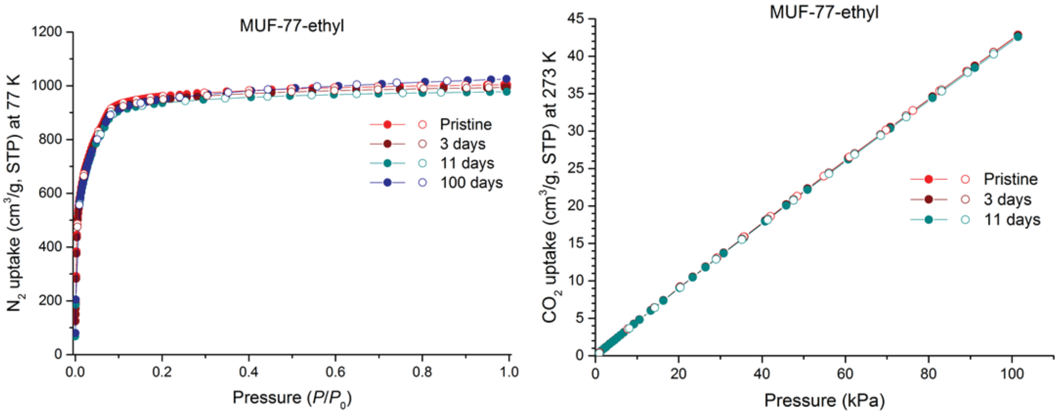

Figure 4.10 Left: Nitrogen adsorption (filled circles) and desorption (open circles) isotherms measured at 77 K for pristine and aged MUF-77-ethyl under 40-50% relative humidity. Right: CO_2 adsorption (filled circles) and desorption (open circles) isotherms measured at 273 K for pristine and aged MUF-77-ethyl under 40-50% relative humidity.

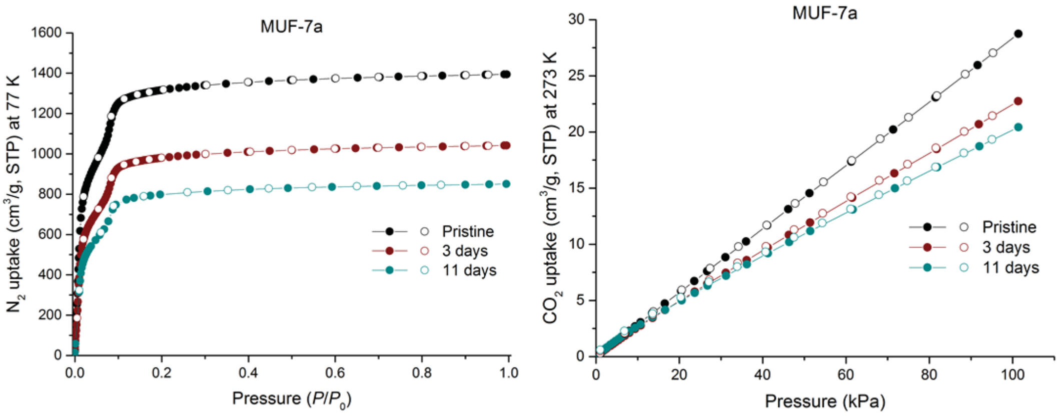

Figure 4.11 Left: Nitrogen adsorption (filled circles) and desorption (open circles) isotherms measured at 77 K for pristine and aged MUF-7a under 40-50% relative humidity. Right: CO_2 adsorption (filled circles) and desorption (open circles) isotherms measured at 273 K for pristine and aged MUF-7a under 40-50% relative humidity.

The observed stability of MUF-77-ethyl, which indicates that it can be handled indefinitely under typical laboratory conditions, is a surprising revelation. It is well established that Zn_4O-carboxylate MOFs are prone to decomposition by water vapour.[220,221,223,228,229] The instability of MUF-7a described above is typical for this class of MOF. In other examples, MOF-5[3] and UMCM-1[55] are known to degrade rapidly in ambient conditions,[221,223,228] and MOF-177,[12] which is used as an adsorbent in prototype natural gas fuel tanks,[230] collapses upon exposure to 40% RH for three days.[229] Although a few literature examples have shown moderate resistance to moisture,[182,221,223,224,231] improving their stability in this regard is of considerable current interest.[222,224,231]

Both MUF-77-ethyl and MUF-7a are quaternary MOFs that are constructed from similar ligand sets and identical SBUs. Why does their stability toward humid air differ so remarkably? We note that the major difference between the frameworks is the identity of the tritopic ligand: hett in MUF-77-ethyl and btb in MUF-7a. On this basis, there are two plausible reasons behind the superior stability of MUF-77-ethyl: First, hett is more hydrophobic than btb, which may lead to a drop in the affinity of MUF-77-ethyl for water vapour vis-à-vis MUF-7a. Second, the truxene backbone of hett is more rigid than btb, which may impede substitution reactions, such as hydrolysis, at the Zn_4O SBUs. Differences in basicity arising from the electron-rich truxene core may be discounted since the estimated pKa of H_3hett (3.42 ± 0.70) is very similar to that of H_3btb (3.46 ± 0.10).[232]

4.2.3 Synthesis and structure of other MUF-77 frameworks

To examine these points in detail and optimize this class of MOF for water stability, we designed a family of truxene-based tritopic ligands that feature alkyl chains of different lengths (Figure 4.12). Since the overall geometry of these ligands is the same as the hett ligand, we anticipated that quaternary MOFs which are isoreticular to MUF-77-ethyl could be produced. We indeed found this to be the case and were able to prepare the five new quaternary MOFs depicted in Figure 4.12 in high yield and perfect phase purity. We characterized these frameworks by single crystal XRD (Table 4.1), ^{1}H NMR spectroscopy of digested samples (Electronic Appendix B), PXRD (Electronic Appendix B), optical microscopy, and elemental analyses.

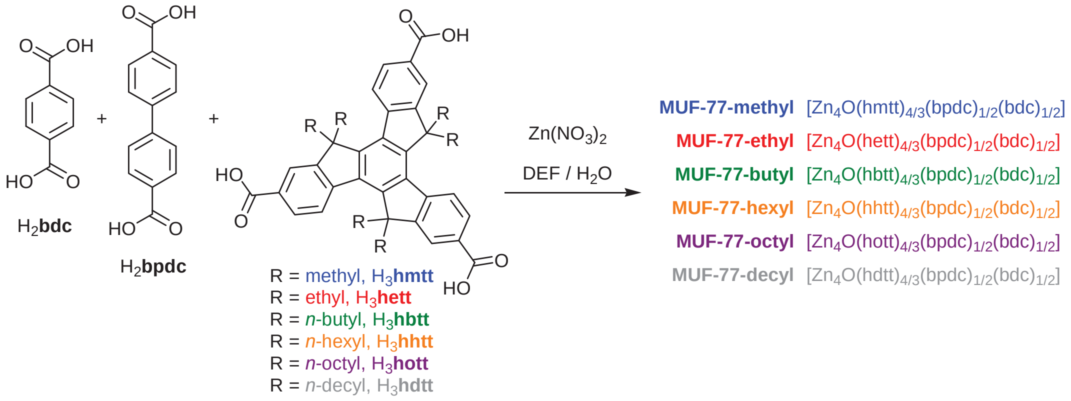

Figure 4.12 Synthetic route to the MUF-77 series of materials.

The resistance of these materials to atmospheric water vapour enabled us to use desolvated crystals for all single crystal X-ray diffraction experiments. The structures of MUF-77-methyl and -butyl indicate that the alkyl chains extend normal to the truxene plane (as observed for MUF-77-ethyl) and are directed into both the large and small dodecahedral cavities. This appears to be a favorable alignment of the alkyl chains based on the solid state structure of 2,7,12-triacetyl-5,5',10,10',15,15'-hexaoctyltruxene (Figure 4.13). Shorter alkyl chains (up to hexyl) can be fully accommodated in the large dodecahedral cavities (Figure 4.14). The tetrahedral cavities (diameters ~8 Å), on the other hand, are largely unaffected. It was not possible to accurately model the disposition of the alkyl chains in MUF-77-octyl and -decyl using X-ray crystallography data due to disorder, although it is evident that they occupy most of the dodecahedral void spaces and spill over into the tetrahedral cavities.

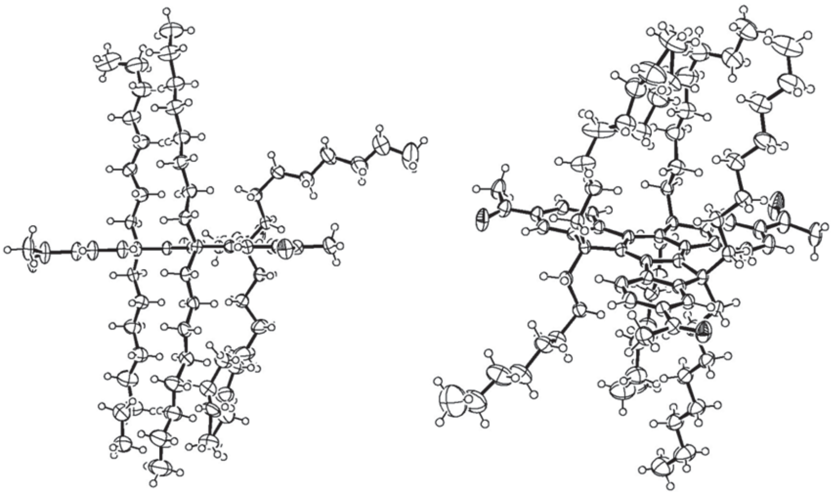

Figure 4.13 ORTEP diagrams for 2,7,12-triacetyl-5,5′,10,10′-15,15′-hexaoctyltruxene showing 50% ellipsoid probability.

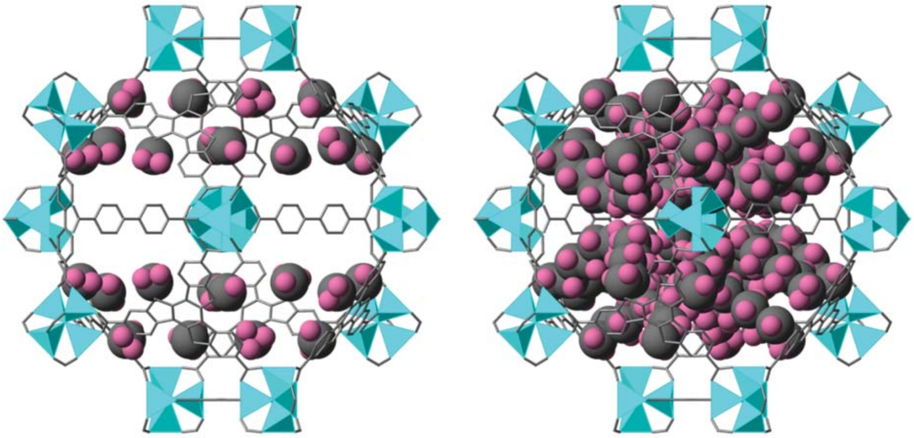

Figure 4.14 Views of the large dodecahedral cavities of MUF-77-methyl (left) and MUF-77-hexyl (right) showing the alkyl groups appended to the truxene ligand in space-filling mode.

Table 4.1 X-ray crystallography: summary of data collection and refinement details the MUF-77 series.

MOF	**MUF-77-methyl**	**MUF-77-ethyl**	**MUF-77-butyl**	**MUF-77-hexyl**	**MUF-77-octyl**	**MUF-77-decyl**
Formula	$C_{59}H_{42}O_{13}Zn_4$	$C_{67}H_{58}O_{13}Zn_4$	$C_{83}H_{90}O_{13}Zn_4$	$C_{99}H_{122}O_{13}Zn_4$	$C_{115}H_{154}O_{13}Zn_4$	$C_{131}H_{186}O_{13}Zn_4$
Formula weight	1220.40	1332.61	1557.02	1781.44	2005.85	2230.27
Crystal size (mm)	0.864x0.721x0.633	0.282x0.278x0.252	0.700x0.652x0.586	0.719x0.708x0.615	0.500x0.458x0.452	0.488x0.433x0.415
Temperature (K)	293(2)	293(2)	293(2)	293(2)	293(2)	293(2)
Wavelength (Å)	1.54178	1.54178	1.54178	1.54178	1.54178	1.54178
Crystal system	cubic	cubic	cubic	cubic	cubic	cubic
Space group	*Pm*-3	*Pm*-3	*Pm*-3	*Pm*-3	*Pm*-3	*Pm*-3
Unit cell length (Å)	29.9525(3)	29.9508(5)	29.9363(5)	29.8614(5)	29.8116(15)	29.8062(3)
Unit cell volume (Å^3)	26872.0(8)	26867.4(13)	26828.4(13)	26627.5(13)	26495(4)	26480.1(8)
Z	6	6	6	6	6	6
D_{calc} (g cm^{-3})	0.452	0.494	0.578	0.667	0.754	0.839
μ (mm^{-1})	0.769	0.785	0.819	0.858	0.896	0.929
F(000)	3720	4104	4872	5640	6408	7176
Reflns coll. / unique	63191 / 9240	135510 / 9309	135481 / 9304	84708 / 9163	65369 / 6768	59507 / 9137
R_{int}	0.0319	0.0345	0.0337	0.0543	0.0371	0.0308
Data range (Å)	0.81 < d < 6.7	0.81 < d < 6.7	0.81 < d < 6.7	0.81 < d < 6.7	0.90 < d < 6.7	0.81 < d < 6.7
Index ranges	$-22 \le h \le 27$ $-28 \le k \le 35$ $-36 \le l \le 18$	$-18 \le h \le 33$ $-32 \le k \le 36$ $-36 \le l \le 36$	$-34 \le h \le 35$ $-36 \le k \le 26$ $-28 \le l \le 36$	$-20 \le h \le 28$ $-36 \le k \le 36$ $-20 \le l \le 36$	$-32 \le h \le 33$ $-20 \le k \le 17$ $-23 \le l \le 33$	$-26 \le h \le 35$ $-34 \le k \le 18$ $-26 \le l \le 29$
Completeness	99.3%	99.7%	99.7%	99.6%	99.8%	99.7%
T_{min}, T_{max}	0.70, 1.00	0.74, 1.00	0.75, 1.00	0.57, 1.00	0.37, 1.00	0.70, 1.00
R indices for data with I>2σ(I)	$R_1 = 0.0292$ $wR_2 = 0.0771$	$R_1 = 0.0441$ $wR_2 = 0.1080$	$R_1 = 0.0389$ $wR_2 = 0.1145$	$R_1 = 0.0786$ $wR_2 = 0.2480$	$R_1 = 0.0803$ $wR_2 = 0.2579$	$R_1 = 0.1115$ $wR_2 = 0.3743$
R indices for all data	$R_1 = 0.0315$ $wR_2 = 0.0797$	$R_1 = 0.0500$ $wR_2 = 0.1114$	$R_1 = 0.0404$ $wR_2 = 0.1157$	$R_1 = 0.090=21$ $wR_2 = 0.2602$	$R_1 = 0.0964$ $wR_2 = 0.2756$	$R_1 = 0.1171$ $wR_2 = 0.3777$
Largest difference peak and hole (e Å^{-3})	0.208 / −0.251	0.317 / −0.312	0.261 / −0.247	0.384 / −0.372	0.525 / −0.415	0.711 / −0.772

Table 4.2 Summary of the key properties of the MUF-77 series and MUF-7a.

	MUF-7a	**MUF-77-methyl**	**MUF-77-ethyl**	**MUF-77-butyl**	**MUF-77-hexyl**	**MUF-77-octyl**	**MUF-77-decyl**
ligand set	btb bpdc bdc	hmtt bpdc bdc	hett bpdc bdc	hbtt bpdc bdc	hhtt bpdc bdc	hott bpdc bdc	hdtt bpdc bdc
cell dimension[a]	60.232	29.953	29.951	29.936	29.861	29.812	29.806
space group	*I*-43d	*Pm*-3	*Pm*-3	*Pm*-3	*Pm*-3	*Pm*-3	*Pm*-3
density[b]	0.387	0.452	0.494	0.578	0.667	0.754	0.839
BET surface area[c]	4450	3600	3600	3250	2170	1570	1170
pore volume[d]	2.16	1.85	1.55	1.21	1.00	0.65	0.48
porosity after aging[e]	73/61	98/101	99/98	99/98	86/74	87/75	81/74
CO_2 capacity after aging[f]	79/71	98/99	100/99	99/98	89/83	89/82	87/84
Q_{st}^{0}[g]	15.0/12.9	17.4/14.3	18.1/14.2	19.7/15.5	19.9/15.5	19.5/16.0	16.0/19.8
water conc.[h]	2.06	0.11	0.09	0.22	0.20	0.41	0.46

[a] In Å. [b] In g/cm^3. [c] BET surface area in m^2/g. [d] In cm^3/g, calculated from the N_2 adsorption isotherm at 77 K and P/P_0 = 0.995. [e] At 77 K in % with respect to pristine samples after aging for 3/11 days. [f] At 273 K in % with respect to pristine samples after aging for 3/11 days. [g] Heat of adsorption at zero loading in kJ/mol, CO_2/CH_4. [h] Concentration of adsorbed water in the framework pores in mol/L at 50% RH.

By modulating the lengths of the truxene substituents the pore characteristics of this isoreticular family of MOFs can be systematically modified (Figure 4.15, Figure 4.16 and Table 4.2). All frameworks can be activated by solvent exchange with dichloromethane followed by desolvation under vacuum at 80 °C. N_2 sorption isotherms at 77 K allow the estimation of BET surface areas, which extend from 1170 to 3600 m^2/g. Pore volumes range from 1.85 to 0.48 cm^3/g and are directly related to the size of the alkyl substituent on the truxene ligand. Using a computational method, we calculated their pore size distributions from their single-crystal X-ray structures. This yields a plot of normalized pore population as a function of pore diameter (Figure 4.17). The result shows a reduction in the space available in the two large dodecahedral cavities (~18.5 and 21.0 Å in MUF-77-methyl) as the alkyl substituents lengthen. This is consistent with X-ray crystal structures that show that the alkyl substituent occupies this cavity.

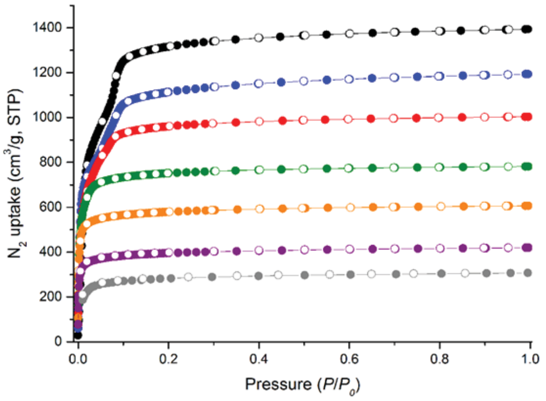

Figure 4.15 Nitrogen adsorption (filled circles) and desorption (open circles) isotherms at 77 K for MUF-7a and the MUF-77- series. Colour code: black: MUF-7a, blue: MUF-77-methyl, red: MUF-77-ethyl, green: MUF-77-butyl, orange: MUF-77-hexyl, purple: MUF-77-octyl and grey: MUF-77-decyl.

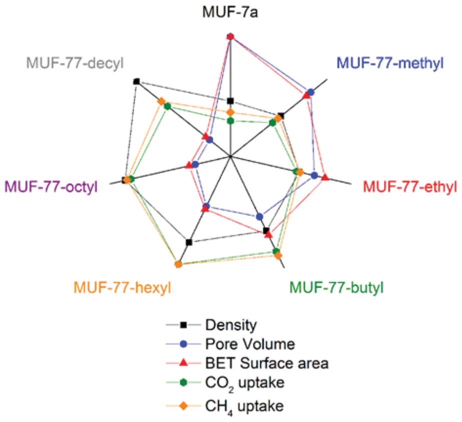

Figure 4.16 A plot showing the density, pore volume, surface area, volumetric CO_2 and CH_4 uptake at 1 atm and 273 K for MUF-7a and the MUF-77 series.

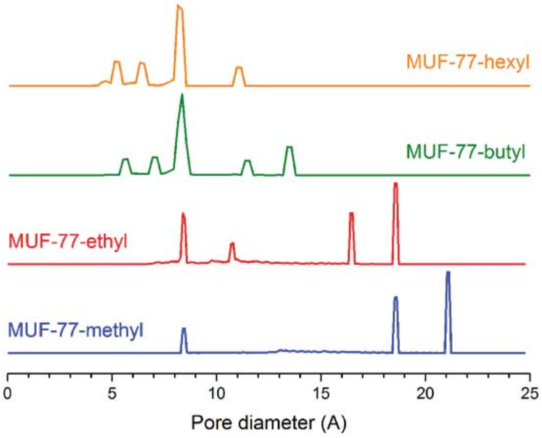

Figure 4.17 Pore size distributions for MUF-77-methyl, -ethyl -butyl and -hexyl calculated from their X-ray crystal structures.

4.2.4 Water stability of MUF-77 family

To test the influence of the length of the alkyl substituents on the stability of these frameworks towards atmospheric humidity, a series of gas and vapour adsorption isotherms were measured. The samples for these measurements were first activated then aged in air at a relative humidity of 40 – 50 % for three days and for 11 days. PXRD patterns were taken during the aging period and no changes could be discerned for any of these materials (Electronic Appendix B). N_2 (77 K) and CO_2 (273 K) isotherms were measured using the aged materials, and uptake capacities at 0.995 atm (N_2) and 1 atm (CO_2) were used as points of comparison with pristine specimens to determine the relative loss of porosity.

A counter-intuitive trend across the MUF-77 series emerges from the data presented in Figure 4.18. Frameworks with longer alkyl chains are *less stable towards water vapour*! Specifically, a cluster of frameworks with high stability comprises MUF-77-methyl, MUF-77-ethyl and MUF-77-butyl. Amongst this group, there are negligible changes in structure over the aging period. It is noteworthy that a 100 day aging experiment on MUF-77-butyl also resulted in minimal porosity loss (Figure 4.19). A second group of lesser stability contains MUF-77-hexyl, MUF-77-octyl and MUF-77-decyl. These MOFs lose about 25% of their capacity for adsorbing N_2 after 11 days of aging, and their CO_2 uptake capacity diminishes by around 17%. MUF-7 is the least stable of the frameworks under investigation.

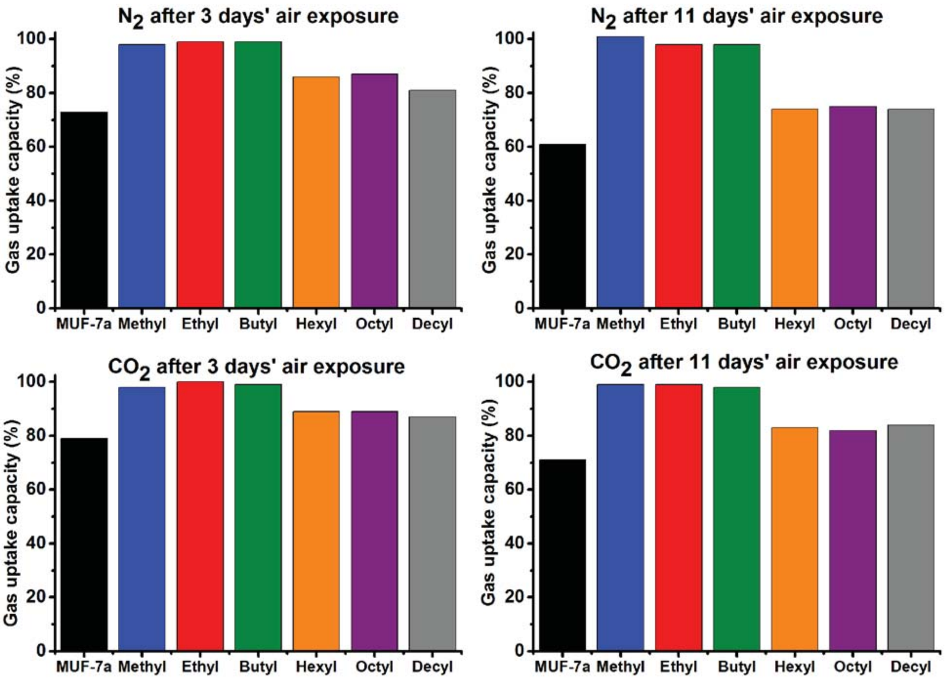

Figure 4.18 Relative porosities and CO_2 uptake capacities of aged MUF-77s and MUF-7a plotted as a fractional capacity with respect to the capacity of their pristine samples. N_2 isotherms measured at 77 K and CO_2 isotherms at 273 K.

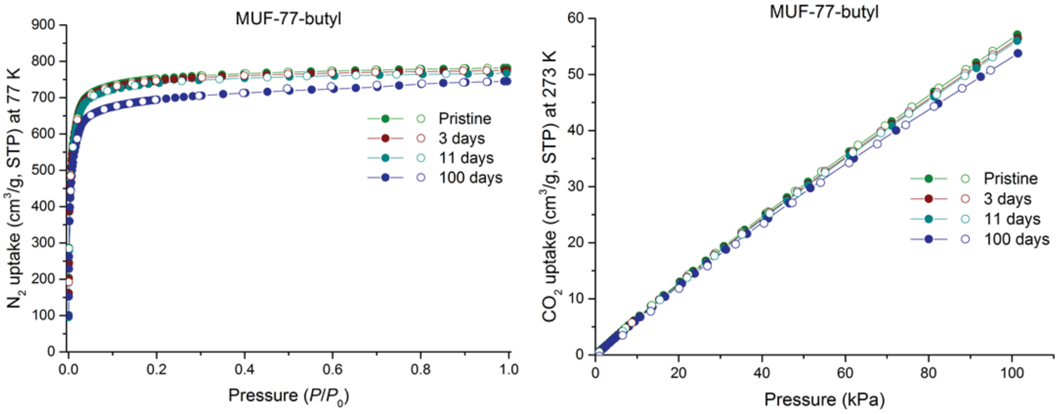

Figure 4.19 Left: Nitrogen adsorption (filled circles) and desorption (open circles) isotherms measured at 77 K for pristine and aged MUF-77-butyl under 40-50 % RH. Right: CO_2 adsorption (filled circles) and desorption (open circles) isotherms measured at 273 K for pristine and aged MUF-77-butyl under 40-50% RH.

A close inspection of experimental water adsorption isotherms[64,233] (Figure 4.20) together with Grand Canonical Monte Carlo (GCMC) simulations[197,234,235] provides insights into this surprising trend. The following observations are pertinent: (i) Water vapour uptake rises slowly as a function of the partial pressure at low RH, as expected for hydrophobic materials. (ii) In the isotherm region corresponding to the relative humidity of our aging experiments (40 - 50%), the concentration of water in the void space of the frameworks can be calculated by dividing the amount of excess water uptake (in mmol/g) by the measured pore volume of the MOF (in cm^3/g, Figure 4.20). The concentration of adsorbed water in the framework pores correlates with the length of the alkyl substituent on the truxene ligand; surprisingly, longer chains leads to higher water concentrations (Figure 4.20). (iii) The simulations provide information on the sites of water molecule adsorption. As shown in Figure 4.21 and Table 4.3, the frequency and relative probability of water molecules being adsorbed closer to Zn_4O SBUs increases with longer alkyl substituents.

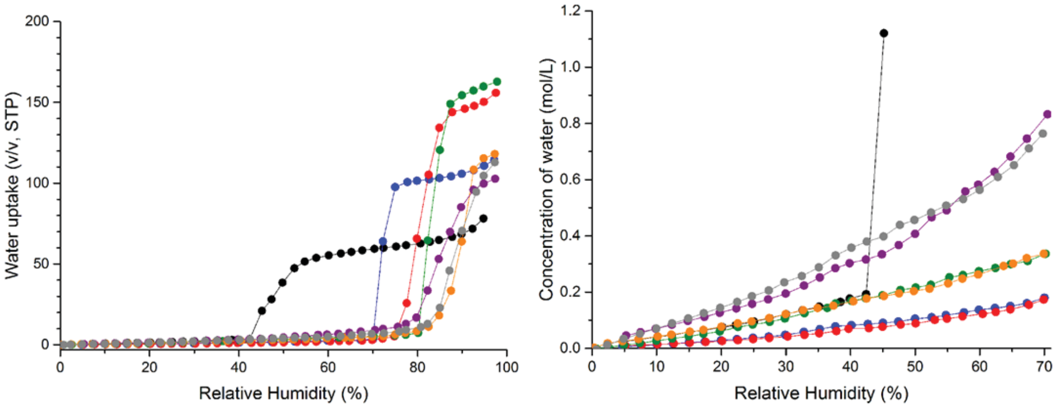

Figure 4.20 Left: Water vapour adsorption isotherms measured at 298 K for MUF-7a (black), MUF-77-methyl (blue), -ethyl (red), -butyl (green), -hexyl (orange), -octyl (purple) and -decyl (grey). Right: Adsorption isotherms presented to highlight the concentration of adsorbed water molecules in the framework void space as a function of RH.

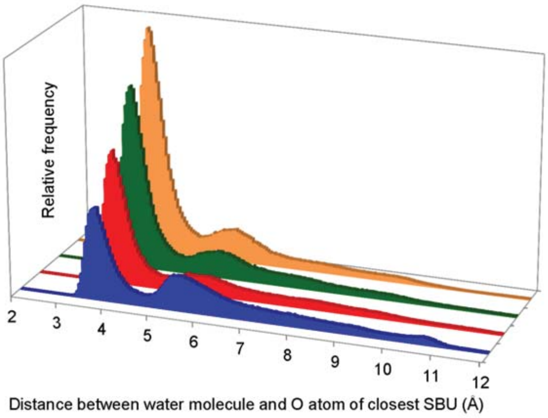

Figure 4.21 The distances between adsorbed water molecules and the closest Zn_4O SBU as calculated by GCMC simulations for MUF-77-methyl (blue), -ethyl (red), -butyl (green) and –hexyl (orange).

Table 4.3 Frequency and probability of water near Zn_4O SBUs in some MUF-77 materials.

MOF	Total frequency	Frequency for $0 < d_{\min} \leq 5$ Å	Probability for $0 < d_{\min} \leq 5$ Å
MUF-77-methyl	636629	281504	44.2%
MUF-77-ethyl	604884	384874	63.6%
MUF-77-butyl	793494	528802	66.6%
MUF-77-hexyl	930710	666636	71.6%

Table 4.4 Pore volume comparison for MUF-7a and MUF-77s calculated from N_2 and H_2O isotherms.

MOF	From N_2 isotherms at 77 K (cm^3/g)	From H_2O isotherms at 298 K (cm^3/g)
MUF-7a	2.16	0.162
MUF-77-methyl	1.85	0.127
MUF-77-ethyl	1.55	0.254
MUF-77-butyl	1.21	0.226
MUF-77-hexyl	1.00	0.142
MUF-77-octyl	0.65	0.110
MUF-77-decyl	0.48	0.108

MUF-77-ethyl was used for further water vapour sorption experiments where the RH was cycled multiple times between 10% and various maximum RH values (Figure 4.22). Material treated in this way was then analysed by PXRD, optical microscopy and a N_2 adsorption isotherm. After 20 cycles of water vapour adsorption and desorption to 70% RH, no visual changes to the MOF crystals were apparent (Figure 4.23). The PXRD pattern and N_2 isotherm were also identical to those of pristine specimens (Figure 4.23 and Figure 4.24). When MUF-77-ethyl was subject to 20 cycles to 75% RH, which lies at the beginning of the steep rise in water vapour uptake, we found the crystals turned almost opaque (Figure 4.23) and lost 40 % of their uptake capacity for N_2 (Figure 4.24). Their PXRD pattern, however, did not change, which reinforces the notion that PXRD alone is not adequate to determine whether a MOF is stable under certain conditions.[81,233] After only 3 cycles to 80% RH, which is at the halfway point of the steep rise, the crystals turned completely opaque (Figure 4.23) and the material lost most of its porosity (Figure 4.24).

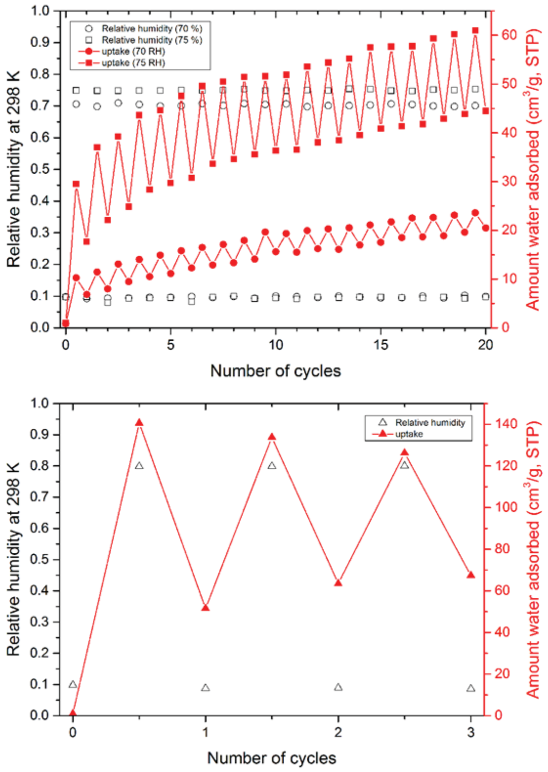

Figure 4.22 Top: Twenty water vapour adsorption and desorption isotherms for MUF-77-ethyl cycled between RH of 0.10 and either 0,70 or 0,75. Bottom: Three water vapour adsorption and desorption isotherms for MUF-77-ethyl cycled between RH of 0.10 and 0.80.

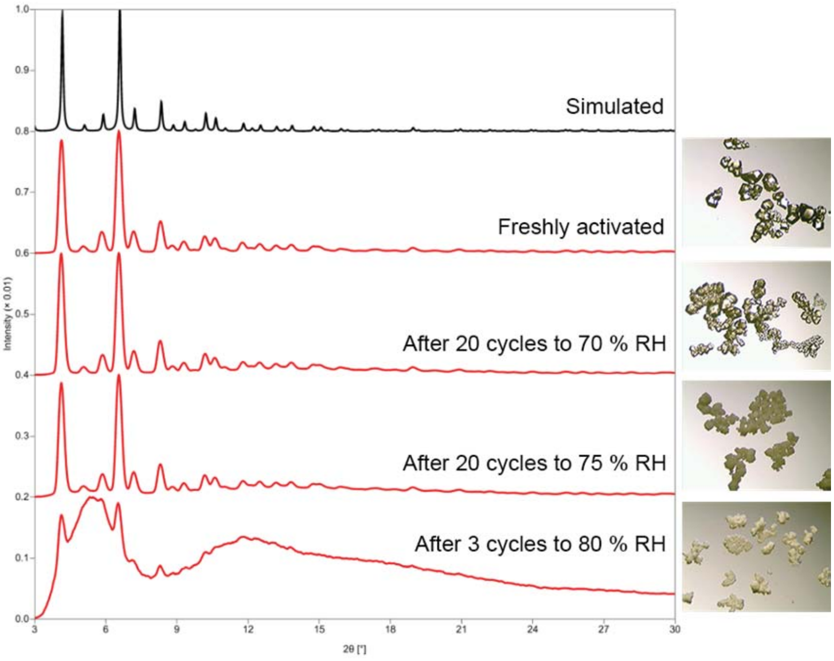

Figure 4.23 PXRD pattern of MUF-77-ethyl before and after water adsorption and desorption cycles between 10 % RH and different maximum humidity.

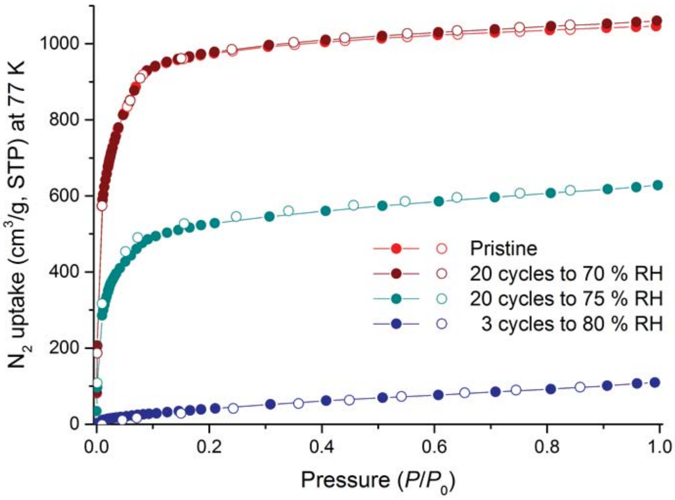

Figure 4.24 N_2 isotherms for MUF-77-ethyl measured at 77 K before and after water adsorption and desorption cycles between 10 % RH and different maximum humidity.

Several important findings emerge from the foregoing observations on water vapour uptake:

1. The contrasting stabilities of MUF-7a and MUF-77-methyl demonstrate that introducing truxene-based ligands in quaternary MOFs dramatically enhances their stability towards humidity. This arises from the truxene ligand, which confers a higher degree of hydrophobicity than btb. MUF-77-methyl therefore adsorbs less water vapour than MUF-77-methyl. The enhanced rigidity of the truxene ligand also plays a role by inhibiting the displacement of the ligands around the zinc clusters by incoming H_2O. We note that ligand rigidification has been found by other worker to enhance MOF stability towards shear forces.[94]

2. The steep rise of the water vapour uptake in the sorption isotherms corresponds to pore filling, which causes the degradation of the framework crystallinity and porosity (Figure 4.23). After pore filling occurs the water sorption is largely irreversible, presumably because of chemisorption to the components of the collapsed frameworks.

3. The stable group of materials, MUF-77-methyl, -ethyl, and -butyl, can be used, handled, or stored at up to 70 % RH over long periods of time. We ascribe this to their relatively low affinity for water vapour, as evidenced by their water vapour sorption isotherms.

4. The instability of the MUF-77 materials with longer alkyl substituents under ambient conditions is due to a combination of a high concentration of water in their void volumes at relevant RHs and the close proximity of the adsorbed water molecules to the Zn_4O clusters.

These factors promote hydrolysis of the zinc(II) clusters leading to framework collapse.[236] This underlies the counterintuitive relationship between ligand hydrophobicity and MOF stability.

Valuable trends in CO_2 and CH_4 adsorption capacities emerge from adsorption isotherms measured for these gases across the MUF-77 series. Volumetric uptake of CO_2 and CH_4 peaks at MUF-77-hexyl (Figure 4.25). Increases of 237 % and 172 % are observed for CO_2 and CH_4, respectively, with respect to MUF-7a. These increases are achieved simply by modifying the pores with space-filling alkyl chains rather than the conventional approach of introducing polar functional groups or open metal sites.[159,161] Related observations have been made in other studies.[191,237-239] We can understand the trends exhibited by the MUF-77 series by analysis of the isosteric heats of adsorption, which increase as the alkyl chain becomes longer (Table 4.2, Figure 4.26), and the available pore volume, which naturally decreases with increasing substituent size. MUF-77-hexyl represents the point at which an optimum combination of heat of adsorption and pore volume is reached. MOFs with shorter alkyl chains feature open pores, which provide relatively few favourable noncovalent interactions between the framework walls and gas molecules. Alkyl chains of intermediate length (e.g., butyl, hexyl) are ideal in that they induce pore topographies with significant nooks and crannies that maximize the number of favourable noncovalent interactions with guest molecules. Overly long alkyl chains, on the other hand, overfill the pores and render them featureless and smaller than optimal, which limits the number of guest molecules that can be bound.

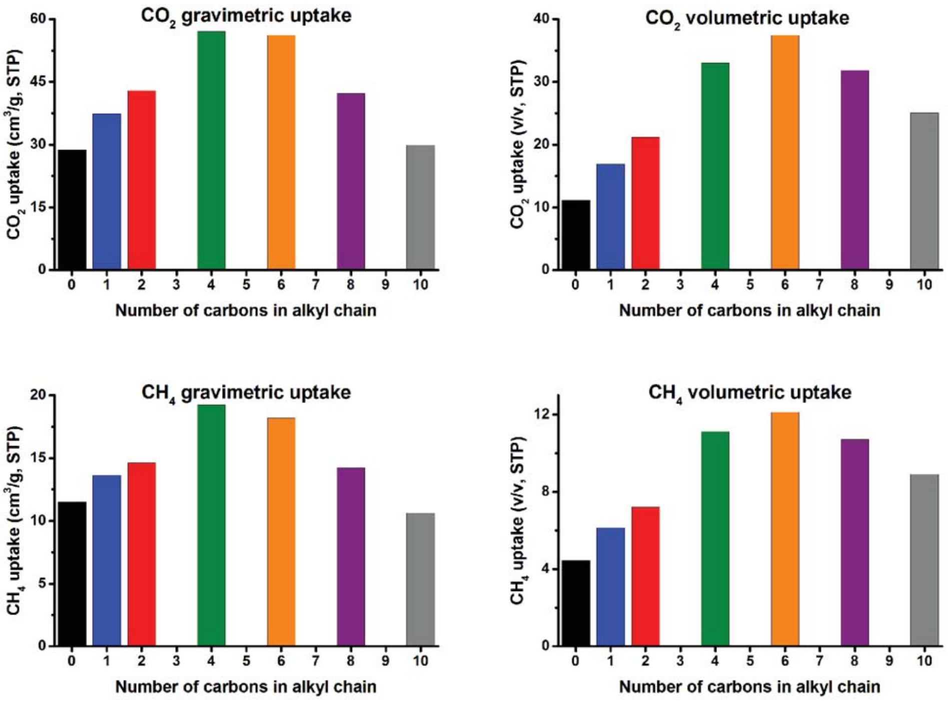

Figure 4.25 Gravimetric (left) and volumetric (right) gas adsorption capacities for CO_2 (top) and CH_4 (bottom) taken from adsorption isotherms at 1 atm and 273 K for MUF-7a (black), MUF-77-methyl (blue), -ethyl (red), -butyl (green), -hexyl (orange), -octyl (purple) and -decyl (grey).

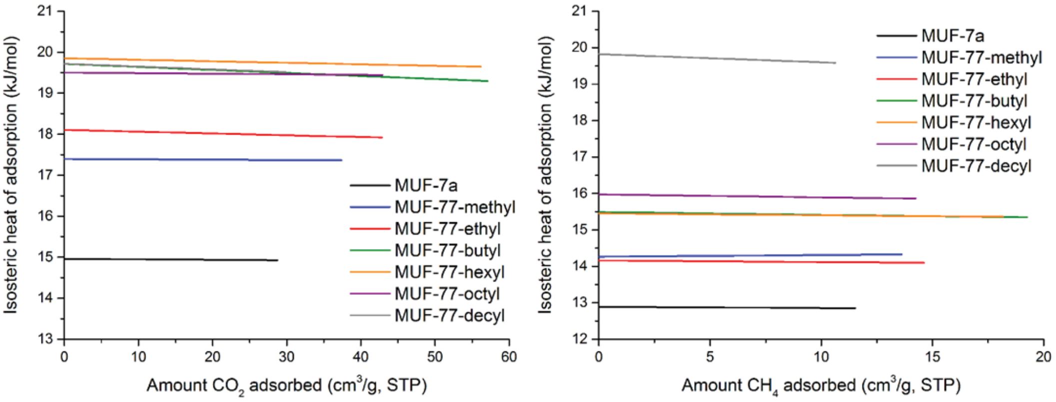

Figure 4.26 Isosteric heat of adsorption plots for the adsorption of CO_2 (left) and CH_4 (right) by MUF-7a and MUF-77s.

4.3 Conclusion

The synthesis of an isoreticular family of quaternary Zn_4O carboxylate MOFs with a series of truxene-based tritopic linkers generates unique insights into the ways in which MOF characteristics can be systematically optimized. The planarity of truxene ligand inhibits the formation of competing phases, allowing reactions involving large ligand sets to converge on the desired multicomponent frameworks. The rigidity and hydrophobicity of the truxene moiety also enhances the stability of these MOFs towards water vapour to the point where several of these materials can be openly handled in standard laboratory environments over a time period of at least several months. By modulating the substituents on the truxene ligands, we made the surprising discovery that members of this series with long alkyl chains are less stable toward ambient humidity. Water adsorption isotherms combined with GCMC simulations revealed that this counter-intuitive finding can be rationalized by an increased concentration of water in the framework pores at low RH and the propensity for this adsorbed water to reside close to the Zn_4O SBUs. Systematic ligand modulation also resulted in tunable CO_2 and CH_4 adsorption characteristics. The CO_2 uptake for the best performing material is more than treble that of its non-functionalized analogue.

These insights are enabled by the multicomponent nature of the MUF-77 series. A selected ligand, in this case the tritopic truxene liker, can be appended with substituents that systematically modify the pore characteristics. Such modifications would typically lead to low porosity and a breakdown in the isoreticular relationship for MOFs that comprise just one ligand. A key advantage of multicomponent MOFs is that − collectively − ligand sets are able to maintain the open structure of parent frameworks even if significant changes are made to one of their members. This enables enlightening relationships between ligand structures, pore characteristics, and functional performance to be established. The modification of all three linkers to produce variants of MUF-77 with programmed pores is an exciting prospect.

4.4 Experimental section

4.4.1 General procedures

All starting compounds and solvents were used as received from commercial sources without further purification unless otherwise noted. Truxene[240] and 5,5′,10,10′,15,15′-hexaethyltruxene[225] were prepared via literature procedures. Column chromatography was carried out on silica gel (grade 60, mesh size 230-400, Scharlau). NMR spectra were recorded at room temperature (unless otherwise noted) on Bruker-400 and Bruker-500 Avance instruments, with the use of the solvent proton as an internal standard. Elemental analyses were performed by the Campbell Microanalytical Laboratory at the University of Otago, New Zealand.

4.4.2 Ligand synthesis and characterization

All truxene-based ligands were synthesized starting from truxene according to Scheme 4.1. Detailed procedures and spectroscopic data on these ligands and their intermediates are available in the Electronic Appendix B.

H_3hbtt: ^{1}H NMR (500 MHz, DMSO-d_6): δ 0.33 – 0.48 (m, 30H), 0.80 (m, 12H), 2.20 (m, 6H), 3.00 (m, 6H), 8.04 (d, J = 8.3 Hz, 3H), 8.08 (s, 3H), 8.44 (d, J = 8.3 Hz, 3H) ppm. ^{13}C NMR (125 MHz, DMSO-d_6): δ 13.63, 22.15, 26.30, 35.56, 55.49, 123.10, 124.43, 128.25, 129.22, 137.67, 143.36, 147.15, 153.11, 167.41 ppm. ES-MS (positive mode): m/z = 811.49 ($[C_{54}H_{67}O_6]^+$, calcd. 811.49). Anal. calcd. for $[C_{54}H_{66}O_6]$: C, 79.96; H, 8.20; Found: C, 79.72; H, 8.23.

H_3hhtt: ^{1}H NMR (400 MHz, DMSO-d_6): δ 0.37 (m, 12H), 0.50 (t, J = 6.6 Hz, 18H), 0.70-0.91 (m, 36H), 2.18 (m, 6H), 2.98 (m, 6H), 8.08 (d, J = 8.3 Hz, 3H), 8.11 (s, 3H), 8.48 (d, J = 8.3 Hz, 3H), 13.04 (m, br, 3H) ppm. ^{13}C NMR (100 MHz, DMSO-d_6): δ 13.59, 21.49, 23.44, 28.64, 30.89, 35.90, 55.57, 122.99, 124.33, 128.22, 129.19, 137.62, 143.37, 146.97, 153.06, 167.48 ppm. ES-MS (positive mode): m/z = 979.68 ($[C_{66}H_{91}O_6]^+$, calcd. 979.68). Anal. calcd. for $[C_{66}H_{90}O_6]\cdot 0.5\ H_2O$: C, 80.20; H, 9.28; Found: C, 80.07; H, 9.38.

H3hott: ^{1}H NMR (500 MHz, DMSO-d_6, 40 °C): δ 0.39 (m, 12H), 0.63 (t, J = 6.9 Hz, 18H), 0.76-0.96 (m, 60H), 2.17 (m, 6H), 2.98 (m, 6H), 8.07 (d, J = 8.2 Hz, 3H), 8.10 (s, 3H), 8.48 (d, J = 8.2 Hz, 3H) ppm. ^{13}C NMR (125 MHz, DMSO-d_6, 40 °C): δ 13.53, 21.66, 23.27, 28.03, 28.37, 28.77, 31.02, 35.76, 55.42, 122.87, 124.11, 128.02, 129.16, 137.54, 143.25, 146.83, 152.93, 167.27 ppm. Anal. calcd. for [$C_{78}H_{114}O_6$]·0.5 H_2O: C, 80.99; H, 10.02; Found: C, 81.02; H, 10.16.

H_3hdtt: ^{1}H NMR (500 MHz, DMSO-*d*$_6$, 80 °C): δ 0.45 (m, 12H), 0.73-1.14 (m, 102H), 2.20 (m, 6H), 2.97 (m, 6H), 8.06 (d, *J* = 8.2 Hz, 3H), 8.10 (s, 3H), 8.46 (d, *J* = 8.3 Hz, 3H) ppm. ^{13}C NMR (125 MHz, DMSO-*d*$_6$, 80 °C): δ 13.15, 21.41, 23.05, 27.97, 28.08, 28.38, 28.50, 30.71, 35.69, 55.23, 122.65, 123.74, 127.61, 129.06, 137.35, 142.97, 146.62, 152.70, 166.87 ppm. Anal. calcd. for [$C_{90}H_{138}O_6$]: C, 82.14; H, 10.57; Found: C, 82.08; H, 10.77.

4.4.3 MOF synthesis and characterization

In general, three ligands and zinc nitrate tetrahydrate were dissolved or well-suspended in DEF and H_2O (3-5% v/v) in a scintillation vial which had been pretreated with Sigmacote. The vial was heated to 85 °C for various period of time and allowed to cool naturally. This yields crystals of the MUF-77 series. To scale up the synthesis, a similar reagent ratio was used and scaled up accordingly. Reactions were carried out in Schott bottles with various amounts of solvents. Detailed procedures and characterization data (^{1}H NMR spectra, optical microscopy images and elemental analyses) of the MUF-77 family are available in Electronic Appendix B.

4.4.4 ^{1}H NMR analysis of digested MOF samples

For ^{1}H NMR spectroscopy, the mother liquor of the as-synthesized MOF crystals was replaced with fresh dry DMF multiple times. The MOF crystals were then filtered through a Büchner funnel on a filter paper under suction and the surfaces of the crystals were allowed to dry. The crystals were then digested using the following protocol: 23 μL of a 35% DCl solution in D_2O was mixed with 1 mL of DMSO-*d*$_6$ to give a DCl/DMSO-*d*$_6$ stock solution. Around 5 mg of MOF was digested in 150 μL of this stock solution together with 450 μL of DMSO-*d*$_6$. Spectra were acquired immediately following dissolution. Spectra for all MOFs are presented in Electronic Appendix B.

4.4.5 Thermogravimetric analysis (TGA)

Thermogravimetric analyses were performed on a TA Instruments Q50 instrument. Measurements were made under a N_2 flow with a heating rate of 5 °C /min.

TGA of DMF-solvated MOFs: The mother liquor of the as-synthesized MOF crystals was replaced with fresh dry DMF multiple times. The MOF crystals were then filtered through a Büchner funnel on filter paper under suction and the surfaces of the crystals were allowed to dry.

TGA of desolvated MOFs: The mother liquor of the as-synthesized MOF crystals was replaced with fresh dry DMF multiple times. The MOF crystals were then soaked in DMF overnight. The solvent was then replaced with fresh dry dichloromethane multiple times. The MOF crystals were then soaked in dichloromethane overnight. The MOF crystals were then evacuated under high vacuum to afford desolvated MOFs.

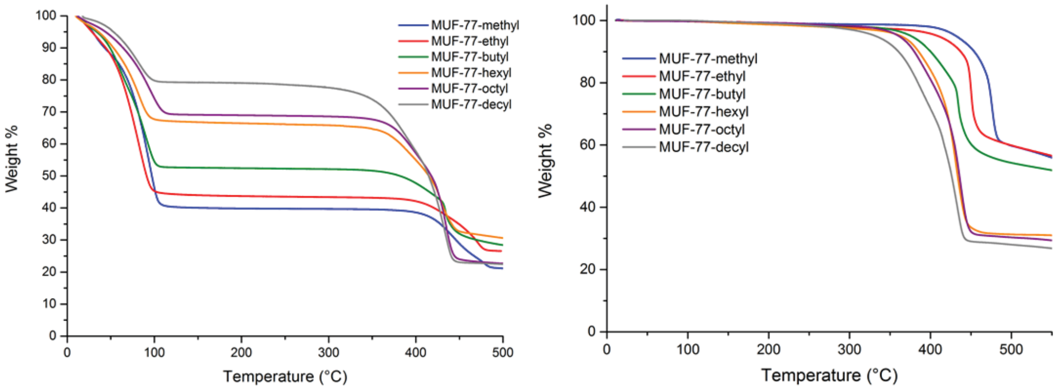

Figure 4.27 Thermogravimetric analysis (TGA) traces of DMF solvated (left) and desolvated(right) MOFs

4.4.6 Single crystal X-ray diffraction

Data collections were performed on a Rigaku Spider diffractometer equipped with a MicroMax MM007 rotating anode generator (Cu$_{\alpha}$ radiation, 1.54180 Å), high-flux Osmic multilayer mirror optics, and a curved image-plate detector. Data were integrated and scaled and averaged with FS Process.[203] XPREP[204] was used to determine the space group and the structures were solved using direct method under SHELXS[204] and refined with SHELXL[204] under an Olex 2[241] graphical interface. Crystallography of MOFs will be described here, whereas crystallography of 2,7,12-triacetyl-5,5′,10,10′,15,15′-hexaoctyltruxene is detailed in Electronic Appendix B.

As-synthesized MOF crystals were soaked in fresh dry DMF and DMF was replenished few times within a day. The crystals were soaked overnight then the solvent was exchanged with dry dichloromethane and dichloromethane was again replenished several times. The crystals were soaked in dry dichloromethane overnight before being activated in a vacuum oven (0.5 Torr) at 80 °C overnight. The vacuum oven was back filled with humid air (~70 % relative humidity) to produce crystals suitable for single crystal X-ray diffraction analyses.

MOF crystals were analyzed within a few days of activation, except for MUF-77-ethyl, which was aged at 40 - 50% relative humidity at 20 °C for 35 days before being analyzed.

All data were collected at 293 K. It is noteworthy that the data quality of these activated crystals is better than that of the crystals in their solvated form. Room temperature data collection also produced better refinement statistics than low temperature data collection.

All zinc, oxygen and non-alkyl carbon atoms were found in the electron density difference maps and refined anisotropically. All hydrogen atoms were calculated and refined as a riding model. The treatment of the atoms of the alkyl chains is described below.

MUF-77-methyl and MUF-77-ethyl

All alkyl carbon atoms were found in the electron density difference map and refined anisotropically.

MUF-77-butyl

All eight carbons atoms of the two butyl groups were found in the electron density difference map. The four carbon atoms which are least distant from the truxene core were refined anisotropically and the rest of the carbon atoms were refined isotropically. One terminal carbon atom of a butyl group was found to be disordered over two sites. The occupancies of these two possible locations were refined freely but sum up to one. The same atomic displacement parameters were used for these two locations. Some distance restraints were used when appropriate.

MUF-77-hexyl

Six out of twelve carbon atoms of the two hexyl groups were found in the electron density difference map. All other carbon atoms are disordered and were not modeled. The two terminal carbon atoms were refined isotropically (with a displacement parameter fixed to 1.2 times that of the adjacent carbon atom) and the remaining alkyl carbon atoms were refined anisotropically. SQUEEZE[227] found that there are 762 unallocated electrons which compares with the 1152 electrons of unmodeled carbon and hydrogen atoms.

MUF-77-octyl

Six out of sixteen carbon atoms of the two octyl groups were found in the electron density difference map. All other carbon atoms are disordered and were not modeled. The four terminal carbon atoms were refined isotropically (with a displacement parameter fixed to 1.2 times that of the adjacent carbon atom) and the remaining alkyl carbon atoms were refined anisotropically. Two distance restraints were used. SQUEEZE found that there are

1103 unallocated electrons which compares with 1920 electrons of unmodeled carbon and hydrogen atoms.

MUF-77-decyl

Six out of twenty carbon atoms of the two decyl groups were found in the electron density difference map. All other carbon atoms are disordered and cannot be located. Thus these carbon atoms are not modeled. The four terminal carbon atoms were refined isotropically and the remaining alkyl carbon atoms were refined anisotropically. Two distance restraints were used. The same atomic displacement parameters were used for the two β carbons atoms. SQUEEZE found that there are 1719 unallocated electrons which compares with 2688 electrons of unmodeled carbon and hydrogen atoms.

4.4.7 Powder x-ray diffraction patterns

All powder X-ray diffraction experiments were carried out on a Rigaku Spider X-ray diffractometer with Cu K_α radiation (Rigaku MM007 microfocus rotating-anode generator), monochromated and focused with high-flux Osmic multilayer mirror optics, and a curved image plate detector. The data were obtained from either freshly prepared MOF samples that had been ground into slurry in a small amount of DEF and kept damp with DEF throughout the measurement, or desolvated MOF samples (prepared in the same way as the samples of the single crystal X-ray experiments) that were ground then fixed to a mount with a minimum amount of Fomblin oil. The two-dimensional images of the Debye rings were integrated with 2DP[242] to give 2θ vs I diffractograms. The predicted powder patterns of the MOFs were generated from their single-crystal structures using Mercury v3.3.

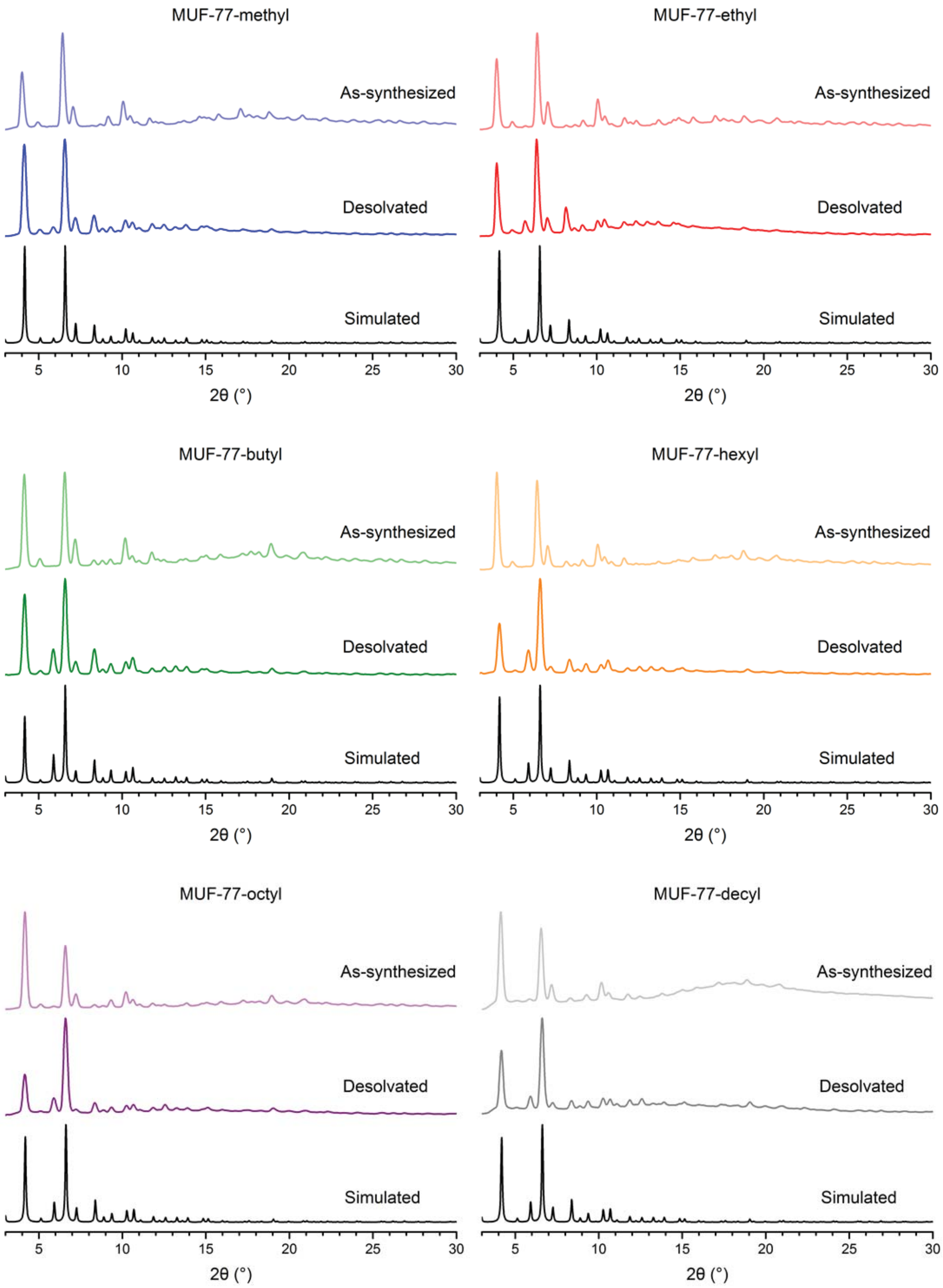

Figure 4.28 Simulated and experimental PXRD patterns of MUF-77 series.

4.4.8 Gas adsorption measurements and calculations

Low pressure gas adsorption isotherms were measured by a volumetric method using a Quantachrome Autosorb iQ2 instrument. Freshly prepared MOF samples were washed with DMF then activated by soaking in dry CH_2Cl_2 for several days then transferred to a pre-dried and weighed analysis tube. Excess CH_2Cl_2 was removed under vacuum and the tube back filled with argon before being heated at 1 °C per minute to 80 °C under vacuum. The sample was then held under a dynamic vacuum at 10^{-6} Torr for 10 hours. Accurate sample masses were calculated using degassed samples after sample tubes were backfilled with nitrogen. All sorption measurements used ultra-high purity gases. Isotherms can be found in Electronic Appendix B and additional isotherm fitting figures and data are available in Electronic Appendix D.

4.4.9 Aging experiments on activated frameworks

Activated MOF samples were aged in air at 40-50% relative humidity and 20 °C. Microscopy images, powder X-ray diffraction patterns and gas sorption measurements were conducted on pristine and aged samples. Most of the aging experiments were performed on samples directly after gas adsorption measurements except for two specimens: MUF-77-ethyl and MUF-77-butyl, which were prepared separately by heating CH_2Cl_2-solvated samples in a vacuum oven (3.5 mbar) to 80 °C overnight. Aged samples were evacuated to 10^{-6} Torr at 20 °C for 5 hours prior to the gas adsorption measurements. PXRD patterns and Gas adsorption data pre- and post-aging are detailed in Electronic Appendix B.

4.4.10 Water vapour sorption measurements

Water adsorption isotherms were measured by a volumetric method using a Quantachrome Autosorb iQ2 instrument. Deionized water was degassed at 3.5 Torr for 2 hours before being used. Freshly prepared MOF samples were washed with DMF then activated by soaking in dry CH_2Cl_2 for several days, transferred to a pre-dried and weighed analysis tube. Excess CH_2Cl_2 was removed under vacuum and back filled with argon before the sample was heated at 1 °C per minute to 80 °C under vacuum then held under a dynamic vacuum at 10^{-6} Torr for 10 hours. Accurate sample masses were calculated using degassed samples after backfilling with nitrogen. Water adsorption and desorption data for MUF-7a and MUF-77 series are detailed in Electronic Appendix B.

4.4.11 Modeling, calculations and simulations

MOF models

Single crystal structures of MUF-77-methyl and MUF-77-ethyl were used directly for all the calculations and simulations without modification. For MUF-77-butyl, most of its atomic coordinates were taken from the single crystal structure except that one disordered carbon atom and its related hydrogen atoms were deleted. Chemically reasonable locations for the missing carbon and hydrogen atoms were added to generate a model for MUF-77-hexyl, and the positions of these generated atoms were optimized by using CHARMm force field using the Discovery Studio 3.5 software pack.[243]

Geometric surface area calculations

The geometric surface areas of the frameworks were calculated by the method described by Düren et al.[194] This involves rolling a spherical probe, with diameter was set to the van der Waals diameter of N_2 (3.72 Å),[244] over the framework atoms. The diameters of the framework atoms were also set to their van der Waals diameters which were calculated by multiplying their Lennard-Jones well-depth diameters, σ, by $2^{1/6}$. The σ values of all framework atoms were taken from the DREIDING force field.[208] The results are listed in Table 4.5.

Table 4.5 Some calculated and experimentally determined results for selected MUF-77s.

MUF-77	-methyl	-ethyl	-butyl	-hexyl
BET surface area (m^2/g)	3600	3600	3250	2170
Geometric surface area (m^2/g)	4031	3836	3120	1787
Pore volume (cm^3/g, from experimental N_2 isotherm)	1.85	1.55	1.21	1.00
Pore volume (PLATON)	1.74	1.52	1.16[a]	No data[b]
Pore volume (helium insertion method)	1.88	1.60	1.20	0.89
Maximum pore diameter (Å)	21.1	18.5	13.6	11.2
Pore limiting diameter (Å)	7.1	6.5	5.7	4.4

a) Based on a model where only one orientation of disordered component is considered. b) Not calculated because some carbon and hydrogen atoms are not found on the electron density difference map.

Theoretical pore volume calculations

Theoretical pore volumes were calculated by PLATON[227] and the helium insertion method.[195] Results from both methods are listed in Table 4.5.

Maximum pore diameter, free pore diameter and pore size distributions

The maximum pore diameters, free pore diameters and pore size distributions of MOFs were calculated using Poreblazer v3.0.2.[226] A cubelet size of 0.2 Å was employed. The results are listed in Table 4.5.

Water vapor adsorption simulations

The locations of water molecules adsorbed in the MOFs were predicted using the grand canonical Monte Carlo (GCMC) simulation method described by Snurr et al.[234] The Lennard-Jones parameters for all framework atoms were taken from the DREIDING force field, which are listed in Table 4.6. Partial charges of the framework atoms were calculated with the EQeq method.[245] The TIP4P force field was used to describe water molecules, in which case the negative charge is moved off the oxygen atom by 0.15 Å and towards the hydrogen atoms.[246] This charge is applied to a dummy atom (M) which is located on the bisector of the HOH angle. The oxygen-hydrogen bond length is 0.9572 Å and the HOH angle is 104.52° according to this force field.

Simulations were performed using the RASPA software package.[197] The water vapor pressure used for all the simulations at 50 % RH and 298 K is 1585 Pa. Three GCMC moves were used with unequal probability as detailed in the original paper.[234] After one million initialization cycles, five million cycles of GCMC moves were performed and the coordinates for all adsorbed water molecules were recorded. The distances between these water oxygen atoms and all 12 Zn_4O cluster oxygen atoms in a MOF unit cell were calculated. The shortest distances were used to calculate the distance distribution plots presented in the main manuscript.

Table 4.6 Lennard-Jones parameters and partial charges for MOF and water atoms.

Atom Type	σ (Å)	ε / k_B (K)	Charge method or value (e)
Zn (MOF)	4.045	27.677	EQeq
O (MOF)	3.033	48.158	EQeq
C (MOF)	3.473	47.856	EQeq
H (MOF)	2.846	7.649	EQeq
O (H_2O)	3.154	78.0	0
H (H_2O)	0	0	0.52
M (H_2O)	0	0	-1.04

Chapter 5

Catalysis by Multicomponent Metal-Organic Frameworks

5.1 Introduction

Catalysis is a vital part of both fundamental and applied chemistry. One great advantage of using heterogeneous catalysts is the facile separation of the product and the catalyst. However, solid heterogeneous catalysts have their own disadvantages. One significant disadvantage is that a solid has very low relative surface area that is exposed to the reactants.[247] This prevents most of the catalyst from getting involved in the reaction. The exceptionally high surface area, and high thermal and chemical stability of MOFs make them ideal heterogeneous catalysts.[57,73,248,249] In the past decade, rapid advances have been made in the field of MOF catalysis.[30,72,85,132,152,185,250-258]

A compelling advantage of multicomponent MOFs over other MOF catalysts is that, as demonstrated by the MUF-7 and MUF-77 families of materials, pockets with a precise three-dimensional array of pre-selected functional groups can be created. To create analogues that are catalytically-active, these pockets might be designed to feature *activation sites* that bind and preorganize substrates by covalent or H-bonding to initiate a reaction, and *modulator sites* that may influence the reaction rate and product selectivity via noncovalent interactions.[259,260] The design of linkers with activation and modulator sites can be guided by small-molecule catalysts, supramolecular catalysts and enzymes.[261-264] Stereoselectivity can potentially be induced by either the activation site (a chiral catalytically-active functional group) or by a chiral modulator group. By fabricating broad families of catalytically-active multicomponent MOFs with pockets that are varied systematically, turnover frequencies and stereoselectivities might be able to be optimised. In this way, catalysis by multicomponent MOFs could have parallels with enzymes in that catalytic activity stems from a well-ordered array of functional groups in a compartment that can be engineered by a kind of "site-directed mutagenesis".[260,265]

5.2 Results and discussion

5.2.1 Synthesis and characterization of a MUF-77 catalyst

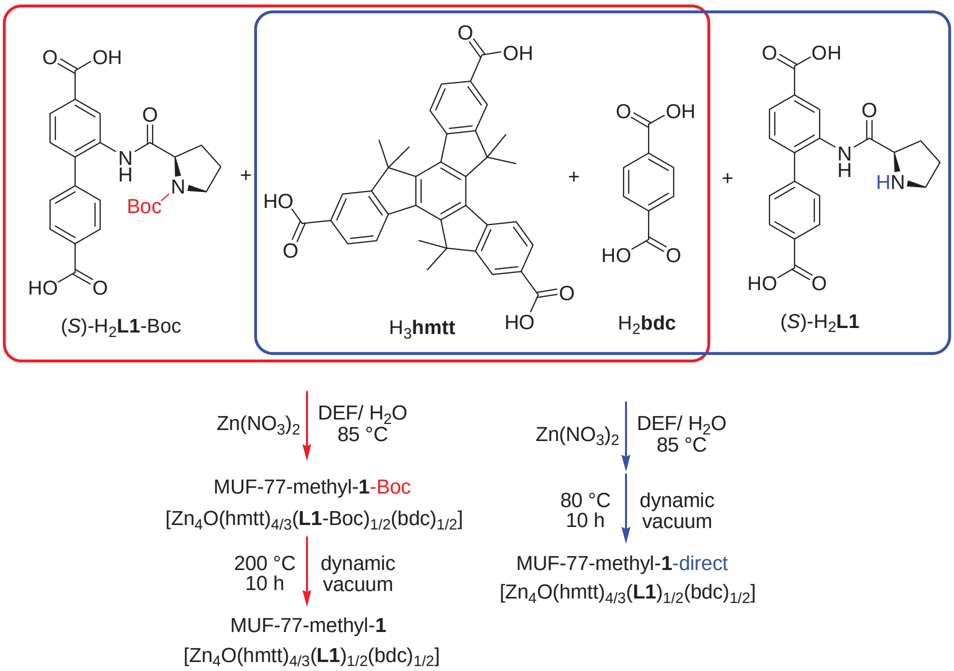

Scheme 5.1 Synthetic route to MUF-77-methyl-**1**-Boc and MUF-77-methyl-**1**. The latter can be prepared by thermolysis of MUF-77-methyl-**1**-Boc (red arrows) or by direct synthesis (blue arrows).

We targeted the synthesis of a MUF-77 variant that bears a chiral, enantiopure, catalytically-active proline unit[1] attached to the bpdc ligand. The two routes to this MOF are shown in Scheme 5.1. In the first route (red arrows) the thermolabile protecting group strategy that has previously been developed earlier by our group[1,32,33] was employed. This involves first installing a *tert*-butoxycarbonyl (Boc) protected proline group, which prevents the amino functionality from interfering with MOF synthesis, to produce a precursor framework. Post-synthetic deprotection by simple heating releases the Boc group as CO_2 and isobutylene, which escape from the framework. The second route to a proline derivative of MUF-77 is shown with blue arrows. Here, an unprotected proline substituent is present on the bpdc ligand and the MOF is synthesized directly.

The first route was implemented by the solvothermal reaction of H_3hmtt, (*S*)-H_2**L1**-Boc,[1] H_2bdc and zinc nitrate in DEF. This produced only one type of well-faceted, colourless crystals. Similar to other members of the MUF-7 and MUF-77 families, the crystals are fully extinguished at all rotational positions under crossed polarisers on an optical microscope, indicating that they belong to a cubic crystal system. The powder X-ray diffraction pattern of these crystals, following activation by desolvation, is almost identical to MUF-77-methyl indicating that it is isoreticular to MUF-77 (Figure 5.1a). An ^{1}H NMR spectrum of a digested sample shows a ratio of 8:3:3 of the three ligands (Figure 5.2). These experiments confirm the formula, structure, and phase-purity of this new MOF, MUF-77-methyl-**1**-Boc.

Following the second route, a solvothermal reaction of H$_3$hmtt, (*S*)-H$_2$**L1**, bdc and zinc nitrate produced MUF-77-methyl-**1**-direct, as evidenced from single-crystal X-ray analysis. However, later experiments showed that this MOF was catalytically inactive, thus to produce a catalytically-active MOF catalyst we focused on the first route.

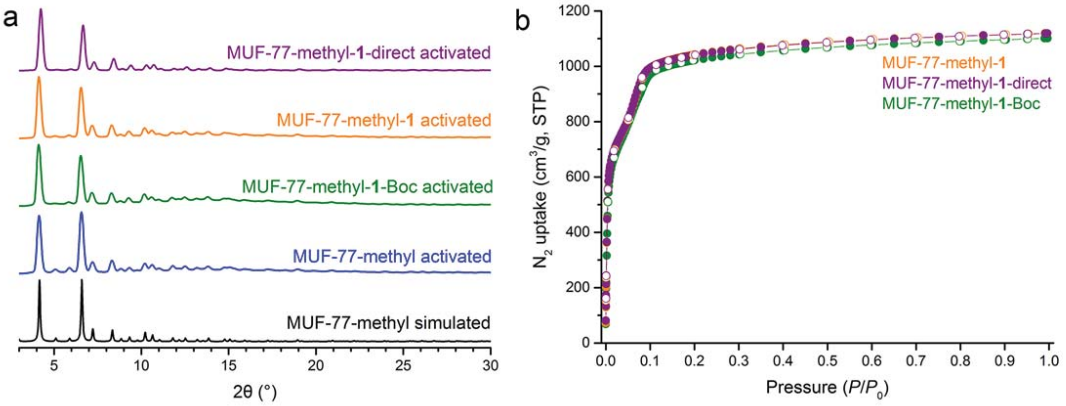

Figure 5.1 a) Simulated MUF-77-methyl PXRD pattern and experimental PXRD patterns of MUF-77-methyl, MUF-77-methyl-**1**-Boc and MUF-77-methyl-**1**. b) Nitrogen adsorption isotherms of MUF-77-methyl-**1**-Boc, MUF-77-methyl-**1** and MUF-77-methyl-**1**-direct measured at 77 K.

To reveal the catalytically-active proline sites, MUF-77-methyl-**1**-Boc was thermolyzed at 200 °C for 10 hours under a dynamic vacuum. This process successfully removed the Boc protecting group, as evidenced by ^{1}H NMR spectroscopy of digested MOF crystals: the two peaks at 1.33 and 1.35 ppm, which correspond to the *tert*-butyl groups of the two conformers of (*S*)-H$_2$**L1**-Boc in solution, disappear (Figure 5.2). The crystallinity of MUF-77-methyl-**1** is maintained after thermolysis since its PXRD pattern is almost identical to MUF-77-methyl-**1**-Boc (Figure 5.1a). The porosity and surface area of MUF-77-methyl-**1** is also unchanged after thermolysis, as indicated by the similarity of the N$_2$ adsorption isotherms measured at 77 K for the two frameworks (Figure 5.1b).

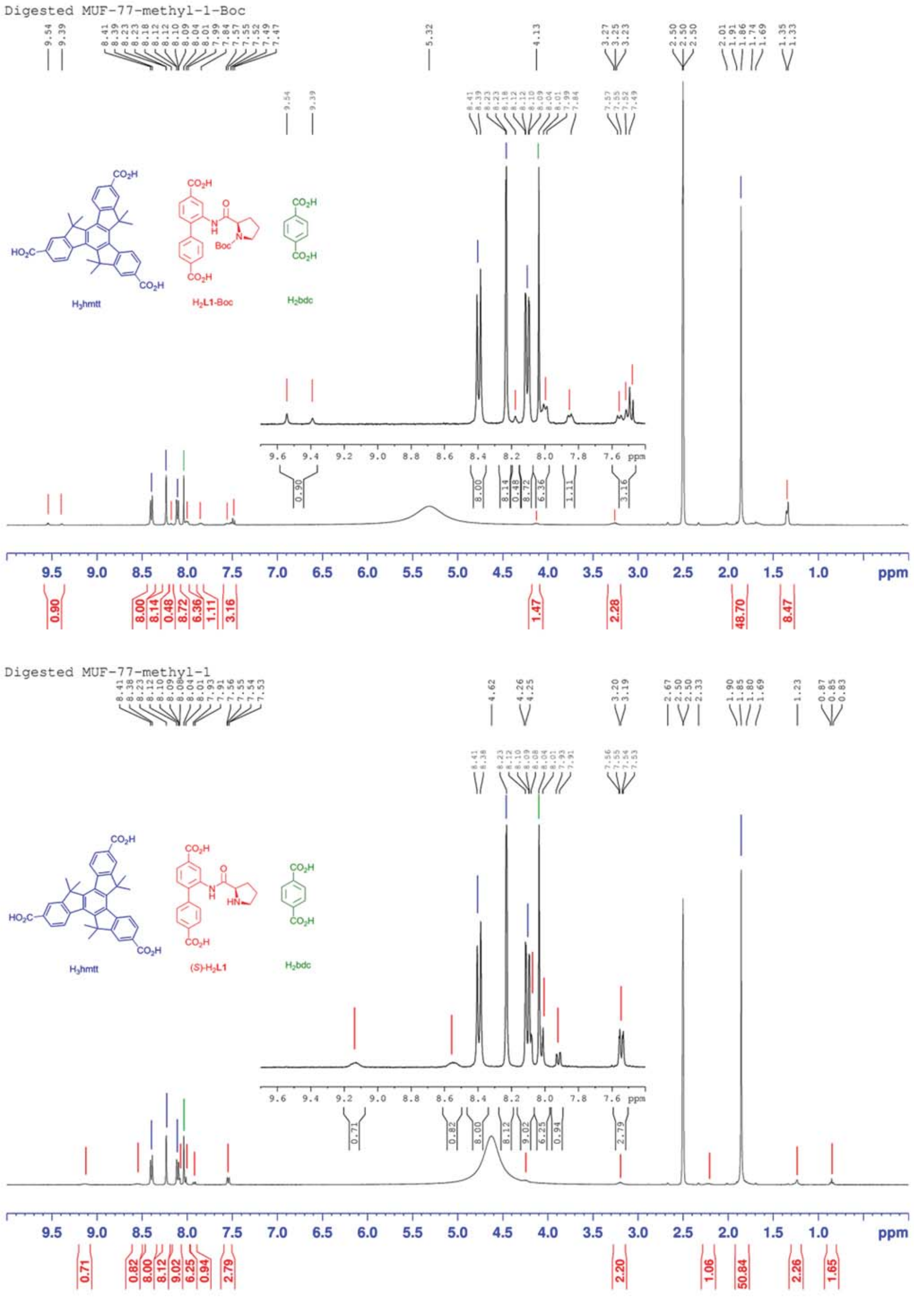

Figure 5.2 Upper: ^{1}H NMR spectra of digested MUF-77-methyl-**1**-Boc showing the integrals that match with the formula [$Zn_4O(hmtt)_{4/3}$(**L1**-Boc)$_{1/2}$(bdc)$_{1/2}$]. Note that two sets of proton peaks of H_2**L1**-Boc are attributed to its two conformers in solution. Lower: ^{1}H NMR spectra of digested MUF-77-methyl-1 showing the integrals that match with the formula [$Zn_4O(hmtt)_{4/3}$(**L1**)$_{1/2}$(bdc)$_{1/2}$]. The spectrum of H_2**L1** is also complicated by the existence of two conformers. Overlaid ^{1}H NMR spectra of digested MUF-77-methyl-**1**-Boc together with H_2**L1**-Boc in DMSO-d_6 can be found in Electronic Appendix C.

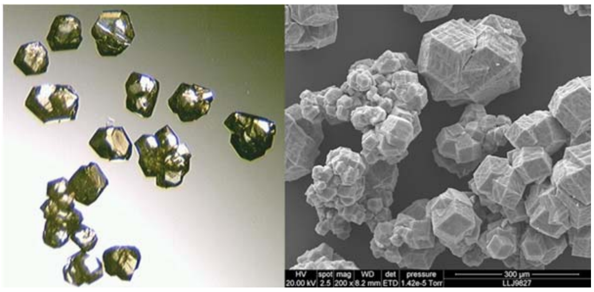

Figure 5.3 Optical (left) and SEM (right) microscopy images of MUF-77-methyl-**1** crystals produced by thermolysis of MUF-77-methyl-**1**-Boc.

Optical and scanning electron microscopy (SEM) images show that MUF-77-methyl-**1** crystals maintain their perfect macroscopic integrity and transparency after thermolysis (Figure 5.3). This indicates the thermolysis of MUF-77-methyl-**1**-Boc is a single-crystal to single-crystal transformation.

Single X-ray crystallography of MUF-77-methyl-**1**-Boc shows that the framework diffracts to high Bragg angles. The best fit of the systematic absences and the $|E^2 - 1|$ value (0.977) are given by the centrosymmetric *P*m-3 space group. This is the same space group as MUF-77-methyl. However in reality it cannot be correct since it contains symmetry elements that are incompatible with the enantiopure proline moiety. The chiral space group *P*23 is also a viable choice. However the refinement was still carried out in *P*m-3 for the following reasons. 1) The atoms of the pyrrolidine ring and Boc group of the proline unit, which encompass the chiral part of the MOF, were not visible on electron density difference map. 2) The proline group is disordered by crystallographic symmetry over the 2, 2′, 6, and 6′ positions in the same way in both space groups. 3) Refinement in *P*23 resulted in unrealistic bond length values. 4) Refinement in *P*23 ended up with a Flack parameter very close to 0.5, again indicating that a racemic twinned model better fits experimental data, which is unrealistic.

Initial refinement in *P*m-3 showed the overall framework structure of MUF-77-**1**-Boc is nearly the same as MUF-77-methyl (described in Chapter 4), except for the bpdc backbone. In MUF-77-methyl-**1**-Boc, the biphenyl rings of **L1**-Boc are disordered over two locations since they lie just off special positions defined by a mirror plane. This implies that the proline group is disordered over eight positions since it is attached to any one of the four crystallographically-equivalent 2/2'/6/6′ carbon atoms of the biphenyl rings. To generate a model of MUF-77-methyl-**1**-Boc for the final refinement, relative atomic positions for most of the atoms of the L-proline-Boc unit were taken from the crystal structure of a related compound (*S*)-Me$_2$**L2** (see section 5.2.4). MUF-77-methyl-**1** was modelled similarly with excellent refinement statistics (Table 5.1).

Table 5.1 Crystallography data summary of MUF-77-methyl-**1**-Boc and MUF-77-methyl-**1**

MOF	**MUF-77-methyl-1-Boc**	**MUF-77-methyl-1**
Formula	$C_{64}H_{50}NO_{14.5}Zn_4$	$C_{61.5}H_{46}NO_{13.5}Zn_4$
Formula weight	1326.53	1276.47
Crystal size (mm)	0.803 × 0.803 × 0.736	0.727 × 0.645 × 0.620
Temperature (K)	290(2)	291(2)
Wavelength (Å)	1.54178	1.54178
Crystal system	cubic	cubic
Space group	*Pm*-3	*Pm*-3
Unit cell length (Å)	29.9444(6)	29.9461(3)
Unit cell volume (Å^3)	26850.2(16)	26854.7(8)
Z	6	6
D_{calc} (g cm^{-3})	0.492	0.474
μ (mm^{-1})	0.794	0.782
F(000)	4062	3900
Reflns coll./unique, R_{int}	103365 / 9316, 0.0518	103850 / 9315, 0.0307
Data range	6.6°<θ<72° or 6.7Å>d >0.81Å	6.6°<θ<72° or 6.7Å>d >0.81Å
Index ranges	$-32 \leq h \leq 36$, $-35 \leq k \leq 36$, $-30 \leq l \leq 21$	$-15 \leq h \leq 36$, $-36 \leq k \leq 33$, $-36 \leq l \leq 21$
Completeness	99.7%	99.7%
T_{min}, T_{max}	0.39, 1.00	0.76, 1.00
R indices for data with I>2σ(I)	$R_1 = 0.0681$; $wR_2 = 0.1865$	$R_1 = 0.0372$; $wR_2 = 0.1034$
R indices for all data	$R_1 = 0.0795$; $wR_2 = 0.1945$	$R_1 = 0.0414$; $wR_2 = 0.1170$
Largest difference peak and hole (e Å^{-3})	0.48 / −0.71	0.24 / −0.47

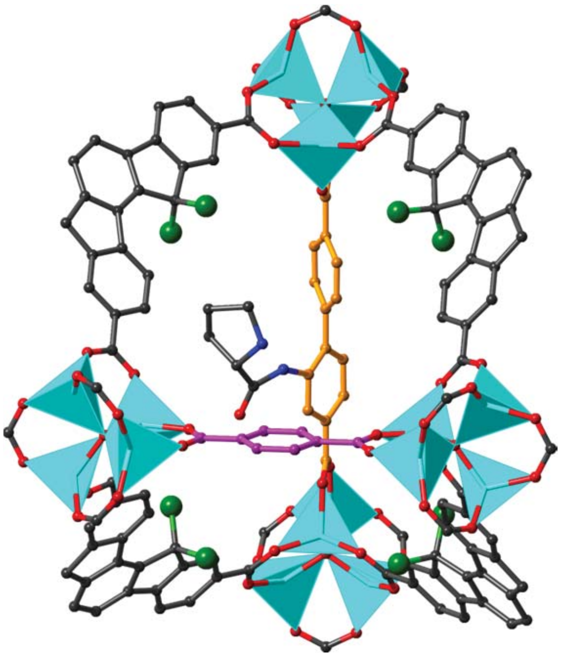

Figure 5.4 A view showing the tetrahedral cavity of the crystal structure of MUF-77-methyl-**1**. The position of the (*S*)-proline group is determined using a combination of the experimental X-ray diffraction data of MUF-77-methyl-**1** and (*S*)-Me$_2$**L2**. The bpdc backbone of **L1** is coloured in orange. bdc ligand is coloured in magenta. The methyl groups of hmtt ligands are highlighted in green.

In the structure of MUF-77-methyl-**1**, the immediate environment of every proline group is identical, which is ideal for producing a uniform outcome to reactions catalysed by this group. The proline nitrogen points towards the interior of the tetrahedral cavity which is defined by four hmtt ligands, a bdc ligand and the **L1** itself (Figure 5.4). Because there is no exact translational relationship between the proline groups of its adjacent pores, they are not strictly identical. That is, the proline groups in neighbouring pores will be randomly oriented with respect to one another. However, these differences between the sites of catalysis are expected to be too minor to impact on the catalytic behaviour of the proline groups. We consider MUF-77-methyl-1 to be a single-site heterogeneous catalyst with a well-defined local environment.

5.2.2 Catalysis study

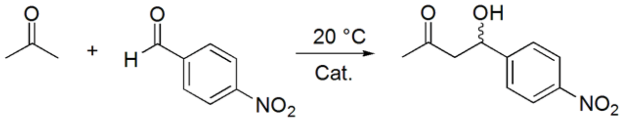

Scheme 5.2 An asymmetric aldol reaction that is catalysed by MUF-77-methyl-**1**.

The aldol reaction as shown in Scheme 5.2 was used to assess the catalytic performance of MUF-77-methyl-**1**. Stock solutions of the reagents were prepared by dissolving 4-nitrobenzaldehyde in acetone with various amount of water. Nitrobenzene was added as an internal standard for HPLC analysis. No uncatalysed background reaction was detected over a period of one month. MOF crystals were then immersed in a known amount of a stock solution and the mixture was tumbled or stood at 20 °C for 24 hours. The supernatant was analyzed by HPLC with a chiral column. We opted not to stir the reaction mixture to avoid grinding the crystals during the reaction, which increases the catalytic sites that are on the outer surface of the MOF crystal[266] and can lead to the solid catalyst being trapped in the meniscus.

The effect of catalyst loading was studied first (Table 5.2, entry 1-5). It was found that using 30% catalyst (moles of proline with respect to 4-nitrobenzaldehyde). led to a ca. 50% conversion of the aldehyde to the aldol product over 24 hours. This is an ideal conversion fraction as it allows variations in the efficiency of the reaction under other conditions to be easily identified. Interestingly, we found that the reaction rate does not depend on whether the reaction is stood or tumbled (Table 5.2, entry 3 and 6). This implies that unassisted diffusion of the substrate and product into and out of the MOF crystals is rapid.

A range of control experiments were performed. A homogeneous reaction using molecular catalyst Me_2**L1** showed that it only accelerates the reaction with respect to MUF-77-methyl-**1** by a small margin, which is consistent with rapid diffusion within the pores of the MOF catalyst. MUF-77-methyl-**1**-Boc and MUF-77-methyl-**1**-direct are both catalytically inactive (entries 7 and 8). The former observation is easily understood on the basis of the unavailability of the pyrrolidine nitrogen atom, while the latter may be due to the side reactions occurred during the MOF synthesis of the pyrrolidine nitrogen atom, as evident from ^{1}H NMR spectrum of digested MUF-77-methyl-**1**-direct. We also filtered the catalyst from the reaction mixture and found this to halt the reaction. These control experiments imply that the proline unit is the only catalytically-active site, and that the catalysis is heterogeneous in nature and not due to dissolved framework components. The failure of route 2 to produce a catalytically competent material underscores the utility of the thermolabile protecting groups in introducing catalytic centres to MOFs.

Table 5.2 Aldol reactions catalysed by MUF-77-methyl-**1** and related compounds.

Entry	Catalyst	Method	H_2O	Cat. loading	Conversion	Rate constant	e.e.
1	MUF-77-methyl-**1**	Tumbled	5	9	16	0.17	17
2	MUF-77-methyl-**1**	Tumbled	5	21	37	0.46	18
3[a]	MUF-77-methyl-**1**	Tumbled	5	30	47,47	0.63	17,19
4	MUF-77-methyl-**1**	Tumbled	5	40	60	0.92	17
5	MUF-77-methyl-**1**	Tumbled	5	51	70	1.2	17
6	MUF-77-methyl-**1**	Stood	5	30	47	0.63	19
7	MUF-77-methyl-**1**-Boc	Stood	5	30	0	-	-
8	MUF-77-methyl-**1**-direct	Stood	5	30	0	-	-
9	Me_2**L1**	Stood	5	30	52	0.73	31
10	MUF-77-methyl-**1**	Stood	0	30	19	0.21	0
11	MUF-77-methyl-**1**	Stood	2	30	22	0.25	16
12	MUF-77-methyl-**1**	Stood	10	30	64	1.0	23
13	MUF-77-methyl-**1**	Stood	20	30	82	1.7	24

Reaction conditions: 20 °C, 24 hour reaction time, initial concentration of 4-nitrobenzaldehyde is 0.04 M in acetone. Water is in % [(V(water)/V(acetone)]. Rate constant unit: mol L^{-1} (acetone) day^{-1}, based on consumption of 4-nitrobenzaldehyde. A detailed definition of the reaction rate constant is available in the experimental section. a) Results from two independent experiments.

Next, the effect of water was studied (entry 6 and 10-13). It was found that when the concentration of water increases, the reaction not only goes faster but the enantioselectivity is also enhanced. Zn_4O-carboxylate MOFs typically have very low tolerance to moisture as well as liquid water. The ability to conduct this reaction in the presence of 20% liquid water is attributed to the exceptional water stability of the MUF-77 family, as demonstrated in Chapter 4. In the presence of 20% water, MUF-77-methyl-**1** showed exceptional resilience: its catalytic activity was undiminished, aside from a small drop after the first cycle, for seven cycles (Figure 5.5 right).

The variations in cycles 2 - 7 are fluctuations in the measurement of the activity of the catalyst (its calculated rate constant) and ee of the product. Because the total volume of the acetone for these cycles is slightly variable (see experimental section), the initial concentration of 4-nitrobenzaldehyde varies accordingly. This allows an estimate of the maximum error in the ee values to be ±1 and in the rate constant to be ±5%.

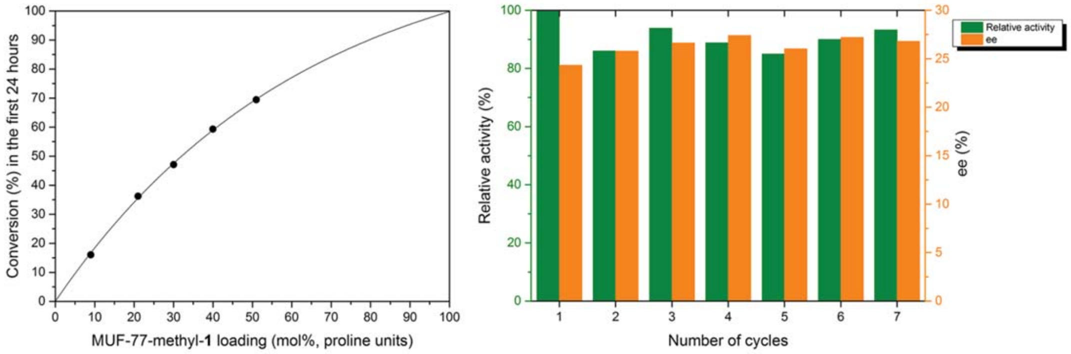

Figure 5.5 Left: a plot of catalyst loading versus conversion of 4-nitrobenzaldehyde to the aldol product over a 24 hour reaction period. Right: a plot showing the recyclability of catalyst MUF-77-methyl-**1** under conditions given in Entry 13 of Table 5.2.

5.2.3 Tuning the catalytic pore environment *via* site-directed "mutagenesis"

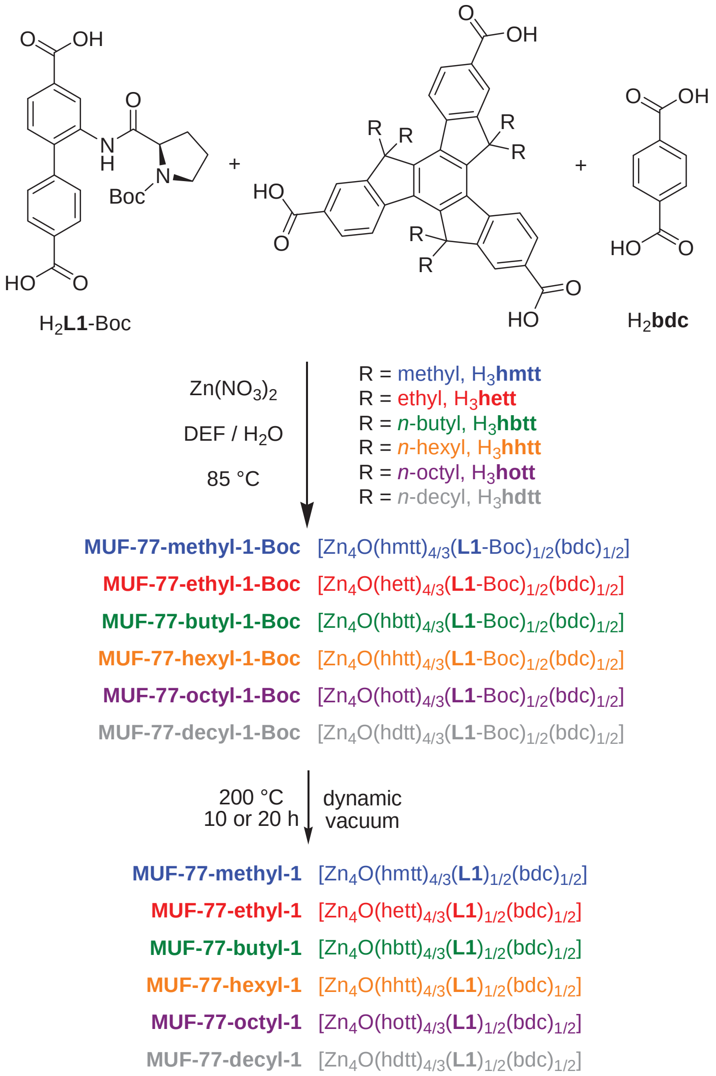

Scheme 5.3 Synthetic route to the MUF-77-**1**-Boc and MUF-77-**1** series of materials.

MUF-77-methyl-**1** features an activation site in the form of a proline group. Our plan was to tune the outcome of the reactions catalysed by this group by varying the modulator sites in its surroundings. The modulator sites we choose to use were alkyl substituents appended to the truxene ligand. Using strategies developed in Chapter 4, we synthesized a family of MUF-77-**1** catalysts with C_1 to C_{10} alkyl chains (Scheme 5.3). Boc-protected frameworks were initially synthesized before the catalytically-active proline site was revealed by postsynthetic thermolysis. The completeness of the thermolysis reaction, which is crucial for maximum catalytic efficiency, was assessed by ^{1}H NMR spectroscopy on digested samples. It was found that for methyl-, ethyl-, and butyl- substituted MUF-77-**1**-Boc, complete thermolysis requires 10 hours' heating. A thermolysis time of 20 hours was sufficient to fully deprotect the hexyl, octyl and decyl members of the MUF-77-**1**-Boc series. As for MUF-77-methyl-**1**, ^{1}H NMR, PXRD, optical microscopy and gas adsorption studies were conducted to confirm their identity, purity and post-thermolysis porosity of these new materials. The PXRD and gas adsorption experiments are summarized in Figure 5.6. The MUF-77-alkyl-**1** MOFs are highly crystalline, isoreticular to one another and have permanent porosity. Thus, through site-directed mutagenesis of the truxene ligand a family of six MOFs featuring catalytic pores that are systematically varied was successfully created.

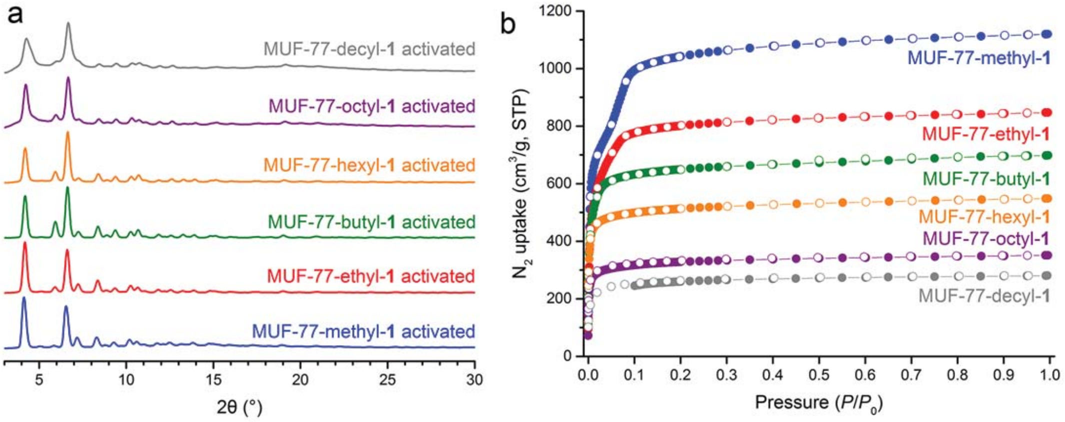

Figure 5.6 a) Experimental PXRD patterns of MUF-77-alkyl-**1** MOFs. b) Nitrogen adsorption isotherms of MUF-77-methyl-**1**-Boc and MUF-77-methyl-**1** measured at 77 K. Adsorption data points for MUF-77-decyl-**1** at the pressure range $0 < P/P_0 < 0.1$ was not measured due to the slow adsorption kinetics.

The impact of these modifications on the aldol reaction shown in Scheme 5.2 was studied. As shown in Table 5.3, a clear trend emerges showing the reaction slows down with alkyl chains that are longer than ethyl. The ee of the aldol product fluctuates but is generally lower than that measured for MUF-77-methyl-**1**.

There are a number of possible explanations for the observed relationship between catalyst structure and performance. (i) The MOFs with longer alkyl groups are likely, on the basis of the parent MUF-77 series, to be less stable in water; therefore, they may be degrading over time. (ii) While it is assumed that the alkyl groups have significant flexibility when solvated with acetone under the conditions of the catalysis reaction, the longer alkyl chains may be inhibiting the diffusion of the reactants and products to/from the active site. This could be examined by the measurement of the diffusion constant of the reactants in the frameworks by pulsed-gradient NMR spectroscopy.[267] (iii) It is known that the rate determining step of aldol reactions catalysed by molecular proline catalysts is the release of the product by hydrolysis of an intermediate iminium ion.[268] On the assumption that the rate determining step in MUF-77-**1** is the same, longer alkyl substituents, which create more hydrophobic environments, might hinder this step and thus slow down the reaction. This could be investigated by preparing MUF-77 “mutants” featuring hydrophilic modulator sites that induce high concentrations of water in the catalytic pore.

Table 5.3 A summary of the aldol reaction between 4-nitrobenzaldehyde and acetone catalysed byMUF-77-alkyl-1.

Entry	Catalyst	Method	H_2O	Cat. loading	Conversion	Rate constant	e.e.
1	MUF-77-methyl-**1**	Stood	20	30	83	1.8	25
2	MUF-77-ethyl-**1**	Stood	20	30	85	1.9	16
3	MUF-77-butyl-**1**	Stood	20	30	45	0.60	28
4	MUF-77-hexyl-**1**	Stood	20	30	25	0.29	23
5	MUF-77-octyl-**1**	Stood	20	30	29	0.34	9
6	MUF-77-decyl-**1**	Stood	20	30	15	0.16	17

Reaction conditions: 20 °C, 24 hour reaction time, initial concentration of 4-nitrobenzaldehyde is 0.04 M in acetone. Water is in % [(V(water)/V(acetone)]. Rate constant unit: mol L^{-1} (acetone) day^{-1}, based on consumption of 4-nitrobenzaldehyde. A detailed definition of the reaction rate constant is available in the experimental section.

5.2.4 Catalysis by a proline group appended to the bdc ligand

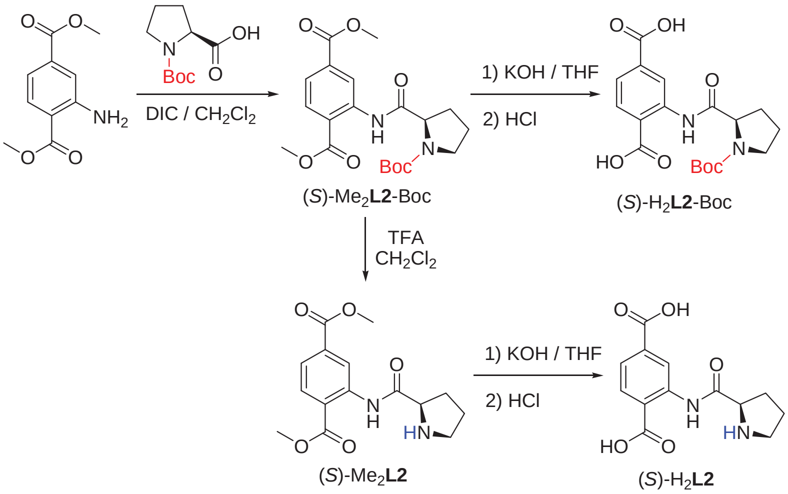

Scheme 5.4 Synthetic routes to H_2bdc derived ligands with proline units.

Another advantage of using multicomponent MOFs as a platform for heterogeneous catalysis is that the framework component to which the catalytic group is appended can be varied without inducing global structural change in the material. For the MUF-77 family, a catalytic site could be appended to the bdc or the truxene linker (in addition to the bpdc linker as described above). From the perspective of synthetic chemistry, the former option is more expedient. We therefore synthesized the proline derivatives of H_2bdc shown in Scheme 5.4. The amide coupling reaction does not lead to any degree of racemization: (*S*)-Me$_2$**L2**-Boc and (*S*)-Me$_2$**L2** exhibit 100 % enantiopurity as determined by HPLC. (*R*)-Me$_2$**L2**-Boc was also prepared to confirm that its peak does not overlap with the *S* enantiomer. The absolute configurations of (*S*)-Me$_2$**L2**-Boc and (*R*)-Me$_2$**L2**-Boc were confirmed by X-ray crystallography (Figure 5.7).

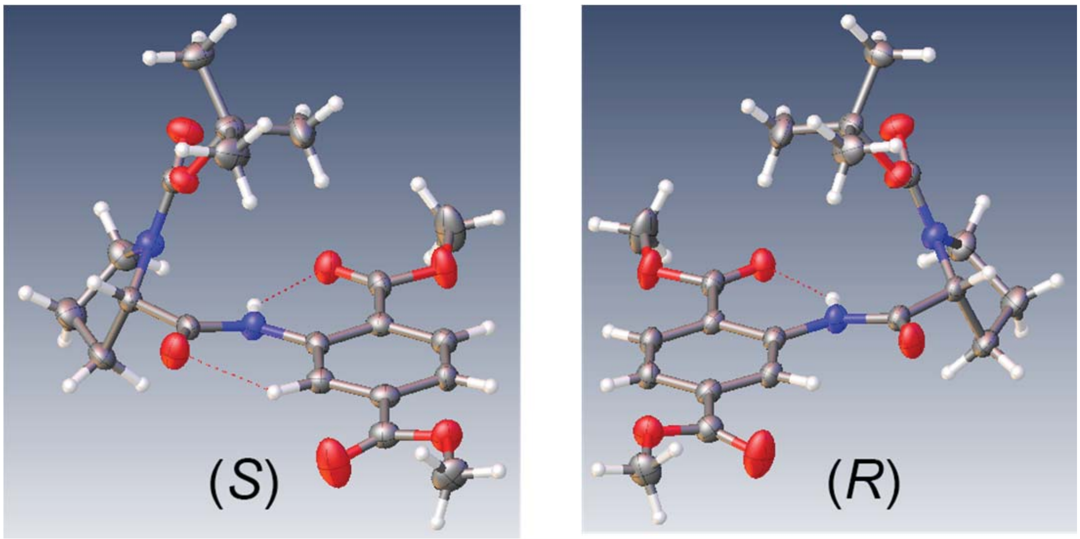

Figure 5.7 ORTEP diagrams of the structures of (*S*)-Me_2**L2**-Boc and (*R*)-Me_2**L2**-Boc, as determined by SC-XRD, showing 50% probability of the atomic displacement ellipsoids. Graphics were generated using Olex 2.[241]

As illustrated in Scheme 5.5, three MUF-77 variants with proline units on the bdc sites were synthesized. The formula of MUF-77-methyl-**2**-Boc was determined as $[Zn_4O(hmtt)_{4/3}(bpdc)_{1/2})((S)\text{-}\mathbf{L2}\text{-Boc})_{1/2}]$ by ^1H NMR spectroscopy of a digested MOF sample. Similarly, MUF-77-methyl-**2**-Boc was heated to 200 °C for 10 hours under dynamic vacuum to fully remove the Boc protecting group, affording MUF-77-methyl-**2** with a formula of $[Zn_4O(hmtt)_{4/3}(bpdc)_{1/2})((S)\text{-}\mathbf{L2})_{1/2}]$ as confirmed by ^1H NMR spectroscopy. As a comparison, MUF-77-methyl-**2**-direct was also synthesized using (*S*)-**L2** in place of (*S*)-**L2**-Boc.

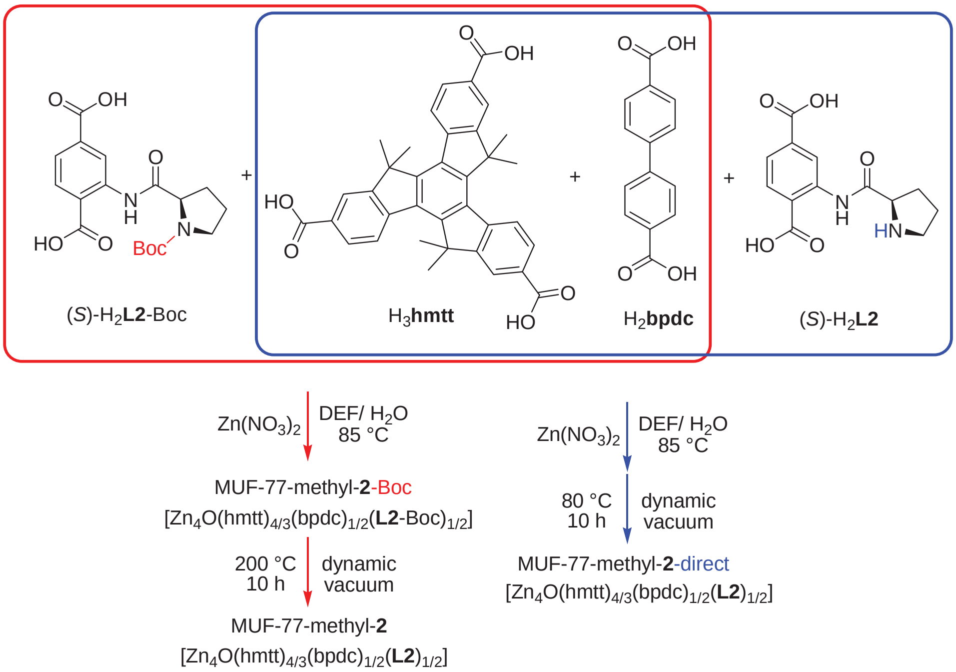

Scheme 5.5 Synthetic route to MUF-77-methyl-**2**-Boc and MUF-77-methyl-**2**. The latter can be prepared by thermolysis of MUF-77-methyl-**2**-Boc (red arrows) or by direct synthesis (blue arrows).

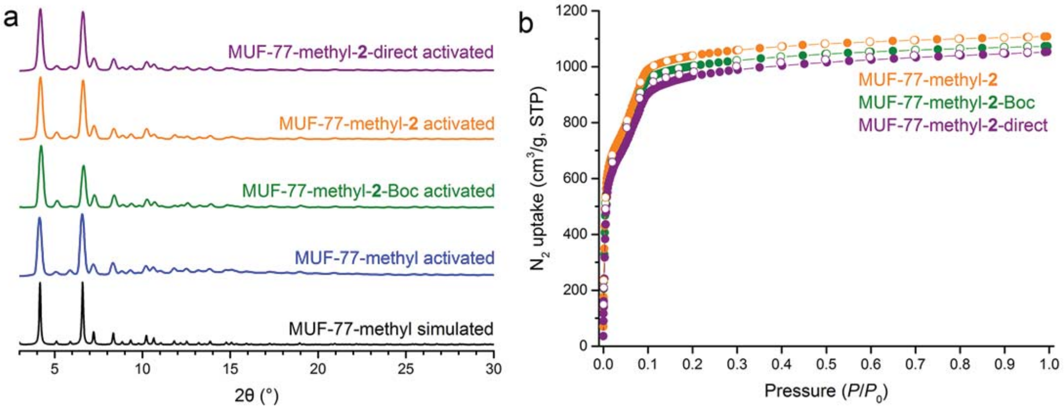

Figure 5.8 a) Experimental PXRD patterns of MUF-77-methyl-**2**-Boc, MUF-77-methyl-**2** and MUF-77-methyl-**2**-direct. b) Nitrogen adsorption isotherms of MUF-77-methyl-**2**-Boc, MUF-77-methyl-**2** and MUF-77-methyl-**2**-direct measured at 77 K.

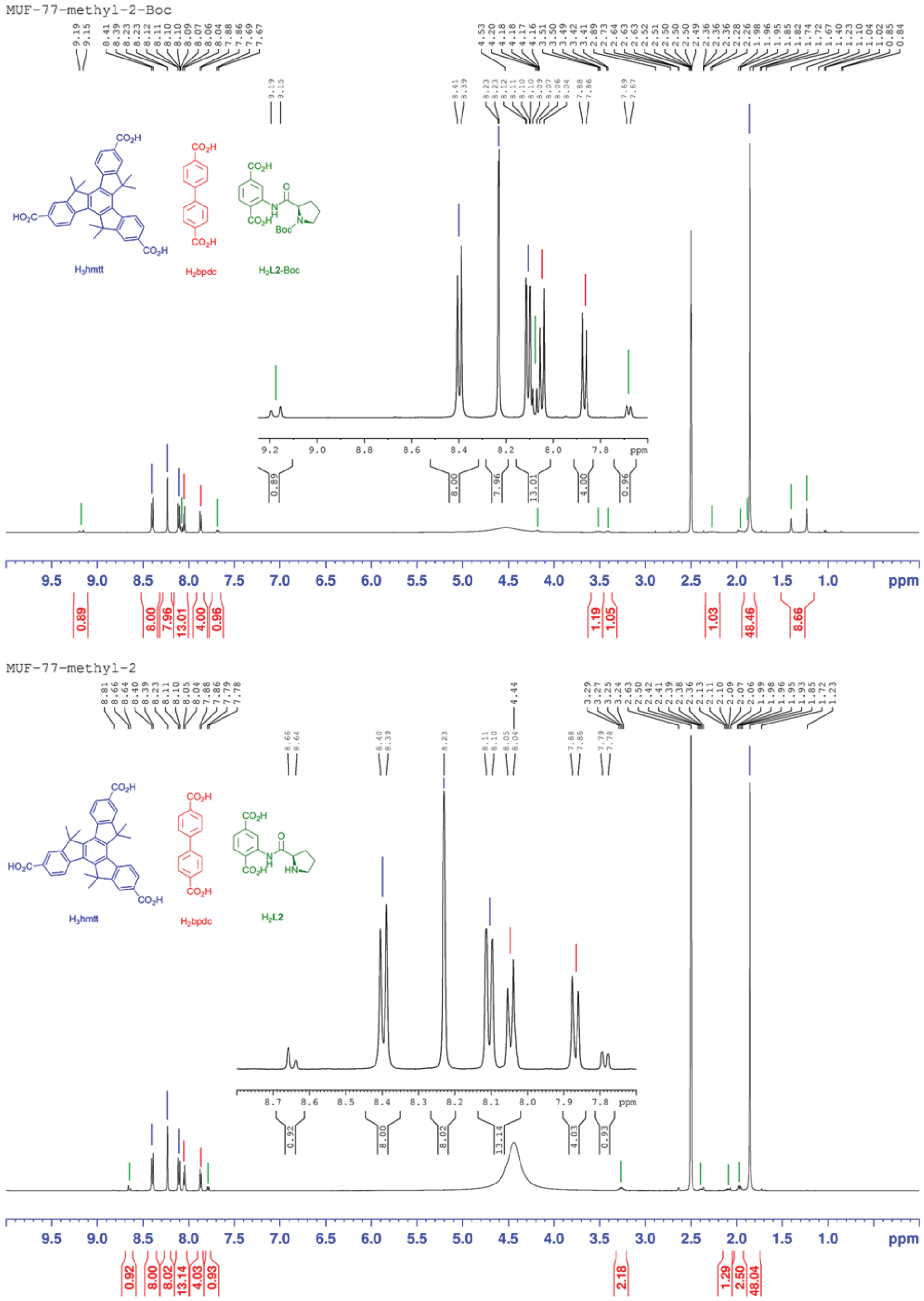

Figure 5.9 ^{1}H NMR spectra of digested MUF-77-methyl-**2**-Boc and MUF-77-methyl-**2**. Complete thermolysis of the former to produce the latter is confirmed by the disappearance of the two proton peaks of the Boc group at 1.24 and 1.41 ppm, contributed from the two conformers of (*S*)-H_2**L2**-Boc.

Table 5.4 A summary of the aldol reaction between 4-nitrobenzaldehyde and acetone catalysed by MUF-77-alkyl-**2**.

Entry	Catalyst	Time	H_2O	Cat. loading	Conversion	Rate constant	e.e.
1	MUF-77-methyl-**1**	24	5	30	47	0.63	19
2	MUF-77-methyl-**2**	6	5	30	55	3.2	-2[c]
3	MUF-77-methyl-**2**	24	5	30	95	3.0	-2[c]
4	MUF-77-methyl-**2**	24	20	30	89	2.2	-9[c]
5	MUF-77-methyl-**2**-Boc	24	5	30	0	-	-
6	MUF-77-methyl-**2**-direct	24	5	30	0	-	-
7	(*S*)-Me$_2$**L2**	24	5	30	>99	5.4[b]	30

Reaction conditions: 20 °C, stood, initial concentration of 4-nitrobenzaldehyde is 0.04 M in acetone. Water is in % [(V(water)/V(acetone)]. Reaction time unit: hour. Rate constant unit: mol L^{-1} (acetone) day^{-1}, based on consumption of 4-nitrobenzaldehyde. A detailed definition of the reaction rate constant is available in the experimental section.

a) Calculated from ([Peak area of elimination product]/[Peak area of total aldol products]) x 100 %. b) Based on the fitting of kinetic data over the initial 6 hours. c) Negative sign indicates reversed enantioselectivity compared to MUF-77-methyl-**1**. Here the *S* product is the major enantiomer.

The relocation of the catalytic proline site from the bpdc ligand to the bdc ligand has a pronounced impact on the catalysis reaction. First, the reaction is five times faster (Table 5.4, entry 1 and 2). Second, the enantioselectivity is reversed (Table 5.4, entry 2-4).

The single crystal X-ray structure of MUF-77-methyl-**2** provides additional insight into this accelerated catalysis. Similar to MUF-77-methyl-**1**, the crystal structure of MUF-77-methyl-**2** was solved in *P*m-3 and the observed proline unit is disordered by crystallographic symmetry over four sites. The first four non-hydrogen atoms attached to the phenyl ring of (*S*)-**L2** were found on the electron difference map and the rest of the atoms of the proline unit were attached using their idealized positions obtained from molecular analogue, (*S*)-Me$_2$**L2**-Boc. From the crystal structure (Figure 5.10), it is clear that the active site of the catalyst points away from the hydrophobic alkyl chains of the truxene, and faces towards a hydrophilic pocket that is close to a Zn_4O cluster. The local water concentration near the hydrophilic sites is expected to be higher compared to hydrophobic sites. Thus the rate determining step, which involves hydrolytic release of the product from the proline catalyst, is maybe accelerated. Since the proline unit of MUF-77-methyl-**1** is directed towards a hydrophobic region of the framework (see earlier), it will not benefit from this acceleration and its apparent rate constants are smaller of that of MUF-77-methyl-**2**.

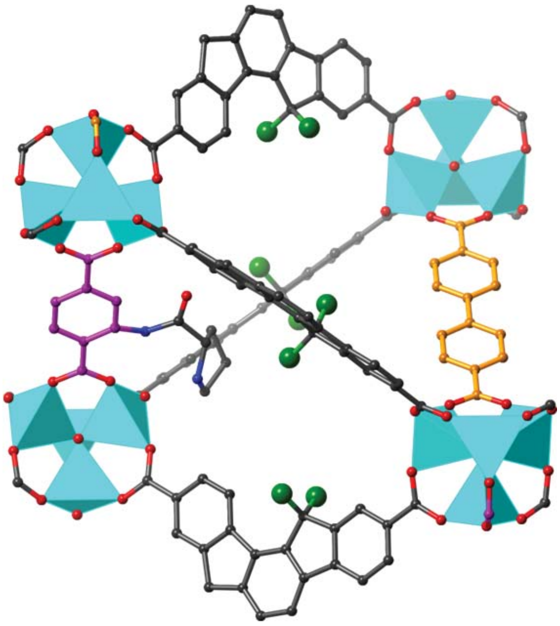

Figure 5.10 A view showing the tetrahedral cavity of the SC-XRD structure of MUF-77-methyl-**2**. The position of the (*S*)-proline group is determined using a combination of experimental X-ray diffraction data of MUF-77-methyl-**2** and (*S*)-Me_2**L2**. The bpdc is coloured in oranges. The bdc backbone of **L2** is coloured in magenta. The methyl groups of hmtt ligands are highlighted in green.

5.3 Conclusion

Using the water stable MUF-77 family as platform, we successfully introduced a homochiral *activation site*, an (*S*)-proline derivative, into the framework through ligand functionalization followed by post-synthetic thermal deprotection. This creates a catalytic pore with its nearby chemical environment well defined and tunable by *modulator sites* on the truxene coligand. By systematic alterations to this modulator site, an isoreticular family of MOFs with tunable hydrophobicities and steric characteristics were created. We showed the reaction rate and enantioselectivity of a catalytic aldol reaction can be tuned by the strategy. In addition, the position of the catalytic site (*activation site*) can be altered, which changes its immediate chemical environment and both reverses the reaction enantioselectivity and increases the reaction rate.

Table 5.5 Crystallography summary of MUF-77-methyl-**2**.

MOF	**MUF-77-methyl-2**
Formula	$C_{61.5}H_{46}NO_{13.5}Zn_4$
Formula weight	1276.47
Crystal size (mm)	0.5 × 0.5 × 0.5
Temperature (K)	293(2)
Wavelength (Å)	1.54178
Crystal system	cubic
Space group	*Pm*-3
Unit cell length (Å)	29.9603(3)
Unit cell volume (Å^3)	26892.9(8)
Z	6
D_{calc} (g cm^{-3})	0.473
μ (mm^{-1})	0.781
F(000)	3900
Reflns coll./unique, R_{int}	103850 / 9315, 0.0307
Data range	6.6°<θ<72° or 6.7Å>d >0.81Å
Index ranges	$-28 \leq h \leq 29$, $-33 \leq k \leq 29$, $-17 \leq l \leq 36$
Completeness	99.6%
T_{min}, T_{max}	0.73, 1.00
R indices for data with I>2σ(I)	$R_1 = 0.0364$; $wR_2 = 0.1615$
R indices for all data	$R_1 = 0.0395$; $wR_2 = 0.1649$
Largest difference peak and hole (e Å^{-3})	0.29/ −0.47

5.4 Experimental section

5.4.1 General procedures

All starting compounds and solvents were used as received from commercial sources without further purification unless otherwise noted. (*S*)-H_2**L1**-Boc and (*S*)-H_2**L1** was provided by David Lun using the same batch that was reported and fully characterized in cited reference.[1] Column chromatography was carried out on silica gel (grade 60, mesh size 230-400, Scharlau). NMR spectra were recorded at room temperature (unless otherwise noted) on Bruker-400 and Bruker-500 Avance instruments, with the use of the solvent proton as an internal standard. HPLC analyses were carried out using a Thermoscientific Ultimate 3000 instrument.

5.4.2 Ligand synthesis

(*S*)-Me_2**L2**-Boc, (*S*)-H_2**L2**-Boc, (*S*)-Me_2**L2**-Boc and (*S*)-Me_2**L2** were synthesized according to Scheme 5.4. (*R*)-Me_2**L2**-Boc was synthesized using the same method as (*S*)-Me_2**L2**-Boc, and its spectroscopic data is identical to (*S*)-Me_2**L2**-Boc. Detailed procedures and characterization data is available in Electronic Appendix C.

5.4.3 MOF synthesis and characterization

In general, three ligands (Table 5.6) and zinc nitrate tetrahydrate (56 μmol) were dissolved or well suspended in DEF (1 mL) and H_2O (30 μL) in a 4 mL scintillation vial which had been pretreated with Sigmacote. The vial was heated to 85 °C for various periods of time and allowed to cool naturally. This yields crystals of the MOF catalysts or their precursors. To scale up the synthesis, a similar reagent ratio was used. Reactions were carried out in Schott bottles with various amounts of solvents.

For the deprotection reactions, Boc-protected MOFs were thoroughly washed with DMF then dichloromethane. These precursor MOF crystals were heated at a rate of 5 °C to 200 °C under dynamic vacuum and held for 10 or 20 hours. The successful completion of the thermolysis reaction was monitored by ^{1}H NMR of digested products.

Table 5.6 Synthetic conditions for MUF-77 catalysts and their precursors

MOF	Ligand A	n (µmol)	Ligand B	n (µmol)	Ligand C	n (µmol)	Activation Temperature (°C)	Activation Time (hour)
MUF-77-methyl-**1**-Boc	H_3hmtt	8	(*S*)-H_2**L1**-Boc	4.5	H_2bdc	11.5	80	5
MUF-77-methyl-**1**	H_3hmtt	8	(*S*)-H_2**L1**-Boc	4.5	H_2bdc	11.5	200	10
MUF-77-methyl-**1**-direct	H_3hmtt	8	(*S*)-H_2**L1**-Boc	4.5	H_2bdc	11.5	80	5
MUF-77-ethyl-**1**	H_3hett	8	(*S*)-H_2**L1**-Boc	4.5	H_2bdc	11.5	200	10
MUF-77-butyl-**1**	H_3hbtt	8	(*S*)-H_2**L1**-Boc	4.5	H_2bdc	11.5	200	10
MUF-77-hexyl-**1**	H_3hhtt	8	(*S*)-H_2**L1**-Boc	4.5	H_2bdc	11.5	200	20
MUF-77-octyl-**1**	H_3hott	8	(*S*)-H_2**L1**-Boc	4.5	H_2bdc	11.5	200	20
MUF-77-decyl-**1**	H_3hdtt	8	(*S*)-H_2**L1**-Boc	4.5	H_2bdc	11.5	200	20
MUF-77-methyl-**2**-Boc	H_3hmtt	8	H_2bpdc	8	(*S*)-H_2**L2**-Boc	16	80	5
MUF-77-methyl-**2**	H_3hmtt	8	H_2bpdc	8	(*S*)-H_2**L2**-Boc	16	80	5
MUF-77-methyl-**2**-direct	H_3hmtt	8	H_2bpdc	11.5	(*S*)-H_2**L2**-Boc	4.5	200	10

5.4.4 ^{1}H NMR analysis of digested MOF samples

For ^{1}H NMR spectroscopy, the mother liquor of the as-synthesized MOF crystals was replaced with fresh dry DMF multiple times. The MOF crystals were then filtered through a Büchner funnel on a filter paper under suction and the surfaces of the crystals were allowed to dry. The crystals were then digested using the following protocol: 23 µL of a 35% DCl solution in D_2O was mixed with 1 mL of DMSO-*d*$_6$ to give a DCl/DMSO-*d*$_6$ stock solution. Around 5 mg of MOF was digested in 150 µL of this stock solution together with 450 µL of DMSO-*d*$_6$. Spectra were acquired immediately following dissolution. Spectra for all MOFs are presented in Electronic Appendix C.

5.4.5 Single crystal X-ray diffraction

Data collections were performed on a Rigaku Spider diffractometer equipped with a MicroMax MM007 rotating anode generator (Cu$_\alpha$ radiation, 1.54180 Å), high-flux Osmic multilayer mirror optics, and a curved image-plate detector. Data were integrated and scaled and averaged with FS Process.**[203]** XPREP**[204]** was used to determine the space group and the structures were solved using direct method under SHELXS**[204]** and refined with SHELXL**[204]** under an Olex 2**[241]** graphical interface. Crystallography of MOFs will be described here, whereas crystallography of (*S*)-Me$_2$**L2**-Boc and (*R*)-Me$_2$**L2**-Boc are detailed in Electronic Appendix C.

As-synthesized MOF crystals were soaked in fresh dry DMF and DMF was replenished several times within a day. The crystals were soaked overnight then the solvent was exchanged with dry dichloromethane and the dichloromethane was again replenished several times. The crystals were soaked in fresh dry dichloromethane overnight before being activated under dynamic vacuum at 80 or 200 °C for various periods of time. The vacuum oven was back filled with nitrogen to produce crystals suitable for single crystal X-ray diffraction analyses.

All zinc, oxygen and carbon atoms from ligand and framework backbones were found in the electron density difference maps and refined anisotropically. Ideal positions for all hydrogen atoms were calculated and refined as a riding model. The first four non-hydrogen atoms coming off the bpdc and bdc ring of (*S*)-**L1**-Boc, (*S*)-**L1**, and (*S*)-**L2** were found on electron density difference maps, despite their low occupancy due to the disorder. To complete the models of pyrrolidine rings, their relative atomic coordinates were taken from single crystal x-ray structure of (*S*)-Me$_2$**L2** using the FRAG command in Olex 2. In the crystal structure of MUF-77-methyl-**1**-Boc and MUF-77-methyl-**1**, their functional groups were disordered over eight sites so the corresponding atomic occupancies were fixed at 0.125 with a fixed isotropic atomic displacement parameter (0.1). MUF-77-methyl-**2** was treated in a similar way. Although substoichiometric inclusion of **L2** was observed by ^{1}H NMR spectroscopy, the refinements were still carried out with fully occupied models for all ligands.

5.4.6 Powder x-ray diffraction patterns

All powder X-ray diffraction experiments were carried out on a Rigaku Spider X-ray diffractometer with Cu K_α radiation (Rigaku MM007 microfocus rotating-anode generator), monochromated and focused with high-flux Osmic multilayer mirror optics, and a curved image plate detector. The data were obtained from either freshly prepared MOF samples that had been ground into slurry in a small amount of DEF and kept damp with DEF throughout the measurement, or desolvated MOF samples (prepared in the same way as the samples of the single crystal X-ray experiments) that were ground then fixed to a mount with a minimum amount of Fomblin oil. The two-dimensional images of the Debye rings were integrated with 2DP[242] to give 2θ vs I diffractograms. The predicted powder patterns of the MOFs were generated from their single-crystal structures using Mercury v3.3.

5.4.7 Gas adsorption measurements and calculations

Low pressure gas adsorption isotherms were measured by a volumetric method using a Quantachrome Autosorb iQ2 instrument. Freshly prepared MOF samples were washed with DMF then activated by soaking in dry CH_2Cl_2 for several days then transferred to a pre-dried and weighed analysis tube. Excess CH_2Cl_2 was removed under vacuum and the tube back filled with argon before being heated at 1 °C per minute to 80 °C under vacuum. The sample was then held under a dynamic vacuum at 10^{-6} Torr for 10 hours. Accurate sample masses were calculated using degassed samples after sample tubes were backfilled with nitrogen. All adsorption measurements used ultra-high purity gases.

5.4.8 Catalysis

In a typical experiment, a solution with known amount of 4-nitrobenzaldehyde, nitrobenzene and water in 250 μL of acetone was added to a vial with pre-weighed desolvated catalyst. The vial was either tumbled or allowed to stand for various periods of time at 20 °C. After the reaction, 50 μL of the supernatant was diluted with 450 μL of hexane and subjected to HPLC analysis. HPLC analysis was carried out using a CHIRALCEL OJ-H column with a mixed solvent of hexane and isopropyl alcohol (85:15 v/v) at a flow rate of 1.2 ml/min. Products were detected according their absorption of 254 nm UV light. The conversion was calculated by comparing the peak area ratio of 4-nitrobenzaldehyde and nitrobenzene before and after the reaction. Figure 5.11 shows a typical HPLC chromatograph of a reaction mixture with the retention time of each compound identified on the figure and figure caption. The ee value of each reaction is reported based on the excess of the *R* enantiomer, which elutes at 16 minutes.

For recycling experiments, the MOF catalyst was loaded in a vial with a 200 μL glass insert to minimize the catalyst loss between cycles. As expected from the narrow stem at the bottom, the diffusion of the reactant and the product was slower so the conversion was compared against the first cycle to calculate the relative reactivity. For the first cycle, a stock solution containing 150 μL acetone was added in to the vial preloaded with desolvated catalyst. After the first cycle, 50 μL supernatant was subjected to HPLC analysis and the remaining supernatant was decanted. The catalyst was washed with acetone at least three times and the catalyst was immersed in minimum amount of acetone before adding the stock solution for the next cycle. As expected, due to the increase total volume of acetone after the first cycle, the concentration of 4-nitrobenzaldehyde slightly decreased and caused the slight drop in reactivity after the first catalytic cycle.

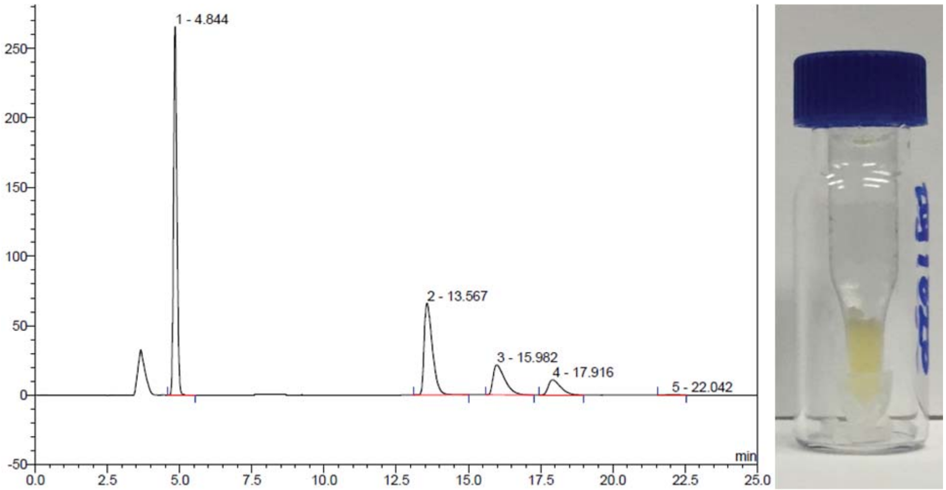

Figure 5.11 Left: A typical HPLC chromatograph of the reaction mixture. Peak 1: nitrobenzene, Peak 2: 4-nitrobenzaldehyde, Peak 3: *R* enantiomer of aldol adduct, Peak 4: *S* enantiomer of aldol adduct, Peak 5: elimination side product. The retention time of acetone is 2.7-2.8 min. The retention time of peak 4 and 5 matches with literature values[1,269] when using a Daicel Chiralpak AS column, eluting with hexane and *i*PrOH mixture (85:15) with a flow rate of 1 ml/min. Because the elimination product peak overlaps with aldol adducts using an AS column, an OJ-H column was used instead. Right: A photo showing the setup for recycling experiments.

Stock solution A was prepared with 4-nitrobenzaldehyde (1.20 mmol), nitrobenzene (1.20 mmol), acetone (30.0 mL) and water (1.50 mL). It was used for reactions in the presence of 5% water. Stock solution B was prepared with 4-nitrobenzaldehyde (0.40 mmol), nitrobenzene (0.40 mmol), acetone (10.0 mL). It was used to determine the impact of water concentration on the reaction. Stock solution C was prepared with 4-nitrobenzaldehyde (1.20 mmol), nitrobenzene (1.20 mmol), acetone (30.0 mL) and water (6.00 mL). It was used for reactions with the presence of 20% water.

Calculation of the apparent rate constant

The reaction rate constant k is calculated based the reaction shown in Scheme 5.2. Thus, the reaction rate, r, based on the consumption of 4-nitrobenzaldehyde can be expressed as a function of reaction rate constant k and the concentration of 4-nitrobenzaldehyde, [PNBA], and acetone [acetone], by assuming the order of the reaction is one based on 4-nitrobenzaldehyde:

$$r = -\frac{d[\mathrm{PNBA}]}{dt} = k[\mathrm{PNBA}][\mathrm{acetone}]^{a}$$

Here, a is the reaction order based on acetone. Since the reaction is carried out in acetone, the above equation can be simplified as

$$r = -\frac{d[\mathrm{PNBA}]}{dt} = k'[\mathrm{PNBA}]$$

where k' is the apparent rate constant.

Solving this differential equation with the following initial condition:

$$[\mathrm{PNBA}] = [\mathrm{PNBA}]_0 \text{ for } t = 0$$

yields

$$\ln[\mathrm{PNBA}] = \ln[\mathrm{PNBA}]_0 - k't$$

Here, $[\mathrm{PNBA}]_0$ is the initial concentration of 4-nitrobenzaldehyde and t is time.

Plotting ln[PNBA] as a function of time yields a linear relationship, as shown in Figure 5.12:

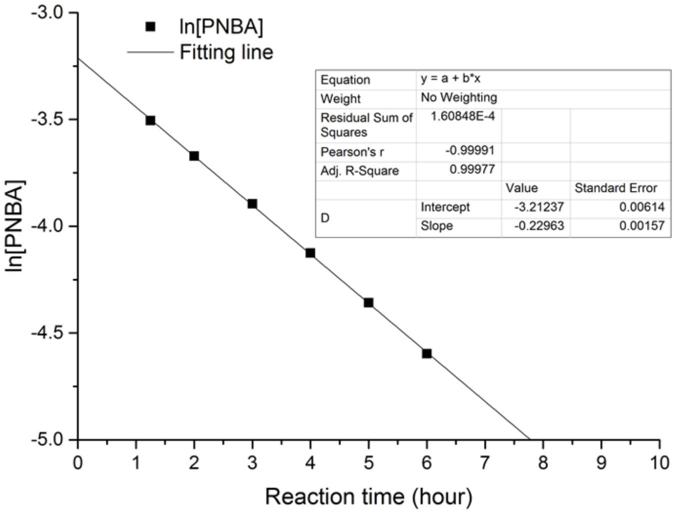

Figure 5.12 Reaction kinetics plot for calculating apparent rate constant for entry 5 of Table 5.4. Note that the unit here for *k'* is mol L^{-1} (acetone) $hour^{-1}$, which was then converted to mol L^{-1} (acetone) day^{-1}.

The linear relationship of the plot proved that the reaction order is indeed one for 4-nitrobenzaldehyde. This allowed us to calculate the apparent reaction constant for each entry by knowing the reaction time and the concentration of 4-nitrobenzaldehyde (by HPLC) during the reaction.

Chapter 6

Summary and Perspectives

6.1 Thesis summary

Before we carried out the work for this thesis, multicomponent MOFs (MC-MOFs) that are constructed with three geometrically distinct organic ligands were not known.[57] Synthesizing MOFs with high complexity had just started to garner interest from MOF researchers.[270,271] However, these studies were limited in MTV-MOFs,[129] and functional groups included in these frameworks were not well ordered.[130]

In this thesis, I have demonstrated that it is possible to construct MC-MOFs from three geometrically-distinct organic ligands. Moreover, I demonstrated their pores can be programed by systematically introducing one, two or three functional groups in the precise locations with perfect order.[191] This level of control was unprecedented in the literature. The discovery of these quaternary MOFs created a new avenue of MOF chemistry, which has recently captured the imagination of other research groups.[214,215]

Fascinating properties also emerged from these quaternary MOFs, such as their exceptional hydrolytic stability.[192] This stability promises practical applications as outlined later. Quaternary MOFs also enabled us to design and synthesize catalysts that feature *activation sites* and *modulator sites*. This chemistry has parallels with enzyme active sites. It was not previously known in MOFs, and would be very difficult to achieve in any other synthetic materials.

6.2 Perspectives on catalysis in quaternary MOFs

In Chapter 5, we only studied one catalytic reaction. In future work, it would be interesting to screen a wide range of reactions, including and beyond aldol reactions. These include Michael, Mannich, Diels-Alder, and Hajos-Parrish-Eder-Sauer-Wiechert reactions, which are all known to be catalysed by proline-based catalysts, as shown in Scheme 6.1.[272,273] In addition, it would also be interesting to incorporate other catalytic moieties in quaternary MOFs, as shown in Scheme 6.2.

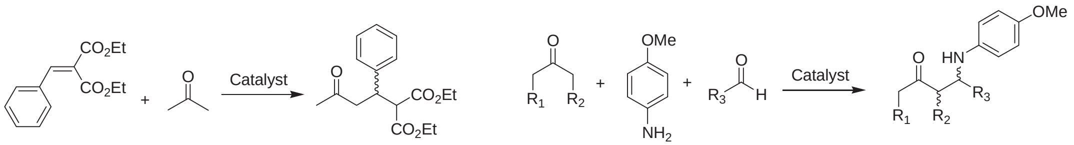

Michael addition reaction

One-pot three-component Mannich-type reaction

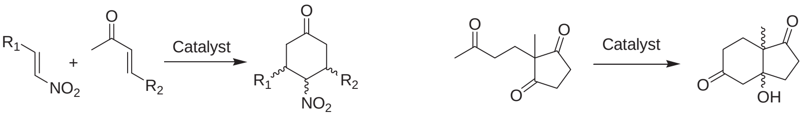

A Diels-Alder reaction

A Hajos-Parrish-Eder-Sauer-Wiechert reaction

Scheme 6.1 Reactions that are known catalysed by proline.

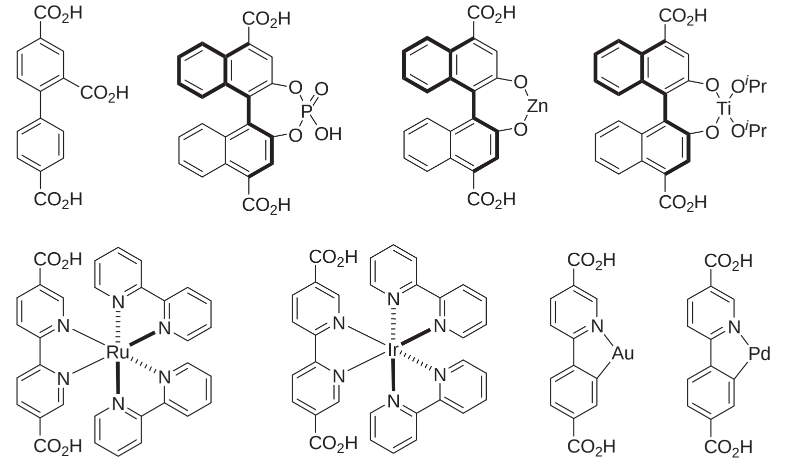

Scheme 6.2 Some examples of catalysts that can be incorporated in MUF-7 and MUF-77 family.

6.3 Introducing more exotic functional groups in quaternary MOFs

Up to this point, functionalization of the truxene ligands has been limited to alkyl substituents, which are chemically rather mundane. It would be interesting to explore functional groups that could bring additional features to MUF-77. As shown in Scheme 6.3, according the general synthetic scheme described in Chapter 4, truxene ligands with hydrophilic chains or chiral centres could be synthesized. Hydrophilic truxenes which are more polar than alkylated ligands could potentially enhance the selective adsorption behaviour of MUF-77s towards CO_2, and thus make them better sorbents for flue gas treatment.

Chiral substituents on the truxene ligand could be useful for chiral separation and asymmetric catalysis. It would be interesting to design and synthesize catalysts that feature a) achiral or racemic activation sites with homochiral modulator sites, and b) homochiral activation sites with modulator sites feature same or inverted chirality. These catalysts could potentially: 1) Generate enantioselectivity from a remote modulator sites rather than the activation unit. 2) Use the modulator site to enhance or override the innate enantioselectivity of chiral activation units.

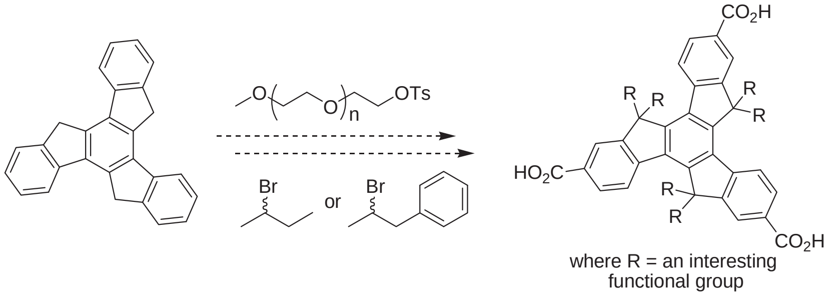

Scheme 6.3 A synthetic scheme to truxene ligands featuring more interesting substituents.

6.4 Exploring more example of quaternary MOFs

Quaternary MOFs are still underdeveloped with the only existing examples being the MUF-7 family, MUF-77 family, UMCM-10-12[214] and PCN-700.[215] It would be interesting to explore more quaternary MOFs. Two directions can be considered to achieve this goal: 1) Isoreticular expansion or contraction of known quaternary frameworks. It would probably be necessary to keep the relative length ratio of the multiple ligands constant to achieve this. 2) Explore ligands with different geometries, such as four-connected square-planar or tetrahedral ligands. Metal clusters featuring different connectivities may also be considered.

6.5 Higher order MC-MOFs

One exciting target would be quinary or higher order MC-MOFs (Scheme 6.4). This would be an ambitious target because the number of competing phases will increase greater than exponentially, as described in Chapter 2. *In silico* methods could assist in identifying feasible frameworks for targeting in the laboratory.[168]

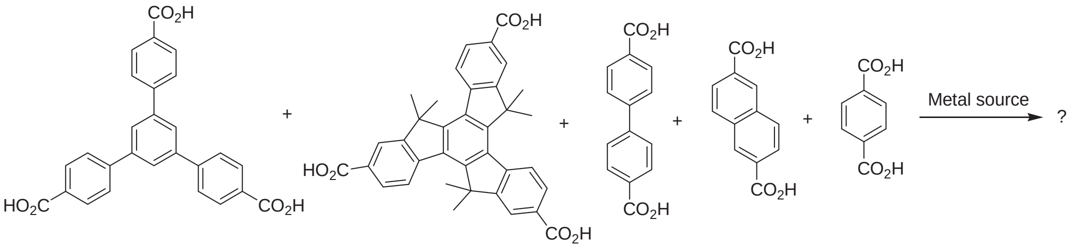

Scheme 6.4 Will this ligand set form a senary MC-MOF comprising five distinct ligands?

6.6 Applications

The exceptional water stability of MUF-77 family promises their real-world applications. First, they could be used as adsorbents for ANG tanks. It is known that MOF-177, which is highly sensitive to water vapour, was used for methane storage in a prototype vehicle. MUF-77-methyl has a very similar porosity to MOF-177 so it could be potentially be employed as a longer-lived adsorbent for these fuel tanks. Second, they can be integrated into mixed-matrix membranes for gas separation applications under humid conditions. For better CO_2 separation performance, a core-shell MUF-77 variant comprising two truxene ligands, as shown in Scheme 6.5, could be fabricated. Truxene ligands with allyl groups could be used for a shell layer to polymerize with membrane materials and provide a goof MOF-matrix interface, and the polyethylene glycol functionalized truxene ligand may form a core with highly selective CO_2 adsorption properties. Third, truxene has very interesting photoluminescence properties[274] and related applications of the MUF-77 family would be worth investigating.

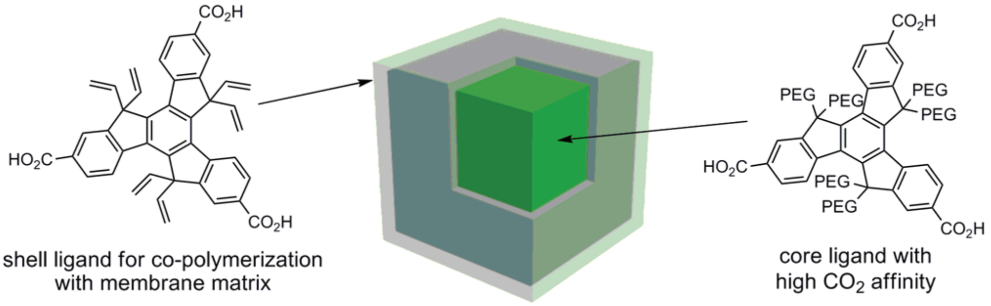

Scheme 6.5 Proposed synthesis of core-shell MUF-77 crystals that can be integrated into mixed-matrix membranes for flue gas treatment.

References

1 D. J. Lun, G. I. N. Waterhouse & S. G. Telfer; A General Thermolabile Protecting Group Strategy for Organocatalytic Metal−Organic Frameworks. *J. Am. Chem. Soc.* **2011**, *133*, 5806-5809.

2 R. Batten Stuart, R. Champness Neil, X.-M. Chen, J. Garcia-Martinez, S. Kitagawa, L. Öhrström, M. O'Keeffe, M. Paik Suh & J. Reedijk. in *Pure Appl. Chem.* Vol. 85 1715 (2013).

3 H. Li, M. Eddaoudi, M. O'Keeffe & O. M. Yaghi; Design and synthesis of an exceptionally stable and highly porous metal-organic framework. *Nature* **1999**, *402*, 276-279.

4 S. R. Caskey, A. G. Wong-Foy & A. J. Matzger; Dramatic Tuning of Carbon Dioxide Uptake via Metal Substitution in a Coordination Polymer with Cylindrical Pores. *J. Am. Chem. Soc.* **2008**, *130*, 10870-10871.

5 J. A. Mason, K. Sumida, Z. R. Herm, R. Krishna & J. R. Long; Evaluating metal-organic frameworks for post-combustion carbon dioxide capture via temperature swing adsorption. *Energy Environ. Sci.* **2011**, *4*, 3030-3040.

6 T. M. McDonald, J. A. Mason, X. Kong, E. D. Bloch, D. Gygi, A. Dani, V. Crocella, F. Giordanino, S. O. Odoh, W. S. Drisdell, B. Vlaisavljevich, A. L. Dzubak, R. Poloni, S. K. Schnell, N. Planas, K. Lee, T. Pascal, L. F. Wan, D. Prendergast, J. B. Neaton, B. Smit, J. B. Kortright, L. Gagliardi, S. Bordiga, J. A. Reimer & J. R. Long; Cooperative insertion of CO2 in diamine-appended metal-organic frameworks. *Nature* **2015**, *519*, 303-308.

7 S. S.-Y. Chui, S. M.-F. Lo, J. P. H. Charmant, A. G. Orpen & I. D. Williams; A Chemically Functionalizable Nanoporous Material $[Cu_3(TMA)_2(H2O)_3]_n$. *Science* **1999**, *283*, 1148-1150.

8 G. Férey, C. Mellot-Draznieks, C. Serre, F. Millange, J. Dutour, S. Surblé & I. Margiolaki; A Chromium Terephthalate-Based Solid with Unusually Large Pore Volumes and Surface Area. *Science* **2005**, *309*, 2040-2042.

9 J. H. Cavka, S. Jakobsen, U. Olsbye, N. Guillou, C. Lamberti, S. Bordiga & K. P. Lillerud; A New Zirconium Inorganic Building Brick Forming Metal Organic Frameworks with Exceptional Stability. *J. Am. Chem. Soc.* **2008**, *130*, 13850-13851.

10 C. Serre, C. Mellot-Draznieks, S. Surblé, N. Audebrand, Y. Filinchuk & G. Férey; Role of Solvent-Host Interactions That Lead to Very Large Swelling of Hybrid Frameworks. *Science* **2007**, *315*, 1828-1831.

11 A. Dutta, K. Koh, A. G. Wong-Foy & A. J. Matzger; Porous Solids Arising from Synergistic and Competing Modes of Assembly: Combining Coordination Chemistry and Covalent Bond Formation. *Angew. Chem. Int. Ed.* **2015**, *54*, 3983-3987.

12 H. K. Chae, D. Y. Siberio-Perez, J. Kim, Y. Go, M. Eddaoudi, A. J. Matzger, M. O'Keeffe & O. M. Yaghi; A route to high surface area, porosity and inclusion of large molecules in crystals. *Nature* **2004**, *427*, 523-527.

13 S. R. Caskey, A. G. Wong-Foy & A. J. Matzger; Phase Selection and Discovery among Five Assembly Modes in a Coordination Polymerization. *Inorg. Chem.* **2008**, *47*, 7751-7756.

14 H. J. Buser, D. Schwarzenbach, W. Petter & A. Ludi; The crystal structure of Prussian Blue: Fe4[Fe(CN)6]3.xH2O. *Inorg. Chem.* **1977**, *16*, 2704-2710.

15 B. F. Hoskins & R. Robson; Design and construction of a new class of scaffolding-like materials comprising infinite polymeric frameworks of 3D-linked molecular rods. A reappraisal of the zinc cyanide and cadmium cyanide structures and the synthesis and structure of the diamond-related frameworks $[N(CH_3)_4][Cu(I)Zn(II)(CN)4]$ and CuI[4,4',4'',4'''-tetracyanotetraphenylmethane]$BF_4 \bullet xC_6H_5NO_2$. *J. Am. Chem. Soc.* **1990**, *112*, 1546-1554.

16 O. M. Yaghi & H. Li; Hydrothermal Synthesis of a Metal-Organic Framework Containing Large Rectangular Channels. *J. Am. Chem. Soc.* **1995**, *117*, 10401-10402.

17 O. M. Yaghi, G. Li & H. Li; Selective binding and removal of guests in a microporous metal-organic framework. *Nature* **1995**, *378*, 703-706.

18 H. Koyama & Y. Saito; The Crystal Structure of Zinc Oxyacetate, $Zn_4O(CH_3COO)_6$. *Bull. Chem. Soc. Jpn.* **1954**, *27*, 112-114.

19 S. Brunauer, P. H. Emmett & E. Teller; Adsorption of Gases in Multimolecular Layers. *J. Am. Chem. Soc.* **1938**, *60*, 309-319.

20 S. S. Kaye, A. Dailly, O. M. Yaghi & J. R. Long; Impact of Preparation and Handling on the Hydrogen Storage Properties of $Zn_4O(1,4\text{-benzenedicarboxylate})_3$ (MOF-5). *J. Am. Chem. Soc.* **2007**, *129*, 14176-14177.

21 M. O’Keeffe, M. A. Peskov, S. J. Ramsden & O. M. Yaghi; The Reticular Chemistry Structure Resource (RCSR) Database of, and Symbols for, Crystal Nets. *Acc. Chem. Res.* **2008**, *41*, 1782-1789.

22 Y. Peng, V. Krungleviciute, I. Eryazici, J. T. Hupp, O. K. Farha & T. Yildirim; Methane Storage in Metal–Organic Frameworks: Current Records, Surprise Findings, and Challenges. *J. Am. Chem. Soc.* **2013**, *135*, 11887-11894.

23 Z. Wang & S. M. Cohen; Postsynthetic Covalent Modification of a Neutral Metal−Organic Framework. *J. Am. Chem. Soc.* **2007**, *129*, 12368-12369.

24 S. Ma, D. Sun, J. M. Simmons, C. D. Collier, D. Yuan & H.-C. Zhou; Metal-Organic Framework from an Anthracene Derivative Containing Nanoscopic Cages Exhibiting High Methane Uptake. *J. Am. Chem. Soc.* **2007**, *130*, 1012-1016.

25 P. D. C. Dietzel, B. Panella, M. Hirscher, R. Blom & H. Fjellvag; Hydrogen adsorption in a nickel based coordination polymer with open metal sites in the cylindrical cavities of the desolvated framework. *Chem. Commun.* **2006**, 959-961.

26 H. Wu, W. Zhou & T. Yildirim; High-Capacity Methane Storage in Metal−Organic Frameworks M_2(dhtp): The Important Role of Open Metal Sites. *J. Am. Chem. Soc.* **2009**, *131*, 4995-5000.

27 T. M. McDonald, W. R. Lee, J. A. Mason, B. M. Wiers, C. S. Hong & J. R. Long; Capture of Carbon Dioxide from Air and Flue Gas in the Alkylamine-Appended Metal–Organic Framework mmen-Mg_2(dobpdc). *J. Am. Chem. Soc.* **2012**, *134*, 7056-7065.

28 Y. Lin, Q. Yan, C. Kong & L. Chen; Polyethyleneimine Incorporated Metal-Organic Frameworks Adsorbent for Highly Selective CO2 Capture. *Sci. Rep.* **2013**, *3*, 1859.

29 Q. Yan, Y. Lin, C. Kong & L. Chen; Remarkable CO_2/CH_4 selectivity and CO_2 adsorption capacity exhibited by polyamine-decorated metal-organic framework adsorbents. *Chem. Commun.* **2013**, *49*, 6873-6875.

30 M. Banerjee, S. Das, M. Yoon, H. J. Choi, M. H. Hyun, S. M. Park, G. Seo & K. Kim; Postsynthetic Modification Switches an Achiral Framework to Catalytically Active Homochiral Metal−Organic Porous Materials. *J. Am. Chem. Soc.* **2009**, *131*, 7524-7525.

31 Z. Wang & S. M. Cohen; Postsynthetic modification of metal-organic frameworks. *Chem. Soc. Rev.* **2009**, *38*, 1315-1329.

32 R. K. Deshpande, J. L. Minnaar & S. G. Telfer; Thermolabile Groups in Metal–Organic Frameworks: Suppression of Network Interpenetration, Post-Synthetic Cavity Expansion, and Protection of Reactive Functional Groups. *Angew. Chem. Int. Ed.* **2010**, *49*, 4598-4602.

33 A. S. Gupta, R. K. Deshpande, L. Liu, G. I. N. Waterhouse & S. G. Telfer; Porosity in metal-organic frameworks following thermolytic postsynthetic deprotection: gas sorption, dye uptake and covalent derivatisation. *CrystEngComm* **2012**, *14*, 5701-5704.

34 K. K. Tanabe, C. A. Allen & S. M. Cohen; Photochemical Activation of a Metal–Organic Framework to Reveal Functionality. *Angew. Chem.* **2010**, *122*, 9924-9927.

35 R. K. Deshpande, G. I. N. Waterhouse, G. B. Jameson & S. G. Telfer; Photolabile protecting groups in metal-organic frameworks: preventing interpenetration and masking functional groups. *Chem. Commun.* **2012**, *48*, 1574-1576.

36 C. A. Allen & S. M. Cohen; Near-UV photo-induced modification in isoreticular metal-organic frameworks. *J. Mater. Chem.* **2012**, *22*, 10188-10194.

37 M. Kim, J. F. Cahill, H. Fei, K. A. Prather & S. M. Cohen; Postsynthetic Ligand and Cation Exchange in Robust Metal–Organic Frameworks. *J. Am. Chem. Soc.* **2012**, *134*, 18082-18088.

38 M. Kim, J. F. Cahill, Y. Su, K. A. Prather & S. M. Cohen; Postsynthetic ligand exchange as a route to functionalization of 'inert' metal-organic frameworks. *Chem. Sci.* **2012**, *3*, 126-130.

39 C. Hon Lau, R. Babarao & M. R. Hill; A route to drastic increase of CO2 uptake in Zr metal organic framework UiO-66. *Chem. Commun.* **2013**, *49*, 3634-3636.

40 O. Karagiaridi, W. Bury, A. A. Sarjeant, C. L. Stern, O. K. Farha & J. T. Hupp; Synthesis and characterization of isostructural cadmium zeolitic imidazolate frameworks via solvent-assisted linker exchange. *Chem. Sci.* **2012**, *3*, 3256-3260.

41 S. Takaishi, E. J. DeMarco, M. J. Pellin, O. K. Farha & J. T. Hupp; Solvent-assisted linker exchange (SALE) and post-assembly metallation in porphyrinic metal-organic framework materials. *Chem. Sci.* **2013**, *4*, 1509-1513.

42 C. J. Doonan, W. Morris, H. Furukawa & O. M. Yaghi; Isoreticular Metalation of Metal−Organic Frameworks. *J. Am. Chem. Soc.* **2009**, *131*, 9492-9493.

43 W. M. Bloch, A. Burgun, C. J. Coghlan, R. Lee, M. L. Coote, C. J. Doonan & C. J. Sumby; Capturing snapshots of post-synthetic metallation chemistry in metal–organic frameworks. *Nat Chem* **2014**, *6*, 906-912.

44 J. D. Evans, C. J. Sumby & C. J. Doonan; Post-synthetic metalation of metal-organic frameworks. *Chem. Soc. Rev.* **2014**, *43*, 5933-5951.

45 J. A. Mason, M. Veenstra & J. R. Long; Evaluating metal-organic frameworks for natural gas storage. *Chem. Sci.* **2014**, *5*, 32-51.

46 A. A. Talin, A. Centrone, A. C. Ford, M. E. Foster, V. Stavila, P. Haney, R. A. Kinney, V. Szalai, F. El Gabaly, H. P. Yoon, F. Léonard & M. D. Allendorf; Tunable Electrical Conductivity in Metal-Organic Framework Thin-Film Devices. *Science* **2014**, *343*, 66-69.

47 W.-Y. Gao, Y. Chen, Y. Niu, K. Williams, L. Cash, P. J. Perez, L. Wojtas, J. Cai, Y.-S. Chen & S. Ma; Crystal Engineering of an nbo Topology Metal–Organic Framework for Chemical Fixation of CO_2 under Ambient Conditions. *Angew. Chem. Int. Ed.* **2014**, *53*, 2615-2619.

48 O. Kozachuk, I. Luz, F. X. Llabrés i Xamena, H. Noei, M. Kauer, H. B. Albada, E. D. Bloch, B. Marler, Y. Wang, M. Muhler & R. A. Fischer; Multifunctional, Defect-Engineered Metal–Organic Frameworks with Ruthenium Centers: Sorption and Catalytic Properties. *Angew. Chem. Int. Ed.* **2014**, *53*, 7058-7062.

49 C. R. Wade & M. Dinca; Investigation of the synthesis, activation, and isosteric heats of CO2 adsorption of the isostructural series of metal-organic frameworks $M_3(BTC)_2$ (M = Cr, Fe, Ni, Cu, Mo, Ru). *Dalton Trans.* **2012**, *41*, 7931-7938.

50 K. A. Cychosz & A. J. Matzger; Water Stability of Microporous Coordination Polymers and the Adsorption of Pharmaceuticals from Water. *Langmuir* **2010**, *26*, 17198-17202.

51 O. M. Yaghi, C. E. Davis, G. Li & H. Li; Selective Guest Binding by Tailored Channels in a 3-D Porous Zinc(II)−Benzenetricarboxylate Network. *J. Am. Chem. Soc.* **1997**, *119*, 2861-2868.

52 H. Li, C. E. Davis, T. L. Groy, D. G. Kelley & O. M. Yaghi; Coordinatively Unsaturated Metal Centers in the Extended Porous Framework of $Zn_3(BDC)_3\cdot 6CH_3OH$ (BDC = 1,4-Benzenedicarboxylate). *J. Am. Chem. Soc.* **1998**, *120*, 2186-2187.

53 H. Li, M. Eddaoudi, T. L. Groy & O. M. Yaghi; Establishing Microporosity in Open Metal−Organic Frameworks: Gas Sorption Isotherms for Zn(BDC) (BDC = 1,4-Benzenedicarboxylate). *J. Am. Chem. Soc.* **1998**, *120*, 8571-8572.

54 M. Eddaoudi, J. Kim, N. Rosi, D. Vodak, J. Wachter, M. O'Keeffe & O. M. Yaghi; Systematic Design of Pore Size and Functionality in Isoreticular MOFs and Their Application in Methane Storage. *Science* **2002**, *295*, 469-472.

55 K. Koh, A. G. Wong-Foy & A. J. Matzger; A Crystalline Mesoporous Coordination Copolymer with High Microporosity. *Angew. Chem. Int. Ed.* **2008**, *47*, 677-680.

56 H. Furukawa, N. Ko, Y. B. Go, N. Aratani, S. B. Choi, E. Choi, A. Ö. Yazaydin, R. Q. Snurr, M. O’Keeffe, J. Kim & O. M. Yaghi; Ultrahigh Porosity in Metal-Organic Frameworks. *Science* **2010**, *329*, 424-428.

57 H. Furukawa, K. E. Cordova, M. O’Keeffe & O. M. Yaghi; The Chemistry and Applications of Metal-Organic Frameworks. *Science* **2013**, *341*, 974.

58 S. Hausdorf, J. Wagler, R. Moβig & F. O. R. L. Mertens; Proton and Water Activity-Controlled Structure Formation in Zinc Carboxylate-Based Metal Organic Frameworks. *J. Phys. Chem. A* **2008**, *112*, 7567-7576.

59 O. M. Yaghi, M. O'Keeffe, N. W. Ockwig, H. K. Chae, M. Eddaoudi & J. Kim; Reticular synthesis and the design of new materials. *Nature* **2003**, *423*, 705-714.

60 L. Bromberg, Y. Diao, H. Wu, S. A. Speakman & T. A. Hatton; Chromium(III) Terephthalate Metal Organic Framework (MIL-101): HF-Free Synthesis, Structure, Polyoxometalate Composites, and Catalytic Properties. *Chem. Mater.* **2012**, *24*, 1664-1675.

61 G. Férey, C. Serre, C. Mellot-Draznieks, F. Millange, S. Surblé, J. Dutour & I. Margiolaki; A Hybrid Solid with Giant Pores Prepared by a Combination of Targeted Chemistry, Simulation, and Powder Diffraction. *Angew. Chem. Int. Ed.* **2004**, *43*, 6296-6301.

62 Q. Fang, G. Zhu, M. Xue, J. Sun, Y. Wei, S. Qiu & R. Xu; A Metal–Organic Framework with the Zeolite MTN Topology Containing Large Cages of Volume 2.5 nm3 *Angew. Chem. Int. Ed.* **2005**, *44*, 3845-3848.

63 M. O’Keeffe & O. M. Yaghi; Deconstructing the Crystal Structures of Metal–Organic Frameworks and Related Materials into Their Underlying Nets. *Chem. Rev.* **2012**, *112*, 675-702.

64 P. Küsgens, M. Rose, I. Senkovska, H. Fröde, A. Henschel, S. Siegle & S. Kaskel; Characterization of metal-organic frameworks by water adsorption. *Microporous Mesoporous Mater.* **2009**, *120*, 325-330.

65 D.-Y. Hong, Y. K. Hwang, C. Serre, G. Férey & J.-S. Chang; Porous Chromium Terephthalate MIL-101 with Coordinatively Unsaturated Sites: Surface Functionalization, Encapsulation, Sorption and Catalysis. *Adv. Funct. Mater.* **2009**, *19*, 1537-1552.

66 Y.-K. Seo, J. W. Yoon, J. S. Lee, Y. K. Hwang, C.-H. Jun, J.-S. Chang, S. Wuttke, P. Bazin, A. Vimont, M. Daturi, S. Bourrelly, P. L. Llewellyn, P. Horcajada, C. Serre & G. Férey; Energy-Efficient Dehumidification over Hierachically Porous Metal–Organic Frameworks as Advanced Water Adsorbents. *Adv. Mater.* **2012**, *24*, 806-810.

67 J. Ehrenmann, S. K. Henninger & C. Janiak; Water Adsorption Characteristics of MIL-101 for Heat-Transformation Applications of MOFs. *Eur. J. Inorg. Chem.* **2011**, *2011*, 471-474.

68 Y. Hu, C. Song, J. Liao, Z. Huang & G. Li; Water stable metal-organic framework packed microcolumn for online sorptive extraction and direct analysis of naproxen and its metabolite from urine sample. *J. Chromatogr. A* **2013**, *1294*, 17-24.

69 G. D. Pirngruber, L. Hamon, S. Bourrelly, P. L. Llewellyn, E. Lenoir, V. Guillerm, C. Serre & T. Devic; A Method for Screening the Potential of MOFs as CO2 Adsorbents in Pressure Swing Adsorption Processes. *ChemSusChem* **2012**, *5*, 762-776.

70 G. Akiyama, R. Matsuda & S. Kitagawa; Highly Porous and Stable Coordination Polymers as Water Sorption Materials. *Chem. Lett.* **2010**, *39*, 360-361.

71 G. Akiyama, R. Matsuda, H. Sato, M. Takata & S. Kitagawa; Cellulose Hydrolysis by a New Porous Coordination Polymer Decorated with Sulfonic Acid Functional Groups. *Adv. Mater.* **2011**, *23*, 3294-3297.

72 B. Li, K. Leng, Y. Zhang, J. J. Dynes, J. Wang, Y. Hu, D. Ma, Z. Shi, L. Zhu, D. Zhang, Y. Sun, M. Chrzanowski & S. Ma; Metal–Organic Framework Based upon the Synergy of a Brønsted Acid Framework and Lewis Acid Centers as a Highly Efficient Heterogeneous Catalyst for Fixed-Bed Reactions. *J. Am. Chem. Soc.* **2015**, *137*, 4243-4248.

73 M. Yoon, R. Srirambalaji & K. Kim; Homochiral metal-organic frameworks for asymmetric heterogeneous catalysis. *Chem. Rev.* **2012**, *112*, 1196-1231.

74 Y. Lin, H. Lin, H. Wang, Y. Suo, B. Li, C. Kong & L. Chen; Enhanced selective CO_2 adsorption on polyamine/MIL-101(Cr) composites. *J. Mater. Chem. A* **2014**, *2*, 14658-14665.

75 K. M. L. Taylor-Pashow, J. D. Rocca, Z. Xie, S. Tran & W. Lin; Postsynthetic Modifications of Iron-Carboxylate Nanoscale Metal−Organic Frameworks for Imaging and Drug Delivery. *J. Am. Chem. Soc.* **2009**, *131*, 14261-14263.

76 Y.-T. Li, K.-H. Cui, J. Li, J.-Q. Zhu, X. Wang & Y.-Q. Tian; The Giant Pore Metal-Organic Frameworks of Scandium Carboxylate with MIL-l00 and MIL-l01 Structures. *Chin. J. Inorg. Chem.* **2011**, *27*, 951-956.

77 S. Biswas, S. Couck, M. Grzywa, J. F. M. Denayer, D. Volkmer & P. Van Der Voort; Vanadium Analogues of Nonfunctionalized and Amino-Functionalized MOFs with MIL-101 Topology – Synthesis, Characterization, and Gas Sorption Properties. *Eur. J. Inorg. Chem.* **2012**, *2012*, 2481-2486.

78 A. C. McKinlay, R. E. Morris, P. Horcajada, G. Férey, R. Gref, P. Couvreur & C. Serre; BioMOFs: Metal–Organic Frameworks for Biological and Medical Applications. *Angew. Chem. Int. Ed.* **2010**, *49*, 6260-6266.

79 J. Della Rocca, D. Liu & W. Lin; Nanoscale Metal–Organic Frameworks for Biomedical Imaging and Drug Delivery. *Acc. Chem. Res.* **2011**, *44*, 957-968.

80 F. Jeremias, V. Lozan, S. K. Henninger & C. Janiak; Programming MOFs for water sorption: amino-functionalized MIL-125 and UiO-66 for heat transformation and heat storage applications. *Dalton Trans.* **2013**, *42*, 15967-15973.

81 N. C. Burtch, H. Jasuja & K. S. Walton; Water Stability and Adsorption in Metal–Organic Frameworks. *Chem. Rev.* **2014**, *114*, 10575-10612.

82 J. E. Mondloch, M. J. Katz, N. Planas, D. Semrouni, L. Gagliardi, J. T. Hupp & O. K. Farha; Are Zr_6-based MOFs water stable? Linker hydrolysis vs. capillary-force-driven channel collapse. *Chem. Commun.* **2014**, *50*, 8944-8946.

83 M. I. Gonzalez, E. D. Bloch, J. A. Mason, S. J. Teat & J. R. Long; Single-Crystal-to-Single-Crystal Metalation of a Metal–Organic Framework: A Route toward Structurally Well-Defined Catalysts. *Inorg. Chem.* **2015**, *54*, 2995-3005.

84 W. J. Phang, H. Jo, W. R. Lee, J. H. Song, K. Yoo, B. Kim & C. S. Hong; Superprotonic Conductivity of a UiO-66 Framework Functionalized with Sulfonic Acid Groups by Facile Postsynthetic Oxidation. *Angew. Chem. Int. Ed.* **2015**, *54*, 5142-5146.

85 S. Pullen, H. Fei, A. Orthaber, S. M. Cohen & S. Ott; Enhanced Photochemical Hydrogen Production by a Molecular Diiron Catalyst Incorporated into a Metal–Organic Framework. *J. Am. Chem. Soc.* **2013**, *135*, 16997-17003.

86 K. Manna, T. Zhang & W. Lin; Postsynthetic Metalation of Bipyridyl-Containing Metal–Organic Frameworks for Highly Efficient Catalytic Organic Transformations. *J. Am. Chem. Soc.* **2014**, *136*, 6566-6569.

87 J. Jiang, F. Gándara, Y.-B. Zhang, K. Na, O. M. Yaghi & W. G. Klemperer; Superacidity in Sulfated Metal–Organic Framework-808. *J. Am. Chem. Soc.* **2014**, *136*, 12844-12847.

88 T. C. Wang, W. Bury, D. A. Gómez-Gualdrón, N. A. Vermeulen, J. E. Mondloch, P. Deria, K. Zhang, P. Z. Moghadam, A. A. Sarjeant, R. Q. Snurr, J. F. Stoddart, J. T. Hupp & O. K. Farha; Ultrahigh Surface Area Zirconium MOFs and Insights into the Applicability of the BET Theory. *J. Am. Chem. Soc.* **2015**, *137*, 3585-3591.

89 J. Park, D. Feng & H.-C. Zhou; Structure-Assisted Functional Anchor Implantation in Robust Metal–Organic Frameworks with Ultralarge Pores. *J. Am. Chem. Soc.* **2015**, *137*, 1663-1672.

90 T.-F. Liu, D. Feng, Y.-P. Chen, L. Zou, M. Bosch, S. Yuan, Z. Wei, S. Fordham, K. Wang & H.-C. Zhou; Topology-Guided Design and Syntheses of Highly Stable Mesoporous Porphyrinic Zirconium Metal–Organic Frameworks with High Surface Area. *J. Am. Chem. Soc.* **2015**, *137*, 413-419.

91 D. Feng, Z.-Y. Gu, Y.-P. Chen, J. Park, Z. Wei, Y. Sun, M. Bosch, S. Yuan & H.-C. Zhou; A Highly Stable Porphyrinic Zirconium Metal–Organic Framework with shp-a Topology. *J. Am. Chem. Soc.* **2014**, *136*, 17714-17717.

92 Z. Wei, Z.-Y. Gu, R. K. Arvapally, Y.-P. Chen, R. N. McDougald, J. F. Ivy, A. A. Yakovenko, D. Feng, M. A. Omary & H.-C. Zhou; Rigidifying Fluorescent Linkers by Metal–Organic Framework Formation for Fluorescence Blue Shift and Quantum Yield Enhancement. *J. Am. Chem. Soc.* **2014**, *136*, 8269-8276.

93 D. Feng, W.-C. Chung, Z. Wei, Z.-Y. Gu, H.-L. Jiang, Y.-P. Chen, D. J. Darensbourg & H.-C. Zhou; Construction of Ultrastable Porphyrin Zr Metal–Organic Frameworks through Linker Elimination. *J. Am. Chem. Soc.* **2013**, *135*, 17105-17110.

94 S. B. Kalidindi, S. Nayak, M. E. Briggs, S. Jansat, A. P. Katsoulidis, G. J. Miller, J. E. Warren, D. Antypov, F. Corà, B. Slater, M. R. Prestly, C. Martí-Gastaldo & M. J. Rosseinsky; Chemical and Structural Stability of Zirconium-based Metal–Organic Frameworks with Large Three-Dimensional Pores by Linker Engineering. *Angew. Chem. Int. Ed.* **2015**, *54*, 221-226.

95 X.-C. Huang, Y.-Y. Lin, J.-P. Zhang & X.-M. Chen; Ligand-Directed Strategy for Zeolite-Type Metal–Organic Frameworks: Zinc(II) Imidazolates with Unusual Zeolitic Topologies. *Angew. Chem. Int. Ed.* **2006**, *45*, 1557-1559.

96 K. S. Park, Z. Ni, A. P. Côté, J. Y. Choi, R. Huang, F. J. Uribe-Romo, H. K. Chae, M. O’Keeffe & O. M. Yaghi; Exceptional chemical and thermal stability of zeolitic imidazolate frameworks. *PNAS* **2006**, *103*, 10186-10191.

97 Y. Pan, Y. Liu, G. Zeng, L. Zhao & Z. Lai; Rapid synthesis of zeolitic imidazolate framework-8 (ZIF-8) nanocrystals in an aqueous system. *Chem. Commun.* **2011**, *47*, 2071-2073.

98 N. L. Rosi, J. Kim, M. Eddaoudi, B. Chen, M. O'Keeffe & O. M. Yaghi; Rod Packings and Metal−Organic Frameworks Constructed from Rod-Shaped Secondary Building Units. *J. Am. Chem. Soc.* **2005**, *127*, 1504-1518.

99 H. Deng, S. Grunder, K. E. Cordova, C. Valente, H. Furukawa, M. Hmadeh, F. Gándara, A. C. Whalley, Z. Liu, S. Asahina, H. Kazumori, M. O’Keeffe, O. Terasaki, J. F. Stoddart & O. M. Yaghi; Large-Pore Apertures in a Series of Metal-Organic Frameworks. *Science* **2012**, *336*, 1018-1023.

100 P. D. C. Dietzel, Y. Morita, R. Blom & H. Fjellvåg; An In Situ High-Temperature Single-Crystal Investigation of a Dehydrated Metal–Organic Framework Compound and Field-Induced Magnetization of One-Dimensional Metal–Oxygen Chains. *Angew. Chem.* **2005**, *117*, 6512-6516.

101 W. Zhou, H. Wu & T. Yildirim; Enhanced H2 Adsorption in Isostructural Metal−Organic Frameworks with Open Metal Sites: Strong Dependence of the Binding Strength on Metal Ions. *J. Am. Chem. Soc.* **2008**, *130*, 15268-15269.

102 E. D. Bloch, L. J. Murray, W. L. Queen, S. Chavan, S. N. Maximoff, J. P. Bigi, R. Krishna, V. K. Peterson, F. Grandjean, G. J. Long, B. Smit, S. Bordiga, C. M. Brown & J. R. Long; Selective Binding of O_2 over N_2 in a Redox–Active Metal–Organic Framework with Open Iron(II) Coordination Sites. *J. Am. Chem. Soc.* **2011**, *133*, 14814-14822.

103 E. D. Bloch, W. L. Queen, R. Krishna, J. M. Zadrozny, C. M. Brown & J. R. Long; Hydrocarbon Separations in a Metal-Organic Framework with Open Iron(II) Coordination Sites. *Science* **2012**, *335*, 1606-1610.

104 D. J. Xiao, E. D. Bloch, J. A. Mason, W. L. Queen, M. R. Hudson, N. Planas, J. Borycz, A. L. Dzubak, P. Verma, K. Lee, F. Bonino, V. Crocellà, J. Yano, S. Bordiga, D. G. Truhlar, L. Gagliardi, C. M. Brown & J. R. Long; Oxidation of ethane to ethanol by N2O in a metal–organic framework with coordinatively unsaturated iron(II) sites. *Nat Chem* **2014**, *6*, 590-595.

105 L. J. Wang, H. Deng, H. Furukawa, F. Gándara, K. E. Cordova, D. Peri & O. M. Yaghi; Synthesis and Characterization of Metal–Organic Framework-74 Containing 2, 4, 6, 8, and 10 Different Metals. *Inorg. Chem.* **2014**, *53*, 5881-5883.

106 N. Planas, A. L. Dzubak, R. Poloni, L.-C. Lin, A. McManus, T. M. McDonald, J. B. Neaton, J. R. Long, B. Smit & L. Gagliardi; The Mechanism of Carbon Dioxide Adsorption in an Alkylamine-Functionalized Metal–Organic Framework. *J. Am. Chem. Soc.* **2013**, *135*, 7402-7405.

107 S. Hausdorf, F. Baitalow, J. Seidel & F. O. R. L. Mertens; Gaseous Species as Reaction Tracers in the Solvothermal Synthesis of the Zinc Oxide Terephthalate MOF-5. *J. Phys. Chem. A* **2007**, *111*, 4259-4266.

108 A. Schaate, P. Roy, A. Godt, J. Lippke, F. Waltz, M. Wiebcke & P. Behrens; Modulated Synthesis of Zr-Based Metal–Organic Frameworks: From Nano to Single Crystals. *Chem. Eur. J.* **2011**, *17*, 6643-6651.

109 H. Bux, F. Liang, Y. Li, J. Cravillon, M. Wiebcke & J. Caro; Zeolitic Imidazolate Framework Membrane with Molecular Sieving Properties by Microwave-Assisted Solvothermal Synthesis. *J. Am. Chem. Soc.* **2009**, *131*, 16000-16001.

110 P. J. Beldon, L. Fábián, R. S. Stein, A. Thirumurugan, A. K. Cheetham & T. Friščić; Rapid Room-Temperature Synthesis of Zeolitic Imidazolate Frameworks by Using Mechanochemistry. *Angew. Chem. Int. Ed.* **2010**, *49*, 9640-9643.

111 C. G. Carson, A. J. Brown, D. S. Sholl & S. Nair; Sonochemical Synthesis and Characterization of Submicrometer Crystals of the Metal–Organic Framework Cu[(hfipbb)(H_2hfipbb)$_{0.5}$]. *Cryst. Growth Des.* **2011**, *11*, 4505-4510.

112 M. Li & M. Dincă; Reductive Electrosynthesis of Crystalline Metal–Organic Frameworks. *J. Am. Chem. Soc.* **2011**, *133*, 12926-12929.

113 C. R. Wade, M. Li & M. Dincă; Facile Deposition of Multicolored Electrochromic Metal–Organic Framework Thin Films. *Angew. Chem. Int. Ed.* **2013**, *52*, 13377-13381.

114 C. Dey, T. Kundu, B. P. Biswal, A. Mallick & R. Banerjee; Crystalline metal-organic frameworks (MOFs): synthesis, structure and function. *Acta Crystallogr. Sect. B* **2014**, *70*, 3-10.

115 Cambridge Structural Database, last acceseed on 30/May/2015. http://www.ccdc.cam.ac.uk/SUPPORTANDRESOURCES/Support/Pages/SupportSolution.aspx?supportsolutionid=275

116 D. J. Tranchemontagne, J. L. Mendoza-Cortes, M. O'Keeffe & O. M. Yaghi; Secondary building units, nets and bonding in the chemistry of metal-organic frameworks. *Chem. Soc. Rev.* **2009**, *38*, 1257-1283.

117 D. N. Dybtsev, H. Chun & K. Kim; Rigid and Flexible: A Highly Porous Metal–Organic Framework with Unusual Guest-Dependent Dynamic Behavior. *Angew. Chem. Int. Ed.* **2004**, *43*, 5033-5036.

118 P. V. Dau, M. Kim, S. J. Garibay, F. H. L. Münch, C. E. Moore & S. M. Cohen; Single-Atom Ligand Changes Affect Breathing in an Extended Metal–Organic Framework. *Inorg. Chem.* **2012**, *51*, 5671-5676.

119 P. Nugent, Y. Belmabkhout, S. D. Burd, A. J. Cairns, R. Luebke, K. Forrest, T. Pham, S. Ma, B. Space, L. Wojtas, M. Eddaoudi & M. J. Zaworotko; Porous materials with optimal adsorption thermodynamics and kinetics for CO_2 separation. *Nature* **2013**, *495*, 80-84.

120 V. Colombo, C. Montoro, A. Maspero, G. Palmisano, N. Masciocchi, S. Galli, E. Barea & J. A. R. Navarro; Tuning the Adsorption Properties of Isoreticular Pyrazolate-Based Metal–Organic Frameworks through Ligand Modification. *J. Am. Chem. Soc.* **2012**, *134*, 12830-12843.

121 C. Y. Lee, O. K. Farha, B. J. Hong, A. A. Sarjeant, S. T. Nguyen & J. T. Hupp; Light-Harvesting Metal–Organic Frameworks (MOFs): Efficient Strut-to-Strut Energy Transfer in Bodipy and Porphyrin-Based MOFs. *J. Am. Chem. Soc.* **2011**, *133*, 15858-15861.

122 R. P. Davies, R. Less, P. D. Lickiss, K. Robertson & A. J. P. White; Structural Diversity in Metal−Organic Frameworks Built from Rigid Tetrahedral [Si(p-C6H4CO2)4]4− Struts. *Cryst. Growth Des.* **2010**, *10*, 4571-4581.

123 S. Wang, J. Wang, W. Cheng, X. Yang, Z. Zhang, Y. Xu, H. Liu, Y. Wu & M. Fang; A Zr metal-organic framework based on tetrakis(4-carboxyphenyl) silane and

factors affecting the hydrothermal stability of Zr-MOFs. *Dalton Trans.* **2015**, *44*, 8049-8061.

124 O. K. Farha, C. E. Wilmer, I. Eryazici, B. G. Hauser, P. A. Parilla, K. O’Neill, A. A. Sarjeant, S. T. Nguyen, R. Q. Snurr & J. T. Hupp; Designing Higher Surface Area Metal–Organic Frameworks: Are Triple Bonds Better Than Phenyls? *J. Am. Chem. Soc.* **2012**, *134*, 9860-9863.

125 Y.-X. Tan, Y.-P. He & J. Zhang; Tuning MOF Stability and Porosity via Adding Rigid Pillars. *Inorg. Chem.* **2012**, *51*, 9649-9654.

126 A. G. Wong-Foy, O. Lebel & A. J. Matzger; Porous Crystal Derived from a Tricarboxylate Linker with Two Distinct Binding Motifs. *J. Am. Chem. Soc.* **2007**, *129*, 15740-15741.

127 X. Lin, I. Telepeni, A. J. Blake, A. Dailly, C. M. Brown, J. M. Simmons, M. Zoppi, G. S. Walker, K. M. Thomas, T. J. Mays, P. Hubberstey, N. R. Champness & M. Schröder; High Capacity Hydrogen Adsorption in Cu(II) Tetracarboxylate Framework Materials: The Role of Pore Size, Ligand Functionalization, and Exposed Metal Sites. *J. Am. Chem. Soc.* **2009**, *131*, 2159-2171.

128 V. Guillerm, Ł. J. Weseliński, Y. Belmabkhout, A. J. Cairns, V. D'Elia, Ł. Wojtas, K. Adil & M. Eddaoudi; Discovery and introduction of a (3,18)-connected net as an ideal blueprint for the design of metal–organic frameworks. *Nat Chem* **2014**, *6*, 673-680.

129 H. Deng, C. J. Doonan, H. Furukawa, R. B. Ferreira, J. Towne, C. B. Knobler, B. Wang & O. M. Yaghi; Multiple Functional Groups of Varying Ratios in Metal-Organic Frameworks. *Science* **2010**, *327*, 846-850.

130 X. Kong, H. Deng, F. Yan, J. Kim, J. A. Swisher, B. Smit, O. M. Yaghi & J. A. Reimer; Mapping of Functional Groups in Metal-Organic Frameworks. *Science* **2013**, *341*, 882-885.

131 H. Chun, D. N. Dybtsev, H. Kim & K. Kim; Synthesis, X-ray Crystal Structures, and Gas Sorption Properties of Pillared Square Grid Nets Based on Paddle-Wheel Motifs: Implications for Hydrogen Storage in Porous Materials. *Chem. Eur. J.* **2005**, *11*, 3521-3529.

132 P. V. Dau & S. M. Cohen; A Bifunctional, Site-Isolated Metal–Organic Framework-Based Tandem Catalyst. *Inorg. Chem.* **2015**, *54*, 3134-3138.

133 W. Chen, J.-Y. Wang, C. Chen, Q. Yue, H.-M. Yuan, J.-S. Chen & S.-N. Wang; Photoluminescent Metal−Organic Polymer Constructed from Trimetallic Clusters and Mixed Carboxylates. *Inorg. Chem.* **2003**, *42*, 944-946.

134 K. Koh, A. G. Wong-Foy & A. J. Matzger; A Porous Coordination Copolymer with over 5000 m2/g BET Surface Area. *J. Am. Chem. Soc.* **2009**, *131*, 4184-4185.

135 N. Klein, I. Senkovska, K. Gedrich, U. Stoeck, A. Henschel, U. Mueller & S. Kaskel; A Mesoporous Metal–Organic Framework. *Angew. Chem. Int. Ed.* **2009**, *48*, 9954-9957.

136 K. Koh, A. G. Wong-Foy & A. J. Matzger; Coordination Copolymerization Mediated by $Zn_4O(CO_2R)_6$ Metal Clusters: a Balancing Act between Statistics and Geometry. *J. Am. Chem. Soc.* **2010**, *132*, 15005-15010.

137 R. Grunker, V. Bon, P. Muller, U. Stoeck, S. Krause, U. Mueller, I. Senkovska & S. Kaskel; A new metal-organic framework with ultra-high surface area. *Chem. Commun.* **2014**, *50*, 3450-3452.

138 Q. Yao, J. Su, O. Cheung, Q. Liu, N. Hedin & X. Zou; Interpenetrated metal-organic frameworks and their uptake of CO2 at relatively low pressures. *J. Mater. Chem.* **2012**, *22*, 10345-10351.

139 K. Koh, J. D. Van Oosterhout, S. Roy, A. G. Wong-Foy & A. J. Matzger; Exceptional surface area from coordination copolymers derived from two linear linkers of differing lengths. *Chem. Sci.* **2012**, *3*, 2429-2432.

140 D. Kim & M. S. Lah; Metal-organic framework with two different types of rigid triscarboxylates: net topology and gas sorption behaviour. *CrystEngComm* **2013**, *15*, 9491-9498.

141 L. E. Kreno, K. Leong, O. K. Farha, M. Allendorf, R. P. Van Duyne & J. T. Hupp; Metal–Organic Framework Materials as Chemical Sensors. *Chem. Rev.* **2012**, *112*, 1105-1125.

142 C. Wang, T. Zhang & W. Lin; Rational Synthesis of Noncentrosymmetric Metal–Organic Frameworks for Second-Order Nonlinear Optics. *Chem. Rev.* **2012**, *112*, 1084-1104.

143 T. C. Narayan, T. Miyakai, S. Seki & M. Dincă; High Charge Mobility in a Tetrathiafulvalene-Based Microporous Metal–Organic Framework. *J. Am. Chem. Soc.* **2012**, *134*, 12932-12935.

144 D. Sheberla, L. Sun, M. A. Blood-Forsythe, S. Er, C. R. Wade, C. K. Brozek, A. Aspuru-Guzik & M. Dincă; High Electrical Conductivity in Ni_3(2,3,6,7,10,11-hexaiminotriphenylene)$_2$, a Semiconducting Metal–Organic Graphene Analogue. *J. Am. Chem. Soc.* **2014**, *136*, 8859-8862.

145 S. S. Park, E. R. Hontz, L. Sun, C. H. Hendon, A. Walsh, T. Van Voorhis & M. Dincă; Cation-Dependent Intrinsic Electrical Conductivity in Isostructural Tetrathiafulvalene-Based Microporous Metal–Organic Frameworks. *J. Am. Chem. Soc.* **2015**, *137*, 1774-1777.

146 M. G. Campbell, D. Sheberla, S. F. Liu, T. M. Swager & M. Dincă; Cu3(hexaiminotriphenylene)2: An Electrically Conductive 2D Metal–Organic Framework for Chemiresistive Sensing. *Angew. Chem. Int. Ed.* **2015**, *54*, 4349-4352.

147 L. Sun, C. H. Hendon, M. A. Minier, A. Walsh & M. Dincă; Million-Fold Electrical Conductivity Enhancement in Fe_2(DEBDC) versus Mn_2(DEBDC) (E = S, O). *J. Am. Chem. Soc.* **2015**, *137*, 6164-6167.

148 S. Bureekaew, S. Horike, M. Higuchi, M. Mizuno, T. Kawamura, D. Tanaka, N. Yanai & S. Kitagawa; One-dimensional imidazole aggregate in aluminium porous coordination polymers with high proton conductivity. *Nat Mater* **2009**, *8*, 831-836.

149 M. Sadakiyo, T. Yamada & H. Kitagawa; Rational Designs for Highly Proton-Conductive Metal−Organic Frameworks. *J. Am. Chem. Soc.* **2009**, *131*, 9906-9907.

150 S. Tominaka, F.-X. Coudert, T. D. Dao, T. Nagao & A. K. Cheetham; Insulator-to-Proton-Conductor Transition in a Dense Metal–Organic Framework. *J. Am. Chem. Soc.* **2015**, *137*, 6428-6431.

151 D. Wu, Z. Guo, X. Yin, Q. Pang, B. Tu, L. Zhang, Y.-G. Wang & Q. Li; Metal–Organic Frameworks as Cathode Materials for Li–O2 Batteries. *Adv. Mater.* **2014**, *26*, 3258-3262.

152 V. Lykourinou, Y. Chen, X.-S. Wang, L. Meng, T. Hoang, L.-J. Ming, R. L. Musselman & S. Ma; Immobilization of MP-11 into a Mesoporous Metal–Organic Framework, MP-11@mesoMOF: A New Platform for Enzymatic Catalysis. *J. Am. Chem. Soc.* **2011**, *133*, 10382-10385.

153 P. Horcajada, C. Serre, M. Vallet-Regí, M. Sebban, F. Taulelle & G. Férey; Metal–Organic Frameworks as Efficient Materials for Drug Delivery. *Angew. Chem. Int. Ed.* **2006**, *45*, 5974-5978.

154 K. Lu, C. He & W. Lin; Nanoscale Metal–Organic Framework for Highly Effective Photodynamic Therapy of Resistant Head and Neck Cancer. *J. Am. Chem. Soc.* **2014**, *136*, 16712-16715.

155 J. R. Long & O. M. Yaghi; The pervasive chemistry of metal-organic frameworks. *Chem. Soc. Rev.* **2009**, *38*, 1213-1214.

156 H.-C. Zhou & S. Kitagawa; Metal-Organic Frameworks (MOFs). *Chem. Soc. Rev.* **2014**, *43*, 5415-5418.

157 H.-C. Zhou, J. R. Long & O. M. Yaghi; Introduction to Metal–Organic Frameworks. *Chem. Rev.* **2012**, *112*, 673-674.

158 J.-R. Li, R. J. Kuppler & H.-C. Zhou; Selective gas adsorption and separation in metal-organic frameworks. *Chem. Soc. Rev.* **2009**, *38*, 1477-1504.

159 K. Sumida, D. L. Rogow, J. A. Mason, T. M. McDonald, E. D. Bloch, Z. R. Herm, T. H. Bae & J. R. Long; Carbon dioxide capture in metal-organic frameworks. *Chem. Rev.* **2012**, *112*, 724-781.

160 L. J. Murray, M. Dinca & J. R. Long; Hydrogen storage in metal-organic frameworks. *Chem. Soc. Rev.* **2009**, *38*, 1294-1314.

161 K. Konstas, T. Osl, Y. Yang, M. Batten, N. Burke, A. J. Hill & M. R. Hill; Methane storage in metal organic frameworks. *J. Mater. Chem.* **2012**, *22*, 16698-16708.

162 http://www.emercedesbenz.com/autos/mercedes-benz/concept-vehicles/mercedes-benz-f125-research-vehicle-technology/ Last accessed on 08/Jun/2015

163 M. Peplow; Materials science: The hole story. *Nature* **2015**, *520*, 148-150.

164 Thermophysical Properties of Fluid Systems, last accessed 3/Jun/2015. http://webbook.nist.gov/chemistry/fluid/

165 M. Kondo, T. Yoshitomi, H. Matsuzaka, S. Kitagawa & K. Seki; Three-Dimensional Framework with Channeling Cavities for Small Molecules: {[M2(4, 4′-bpy)3(NO3)4]·xH2O}n (M Co, Ni, Zn). *Angew. Chem. Int. Ed. Engl.* **1997**, *36*, 1725-1727.

166 C. E. Wilmer, O. K. Farha, T. Yildirim, I. Eryazici, V. Krungleviciute, A. A. Sarjeant, R. Q. Snurr & J. T. Hupp; Gram-scale, high-yield synthesis of a robust metal-organic framework for storing methane and other gases. *Energy Environ. Sci.* **2013**, *6*, 1158-1163.

167 Y. Yan, M. Suyetin, E. Bichoutskaia, A. J. Blake, D. R. Allan, S. A. Barnett & M. Schroder; Modulating the packing of [Cu24(isophthalate)24] cuboctahedra in a triazole-containing metal-organic polyhedral framework. *Chem. Sci.* **2013**, *4*, 1731-1736.

168 C. E. Wilmer, M. Leaf, C. Y. Lee, O. K. Farha, B. G. Hauser, J. T. Hupp & R. Q. Snurr; Large-scale screening of hypothetical metal–organic frameworks. *Nat Chem* **2012**, *4*, 83-89.

169 Y.-P. Chen, Y. Liu, D. Liu, M. Bosch & H.-C. Zhou; Direct Measurement of Adsorbed Gas Redistribution in Metal–Organic Frameworks. *J. Am. Chem. Soc.* **2015**, *137*, 2919-2930.

170 F. Gándara, H. Furukawa, S. Lee & O. M. Yaghi; High Methane Storage Capacity in Aluminum Metal–Organic Frameworks. *J. Am. Chem. Soc.* **2014**, *136*, 5271-5274.

171 https://www.iea.org/publications/freepublications/publication/CO2EmissionsFromFuelCombustionHighlights2014.pdf

172 T. Li, J. E. Sullivan & N. L. Rosi; Design and Preparation of a Core–Shell Metal–Organic Framework for Selective CO2 Capture. *J. Am. Chem. Soc.* **2013**, *135*, 9984-9987.

173 S. Yang, J. Sun, A. J. Ramirez-Cuesta, S. K. Callear, I. F. DavidWilliam, D. P. Anderson, R. Newby, A. J. Blake, J. E. Parker, C. C. Tang & M. Schröder; Selectivity and direct visualization of carbon dioxide and sulfur dioxide in a decorated porous host. *Nat Chem* **2012**, *4*, 887-894.

174 R. T. Yang; *Gas Separation by Adsorption Processes*. (Elsevier Science, 2013).

175 A. L. Myers & J. M. Prausnitz; Thermodynamics of mixed-gas adsorption. *AlChE J.* **1965**, *11*, 121-127.

176 J. Duan, W. Jin & R. Krishna; Natural Gas Purification Using a Porous Coordination Polymer with Water and Chemical Stability. *Inorg. Chem.* **2015**, *54*, 4279-4284.

177 Z. R. Herm, B. M. Wiers, J. A. Mason, J. M. van Baten, M. R. Hudson, P. Zajdel, C. M. Brown, N. Masciocchi, R. Krishna & J. R. Long; Separation of Hexane Isomers in a Metal-Organic Framework with Triangular Channels. *Science* **2013**, *340*, 960-964.

178 J. A. Hogendoorn, W. P. M. van Swaaij & G. F. Versteeg; The absorption of carbon monoxide in COSORB solutions: absorption rate and capacity. *Chem. Eng. Bio. Eng. J.* **1995**, *59*, 243-252.

179 H. Sato, W. Kosaka, R. Matsuda, A. Hori, Y. Hijikata, R. V. Belosludov, S. Sakaki, M. Takata & S. Kitagawa; Self-Accelerating CO Sorption in a Soft Nanoporous Crystal. *Science* **2014**, *343*, 167-170.

180 Y. Inokuma, S. Yoshioka, J. Ariyoshi, T. Arai, Y. Hitora, K. Takada, S. Matsunaga, K. Rissanen & M. Fujita; X-ray analysis on the nanogram to microgram scale using porous complexes. *Nature* **2013**, *495*, 461-466.

181 Y. Inokuma, S. Yoshioka, J. Ariyoshi, T. Arai & M. Fujita; Preparation and guest-uptake protocol for a porous complex useful for 'crystal-free' crystallography. *Nat. Protocols* **2014**, *9*, 246-252.

182 C. Montoro, F. Linares, E. Quartapelle Procopio, I. Senkovska, S. Kaskel, S. Galli, N. Masciocchi, E. Barea & J. A. R. Navarro; Capture of Nerve Agents and Mustard Gas Analogues by Hydrophobic Robust MOF-5 Type Metal–Organic Frameworks. *J. Am. Chem. Soc.* **2011**, *133*, 11888-11891.

183 N. M. Padial, E. Quartapelle Procopio, C. Montoro, E. López, J. E. Oltra, V. Colombo, A. Maspero, N. Masciocchi, S. Galli, I. Senkovska, S. Kaskel, E. Barea & J. A. R. Navarro; Highly Hydrophobic Isoreticular Porous Metal–Organic Frameworks for the Capture of Harmful Volatile Organic Compounds. *Angew. Chem. Int. Ed.* **2013**, *52*, 8290-8294.

184 E. López-Maya, C. Montoro, L. M. Rodríguez-Albelo, S. D. Aznar Cervantes, A. A. Lozano-Pérez, J. L. Cenís, E. Barea & J. A. R. Navarro; Textile/Metal–Organic-Framework Composites as Self-Detoxifying Filters for Chemical-Warfare Agents. *Angew. Chem. Int. Ed.* **2015**, *54*, 6790-6794.

185 J. E. Mondloch, M. J. Katz, W. C. Isley Iii, P. Ghosh, P. Liao, W. Bury, G. W. Wagner, M. G. Hall, J. B. DeCoste, G. W. Peterson, R. Q. Snurr, C. J. Cramer, J. T. Hupp & O. K. Farha; Destruction of chemical warfare agents using metal–organic frameworks. *Nat Mater* **2015**, *14*, 512-516.

186 S.-Y. Moon, Y. Liu, J. T. Hupp & O. K. Farha; Instantaneous Hydrolysis of Nerve-Agent Simulants with a Six-Connected Zirconium-Based Metal–Organic Framework. *Angew. Chem. Int. Ed.* **2015**, *54*, 6795-6799.

187 J. E. Mondloch, W. Bury, D. Fairen-Jimenez, S. Kwon, E. J. DeMarco, M. H. Weston, A. A. Sarjeant, S. T. Nguyen, P. C. Stair, R. Q. Snurr, O. K. Farha & J. T. Hupp; Vapor-Phase Metalation by Atomic Layer Deposition in a Metal–Organic Framework. *J. Am. Chem. Soc.* **2013**, *135*, 10294-10297.

188 H. Furukawa, F. Gándara, Y.-B. Zhang, J. Jiang, W. L. Queen, M. R. Hudson & O. M. Yaghi; Water Adsorption in Porous Metal–Organic Frameworks and Related Materials. *J. Am. Chem. Soc.* **2014**, *136*, 4369-4381.

189 R. C. Bansal & M. Goyal; *Activated carbon adsorption.* (Boca Raton : Dekker/CRC Press, 2005, 2005).

190 K. S. Walton & R. Q. Snurr; Applicability of the BET Method for Determining Surface Areas of Microporous Metal−Organic Frameworks. *J. Am. Chem. Soc.* **2007**, *129*, 8552-8556.

191 L. Liu, K. Konstas, M. R. Hill & S. G. Telfer; Programmed Pore Architectures in Modular Quaternary Metal–Organic Frameworks. *J. Am. Chem. Soc.* **2013**, *135*, 17731-17734.

192 L. Liu & S. G. Telfer; Systematic Ligand Modulation Enhances the Moisture Stability and Gas Sorption Characteristics of Quaternary Metal–Organic Frameworks. *J. Am. Chem. Soc.* **2015**, *137*, 3901-3909.

193 M. Dincǎ, A. Dailly, Y. Liu, C. M. Brown, D. A. Neumann & J. R. Long; Hydrogen Storage in a Microporous Metal−Organic Framework with Exposed Mn2+ Coordination Sites. *J. Am. Chem. Soc.* **2006**, *128*, 16876-16883.

194 T. Düren, F. Millange, G. Férey, K. S. Walton & R. Q. Snurr; Calculating Geometric Surface Areas as a Characterization Tool for Metal−Organic Frameworks. *J. Phys. Chem. C* **2007**, *111*, 15350-15356.

195 H. Frost, T. Düren & R. Q. Snurr; Effects of Surface Area, Free Volume, and Heat of Adsorption on Hydrogen Uptake in Metal−Organic Frameworks. *J. Phys. Chem. B* **2006**, *110*, 9565-9570.

196 D. Frenkel & B. Smit; *Understanding Molecular Simulation : From Algorithms to Applications*. (Academic Press, 2002).

197 D. Dubbeldam, S. Calero, D. E. Ellis & R. Q. Snurr; RASPA: molecular simulation software for adsorption and diffusion in flexible nanoporous materials. *Mol. Simul.* **2015**, 1-21.

198 http://gavrog.org/

199 J. Rouquerol, D. Avnir, C. W. Fairbridge, D. H. Everett, J. M. Haynes, N. Pernicone, J. D. F. Ramsay, K. S. W. Sing & K. K. Unger; Recommendations for the characterization of porous solids (Technical Report). *Pure Appl. Chem.* **1994**, *66*, 1739.

200 C. E. Wilmer, O. K. Farha, Y.-S. Bae, J. T. Hupp & R. Q. Snurr; Structure-property relationships of porous materials for carbon dioxide separation and capture. *Energy Environ. Sci.* **2012**, *5*, 9849-9856.

201 J. L. C. Rowsell, A. R. Millward, K. S. Park & O. M. Yaghi; Hydrogen Sorption in Functionalized Metal−Organic Frameworks. *J. Am. Chem. Soc.* **2004**, *126*, 5666-5667.

202 S. Das, H. Kim & K. Kim; Metathesis in Single Crystal: Complete and Reversible Exchange of Metal Ions Constituting the Frameworks of Metal−Organic Frameworks. *J. Am. Chem. Soc.* **2009**, *131*, 3814-3815.

203 PROCESS (Rigaku Corporation, Tokyo, Japan, 1996).

204 G. M. Sheldrick; A short history of SHELX. *Acta Cryst.* **2008**, *A64*, 112-122.

205 AREAMAX v. 1.1.2 (Rigaku Corporation, 2003).

206 T. Düren, F. Millange, G. Férey, K. S. Walton & R. Q. Snurr; Calculating Geometric Surface Areas as a Characterization Tool for Metal−Organic Frameworks. *J. Phys. Chem. C* **2007**, *111*, 15350-15356.

207 Y.-S. Bae, A. O. Yazaydın & R. Q. Snurr; Evaluation of the BET Method for Determining Surface Areas of MOFs and Zeolites that Contain Ultra-Micropores. *Langmuir* **2010**, *26*, 5475-5483.

208 S. L. Mayo, B. D. Olafson & W. A. Goddard; DREIDING: a generic force field for molecular simulations. *J. Phys. Chem.* **1990**, *94*, 8897-8909.

209 D. Sun, Y. Ke, D. J. Collins, G. A. Lorigan & H.-C. Zhou; Construction of Robust Open Metal−Organic Frameworks with Chiral Channels and Permanent Porosity. *Inorg. Chem.* **2007**, *46*, 2725-2734.

210 X. Zhao, J. Dou, D. Sun, P. Cui, D. Sun & Q. Wu; A porous metal-organic framework (MOF) with unusual 2D to 3D polycatenation based on honeycomb layers. *Dalton Trans.* **2012**, *41*, 1928-1930.

211 P. V. Dau, K. K. Tanabe & S. M. Cohen; Functional group effects on metal-organic framework topology. *Chem. Commun.* **2012**, *48*, 9370-9372.

212 Gaussian 09 v. Revision D.01 (Gaussian, Inc. Wallingford CT, 2013).

213 K. S. W. Sing; Reporting physisorption data for gas/solid systems with special reference to the determination of surface area and porosity (Recommendations 1984). *Pure Appl. Chem.* **1985**, *57*, 603.

214 A. Dutta, A. G. Wong-Foy & A. J. Matzger; Coordination copolymerization of three carboxylate linkers into a pillared layer framework. *Chem. Sci.* **2014**, *5*, 3729-3734.

215 S. Yuan, W. Lu, Y.-P. Chen, Q. Zhang, T.-F. Liu, D. Feng, X. Wang, J. Qin & H.-C. Zhou; Sequential Linker Installation: Precise Placement of Functional Groups in Multivariate Metal–Organic Frameworks. *J. Am. Chem. Soc.* **2015**, *137*, 3177-3180.

216 Y. K. Park, S. B. Choi, H. Kim, K. Kim, B.-H. Won, K. Choi, J.-S. Choi, W.-S. Ahn, N. Won, S. Kim, D. H. Jung, S.-H. Choi, G.-H. Kim, S.-S. Cha, Y. H. Jhon, J. K. Yang & J. Kim; Crystal Structure and Guest Uptake of a Mesoporous Metal–Organic Framework Containing Cages of 3.9 and 4.7 nm in Diameter. *Angew. Chem.* **2007**, *119*, 8378-8381.

217 D. Sun, S. Ma, Y. Ke, D. J. Collins & H.-C. Zhou; An Interweaving MOF with High Hydrogen Uptake. *J. Am. Chem. Soc.* **2006**, *128*, 3896-3897.

218 A. D. Becke; Density‐functional thermochemistry. II. The effect of the Perdew‐Wang generalized‐gradient correlation correction. *J. Chem. Phys.* **1992**, *97*, 9173-9177.

219 C. Lee, W. Yang & R. G. Parr; Development of the Colle-Salvetti correlation-energy formula into a functional of the electron density. *Phys. Rev. B* **1988**, *37*, 785-789.

220 P. Guo, D. Dutta, A. G. Wong-Foy, D. W. Gidley & A. J. Matzger; Water Sensitivity in Zn4O-Based MOFs is Structure and History Dependent. *J. Am. Chem. Soc.* **2015**, *137*, 2651-2657.

221 J. G. Nguyen & S. M. Cohen; Moisture-Resistant and Superhydrophobic Metal−Organic Frameworks Obtained via Postsynthetic Modification. *J. Am. Chem. Soc.* **2010**, *132*, 4560-4561.

222 H. Li, W. Shi, K. Zhao, H. Li, Y. Bing & P. Cheng; Enhanced Hydrostability in Ni-Doped MOF-5. *Inorg. Chem.* **2012**, *51*, 9200-9207.

223 J. Yang, A. Grzech, F. M. Mulder & T. J. Dingemans; Methyl modified MOF-5: a water stable hydrogen storage material. *Chem. Commun.* **2011**, *47*, 5244-5246.

224 T. Wu, L. Shen, M. Luebbers, C. Hu, Q. Chen, Z. Ni & R. I. Masel; Enhancing the stability of metal-organic frameworks in humid air by incorporating water repellent functional groups. *Chem. Commun.* **2010**, *46*, 6120-6122.

225 Y. Kim, S. Das, S. Bhattacharya, S. Hong, M. G. Kim, M. Yoon, S. Natarajan & K. Kim; Metal-Ion Metathesis in Metal–Organic Frameworks: A Synthetic Route to New Metal–Organic Frameworks. *Chem. Eur. J.* **2012**, *18*, 16642-16648.

226 L. Sarkisov & A. Harrison; Computational structure characterisation tools in application to ordered and disordered porous materials. *Mol. Simul.* **2011**, *37*, 1248-1257.

227 A. Spek; Single-crystal structure validation with the program PLATON. *J. Appl. Crystallogr.* **2003**, *36*, 7-13.

228 P. M. Schoenecker, C. G. Carson, H. Jasuja, C. J. J. Flemming & K. S. Walton; Effect of Water Adsorption on Retention of Structure and Surface Area of Metal–Organic Frameworks. *Ind. Eng. Chem. Res.* **2012**, *51*, 6513-6519.

229 Y. Li & R. T. Yang; Gas Adsorption and Storage in Metal−Organic Framework MOF-177. *Langmuir* **2007**, *23*, 12937-12944.

230 http://www.automotive.basf.com/mof_technology_natural_gas/

231 M. D. Allendorf & V. Stavila; Crystal engineering, structure-function relationships, and the future of metal-organic frameworks. *CrystEngComm* **2015**, *17*, 229-246.

232 Calculated using Advanced Chemistry Development (ACD/Labs) Software V11.02 (© 1994-2014 ACD/Labs)

233 J. Canivet, A. Fateeva, Y. Guo, B. Coasne & D. Farrusseng; Water adsorption in MOFs: fundamentals and applications. *Chem. Soc. Rev.* **2014**, *43*, 5594-5617.

234 P. Ghosh, K. C. Kim & R. Q. Snurr; Modeling Water and Ammonia Adsorption in Hydrophobic Metal–Organic Frameworks: Single Components and Mixtures. *J. Phys. Chem. C* **2013**, *118*, 1102-1110.

235 P. Z. Moghadam, P. Ghosh & R. Q. Snurr; Understanding the Effects of Preadsorbed Perfluoroalkanes on the Adsorption of Water and Ammonia in MOFs. *J. Phys. Chem. C* **2015**, *119*, 3163-3170.

236 J. A. Greathouse & M. D. Allendorf; The Interaction of Water with MOF-5 Simulated by Molecular Dynamics. *J. Am. Chem. Soc.* **2006**, *128*, 10678-10679.

237 A. Schoedel, W. Boyette, L. Wojtas, M. Eddaoudi & M. J. Zaworotko; A Family of Porous Lonsdaleite-e Networks Obtained through Pillaring of Decorated Kagomé Lattice Sheets. *J. Am. Chem. Soc.* **2013**, *135*, 14016-14019.

238 N. C. Burtch, H. Jasuja, D. Dubbeldam & K. S. Walton; Molecular-level Insight into Unusual Low Pressure CO_2 Affinity in Pillared Metal–Organic Frameworks. *J. Am. Chem. Soc.* **2013**, *135*, 7172-7180.

239 R. Babarao, C. J. Coghlan, D. Rankine, W. M. Bloch, G. K. Gransbury, H. Sato, S. Kitagawa, C. J. Sumby, M. R. Hill & C. J. Doonan; Does functionalisation enhance CO2 uptake in interpenetrated MOFs? An examination of the IRMOF-9 series. *Chem. Commun.* **2014**, *50*, 3238-3241.

240 P. Khokhlov & P. I. Lazarev; Film and Device Using Layer Based on Ribtan Material. *Int. Pat. Appl.* WO 2009/158553 A2 (**2009**).

241 O. V. Dolomanov, L. J. Bourhis, R. J. Gildea, J. A. K. Howard & H. Puschmann; OLEX2: a complete structure solution, refinement and analysis program. *J. Appl. Crystallogr.* **2009**, *42*, 339-341.

242 2DP v. 1.0.3.4 (Rigaku Corporation, 2011).

243 Discovery Studio (Accelrys Software Inc., 2012).

244 Y.-S. Bae, A. O. z. r. Yazaydın & R. Q. Snurr; Evaluation of the BET Method for Determining Surface Areas of MOFs and Zeolites that Contain Ultra-Micropores. *Langmuir* **2010**, *26*, 5475-5483.

245 C. E. Wilmer, K. C. Kim & R. Q. Snurr; An Extended Charge Equilibration Method. *J. Phys. Chem. Lett.* **2012**, *3*, 2506-2511.

246 W. L. Jorgensen, J. Chandrasekhar, J. D. Madura, R. W. Impey & M. L. Klein; Comparison of simple potential functions for simulating liquid water. *J. Chem. Phys.* **1983**, *79*, 926-935.

247 C. N. Satterfield; *Heterogeneous catalysis in industrial practice. 2nd edition*. (1991).

248 A. Corma, H. García & F. X. Llabrés i Xamena; Engineering Metal Organic Frameworks for Heterogeneous Catalysis. *Chem. Rev.* **2010**, *110*, 4606-4655.

249 J. Lee, O. K. Farha, J. Roberts, K. A. Scheidt, S. T. Nguyen & J. T. Hupp; Metal-organic framework materials as catalysts. *Chem. Soc. Rev.* **2009**, *38*, 1450-1459.

250 P. Wu, C. He, J. Wang, X. Peng, X. Li, Y. An & C. Duan; Photoactive Chiral Metal–Organic Frameworks for Light-Driven Asymmetric α-Alkylation of Aldehydes. *J. Am. Chem. Soc.* **2012**, *134*, 14991-14999.

251 L. Ma, C. Abney & W. Lin; Enantioselective catalysis with homochiral metal-organic frameworks. *Chem. Soc. Rev.* **2009**, *38*, 1248-1256.

252 Z.-M. Zhang, T. Zhang, C. Wang, Z. Lin, L.-S. Long & W. Lin; Photosensitizing Metal–Organic Framework Enabling Visible-Light-Driven Proton Reduction by a Wells–Dawson-Type Polyoxometalate. *J. Am. Chem. Soc.* **2015**, *137*, 3197-3200.

253 C. Wang, J.-L. Wang & W. Lin; Elucidating Molecular Iridium Water Oxidation Catalysts Using Metal–Organic Frameworks: A Comprehensive Structural, Catalytic, Spectroscopic, and Kinetic Study. *J. Am. Chem. Soc.* **2012**, *134*, 19895-19908.

254 X. Yu & S. M. Cohen; Photocatalytic metal-organic frameworks for the aerobic oxidation of arylboronic acids. *Chem. Commun.* **2015**,

255 D. Feng, Z.-Y. Gu, J.-R. Li, H.-L. Jiang, Z. Wei & H.-C. Zhou; Zirconium-Metalloporphyrin PCN-222: Mesoporous Metal–Organic Frameworks with Ultrahigh Stability as Biomimetic Catalysts. *Angew. Chem. Int. Ed.* **2012**, *51*, 10307-10310.

256 J. S. Seo, D. Whang, H. Lee, S. I. Jun, J. Oh, Y. J. Jeon & K. Kim; A homochiral metal-organic porous material for enantioselective separation and catalysis. *Nature* **2000**, *404*, 982-986.

257 K. Mo, Y. Yang & Y. Cui; A Homochiral Metal–Organic Framework as an Effective Asymmetric Catalyst for Cyanohydrin Synthesis. *J. Am. Chem. Soc.* **2014**, *136*, 1746-1749.

258 Y. Liu, X. Xi, C. Ye, T. Gong, Z. Yang & Y. Cui; Chiral Metal–Organic Frameworks Bearing Free Carboxylic Acids for Organocatalyst Encapsulation. *Angew. Chem.* **2014**, *126*, 14041-14045.

259 P. Dydio & J. N. H. Reek; Supramolecular control of selectivity in transition-metal catalysis through substrate preorganization. *Chem. Sci.* **2014**, *5*, 2135-2145.

260 M. Raynal, P. Ballester, A. Vidal-Ferran & P. W. N. M. van Leeuwen; Supramolecular catalysis. Part 2: artificial enzyme mimics. *Chem. Soc. Rev.* **2014**, *43*, 1734-1787.

261 M. Gruttadauria, F. Giacalone & R. Noto; Supported proline and proline-derivatives as recyclable organocatalysts. *Chem. Soc. Rev.* **2008**, *37*, 1666-1688.

262 G. W. Parshall & S. D. Ittel; *Homogeneous Catalysis: The Applications and Chemistry of Catalysis by Soluble Transition Metal Complexes*. (Wiley, 1992).

263 A. Berkessel & H. Gröger; *Asymmetric Organocatalysis: From Biomimetic Concepts to Applications in Asymmetric Synthesis*. (Wiley-VCH, 2005).

264 G. J. Bartlett, C. T. Porter, N. Borkakoti & J. M. Thornton; Analysis of Catalytic Residues in Enzyme Active Sites. *J. Mol. Biol.* **2002**, *324*, 105-121.

265 D. Ringe & G. A. Petsko; How Enzymes Work. *Science* **2008**, *320* 1428-1429.

266 M. Lee, S. M. Shin, N. Jeong & P. K. Thallapally; Chiral environment of catalytic sites in the chiral metal-organic frameworks. *Dalton Trans.* **2015**, *44*, 9349-9352.

267 S. Hertel, M. Wehring, S. Amirjalayer, M. Gratz, J. Lincke, H. Krautscheid, R. Schmid & F. Stallmach; NMR studies of benzene mobility in metal-organic framework MOF-5. *Eur. Phys. J. Appl. Phys.* **2011**, *55*, 20702.

268 M. Arnó & L. R. Domingo; Density functional theory study of the mechanism of the proline-catalyzed intermolecular aldol reaction. *Theor. Chem. Acc.* **2002**, *108*, 232-239.

269 A. J. A. Cobb, D. M. Shaw, D. A. Longbottom, J. B. Gold & S. V. Ley; Organocatalysis with proline derivatives: improved catalysts for the asymmetric Mannich, nitro-Michael and aldol reactions. *Org. Biomol. Chem.* **2005**, *3*, 84-96.

270 A. D. Burrows; Mixed-component metal-organic frameworks (MC-MOFs): enhancing functionality through solid solution formation and surface modifications. *CrystEngComm* **2011**, *13*, 3623-3642.

271 D. N. Bunck & W. R. Dichtel; Mixed Linker Strategies for Organic Framework Functionalization. *Chem. Eur. J.* **2013**, *19*, 818-827.

272 W. Notz, F. Tanaka & C. F. Barbas; Enamine-Based Organocatalysis with Proline and Diamines: The Development of Direct Catalytic Asymmetric Aldol, Mannich, Michael, and Diels−Alder Reactions. *Acc. Chem. Res.* **2004**, *37*, 580-591.

273 U. Eder, G. Sauer & R. Wiechert; New Type of Asymmetric Cyclization to Optically Active Steroid CD Partial Structures. *Angew. Chem. Int. Ed. Engl.* **1971**, *10*, 496-497.

274 F. Goubard & F. Dumur; Truxene: a promising scaffold for future materials. *RSC Adv.* **2015**, *5*, 3521-3551.